Numerical Modelling of Paper-Based Microfluidic Flow Cells

by

Pardis Sadeghi

B.Sc., University of Tehran, Iran, 2019

Thesis Submitted in Partial Fulfillment of the
Requirements for the Degree of
Master of Applied Science

in the
School of Mechatronic Systems Engineering
Faculty of Applied Sciences

SIMON FRASER UNIVERSITY
Fall 2021

Declaration of Committee

Name:	**Pardis Sadeghi**
Degree:	**Master of Applied Science**
Title:	**Numerical Modelling of Paper-Based Microfluidic Flow Cells**

Committee:

Chair: **Siamak Arzanpour**
Associate Professor, Mechatronic Systems Engineering

Erik Kjeang
Supervisor
Professor, Mechatronic Systems Engineering

Bonnie Gray
Committee Member
Professor, Engineering Science

Behraad Bahreyni
Examiner
Associate Professor, Mechatronic Systems Engineering

Abstract

A general mathematical/numerical methodology was developed for paper-based, microfluidic electrochemical flow cells. The methodology involves capillary flow, imbibition, mass transport, and electrochemical reactions. The combined model was implemented on a novel microfluidic paper-based flow battery called PowerPAD and rendered numerical results that are very close to published experimental data for this prospective flow cell both under steady and unsteady conditions. It also enabled identifying back-diffusion and species crossover as the key factors controlling the power output and runtime of this flow cell while the role of migration flux was shown to be negligible. The mathematical model was also used for optimizing the electrochemical performance of the PowerPAD. By modifying the design of the electrode and the absorbent pad currently used in this particular flow cell, an optimized design was found that is predicted to roughly triple the runtime of the PowerPAD. The new design has a higher efficiency and a flatter power-output curve making it more suitable for small-scale consumer electronics, as compared with the current design. Overall, the research outcomes may contribute to a new generation of practical, biodegradable batteries based on the modified PowerPAD cell design proposed in this work.

Keywords: battery; microfluidic; numerical model; quinone; crossover; biodegradable

Dedication

I dedicate this thesis to my husband (Mehdi) for his love and affection, and also to our great families for their constant support and persistent encouragement throughout this challenging but enjoyable MASc journey.

Acknowledgements

I would like to express my sincerest gratitude to my great supervisor, Professor Erik Kjeang, for giving me the opportunity to work with him on this fascinating project. I am also grateful to Professor Kjeang for the constant support granted to me during my Master's journey all through these difficult years. The freedom and flexibility granted to me to try/pursue different ideas are also much appreciated. Without the constructive comments that I have received from my supervisor during our bi-weekly meetings I could not have reached the milestones of this project. I also would like to thank Dr. Omar Ibrahim for his willingness to answer my relentless questions. Special thanks are due to Dr. Mohammad Pourjafar for teaching me how to work with COMSOL and also for his willingness to debug my codes whenever needed. I would like to thank my fellow classmates that made the office/lab a joyful place to work in. I also would like to thank my defence and supervisory committee for accepting to review this bulky thesis. The constructive comments received from the members of the committee (either during or after the defence session) are also much appreciated; I found them very useful and very relevant indeed. Finally, I would like to gratefully acknowledge the Funding received from Natural Sciences and Engineering Research Council of Canada (NSERC), Canada Foundation for Innovation (CFI) and British Columbia Knowledge Development (BCKDF).

Table of Contents

List of Tables

List of Figures

List of Acronyms

OCV	Open Circuit Voltage
PDE	Partial Differential Equation
PEM	Polymer Exchange Membrane
RFB	Redox Flow Battery
SCE	Saturated Calomel Electrode
SOC	State-of-Charge
RDK	Rapid Diagnostic Kit
POC	Point-of-Care
PPC	Power Performance Curve

Glossary

Roman	Definition	Unit
A	Area	m^2
a	Specific area	m^{-1}
c	Concentration	mol/m^3
D	Diffusion coefficient	m^2/s
d	Diameter	m
E	Electric potential	V
F	Faraday's constant = 96,487	C/mol
H	Height of the electrode	m
h	Height of the pad	m
I	Current	A
j	Current density	A/m^2
k	Reaction rate constant	m/s
k_m	Mass transport coefficient	m/s
L	Length	m
N	Molar mass	kg/mol
N	Flux density	$mol/s/m^2$
n	Exponent in the Richards model	—
n	Number of electrons	—
P	Power	mW
p	Pressure	Pa
q_{th}	Theoretical capacity	mA.hr
Q	Flow rate	m^3/s
R	Molar gas constant = 8.314	J/mol/K
R	Source/sink term	$mol/ m^3/s$
x	Position vector	m
S	Saturation	—
T	Temperature	K
t	Time	s
u,v	Velocity components	$m.s^{-1}$
V	Volume	m^3
W	Width of electrode	m
w	Width of pad	m
x,y,z	Cartesian coordinates	m
Z	Charge number	—

Greek	Definition	Unit
α	Transfer coefficient	—
β	Volume fraction	—
γ	Ionic activity	—
μ	Dynamic viscosity	mPa.s
ξ	Ionic mobility	$m^2.mol/J/s$

G	Gibbs free energy	J/mol
δ	Diffusion layer thickness	m
δ	Gap distance	m
ε	Porosity	–
θ	Contact angle	deg
φ	Potential	V
η	Overpotential	V
κ	Permeability	m^2
λ	Exponent in the Brooks-Corey Model	–
ρ	Density	kg/m^3
σ	Electric conductivity	S/m
Γ	Surface tension	N/m

Subscripts	**Meaning**
a	Anodic property
c	Cathodic property
c	Capillary
eff	Effective value
f	Electrolyte
i	Species
o	Oxidant
r	Reductant
s	Electrode
0	Initial value
2,3,4,5	C(II), C(III), C(IV) and C(V) species

Superscripts	**Meaning**
eff	Effective value
eq	Equilibrium value
0	Reference value
s	Surface value
−	Negative electrode
+	Positive electrode

Dimensionless Numbers:

Re	Reynolds number
Sc	Schmidt number
Sh	Sherwood number
Ψ	Electric-Potential Number

Chapter 1:

Introduction

1.1. Energy Demands in Consumer Electronics

Portable electronic devices such as laptops, cell phones, tablets, smart-watches, head-phones, MP3 players, and the like are increasingly playing a key role in our everyday life [1]. In fact, these days, it is hard to imagine a world without, say, cell phones. These small-sized devices, which are categorized as consumer-electronics, need electrical energy to function. While some of them can be powered by renewable energies such as solar cells, as it stands, the power needs of devices such as cell phones and laptops can only be met with conventional cells such as lithium-ion batteries. Although these conventional dry cells are highly efficient and affordable, it should be conceded that they are not sustainable. For example, the world's Lithium resources are limited and they are not renewable. More importantly, extraction of lithium from its ores needs toxic chemicals which can easily pollute aquifers [2]. To these should be added the fact that disposal of such dry cells is troublesome. A major problem is the notion that they are often discarded while not fully discharged. This means that the toxic chemicals still left inside the battery can easily harm the environment whenever there is a leakage—which is very likely in landfills. For reasons like these, the search for new battery technologies is still an active field of research. In a world that is being re-imagined with *green* energy, an ideal battery technology is the one that is completely bio-degradable and eco-friendly. Fortunately, certain types of fuels cells and flow-batteries may meet this "green-cell" criterion.

1.2. Fuel Cells and Flow Batteries

Fuel cells and flow batteries are electrochemical cells that convert the chemical energy of a fuel into electricity through a pair of redox reactions [3]. They differ from ordinary dry cells in that they require a continuous supply of fuel to sustain their electrochemical reactions. While the idea is not new and dates back to 18th century, only recently are we

witnessing the use of this technology in large-scale systems such as vehicles. They are also increasingly being used as energy-storage systems for intermittent sources of energy such as wind or solar. In recent years, we are seeing a growing interest in extending the fuel-cell/flow-battery technology to small-scale, point-of-care (POC) electronic devices such as rapid-diagnostic kits (RDK). Figure 1.1 shows one of these kits equipped with printed circuitry so that it can digitally show the test result and communicate it with remote labs or physicians via cell phones. Kits like this are increasingly being used all around the globe for medical care [4]. Their widespread popularity stems from the notion that they are very affordable in addition to being accurate and quite fast. Fortunately, the power requirements of current commercially-available diagnostic e-kits is well within the range of certain microfluidic flow-cell technologies.

Figure 1.1. A typical microfluidic diagnostic kit equipped with printed electronics.

1.3. Microfluidic Flow Cells

Microfluidics is the science of manipulating small amounts of a fluid when it flows through channels of millimeter or sub-millimeter scale [6]. An example is the flow of blood through the capillaries in human body. In recent years, microfluidics has emerged as an active area of research thanks to its application in important fields such as biology and medicine. They are also increasingly being used in physical sciences such as

electro-chemistry. A key feature of microfluidic systems is that due to small length scales involved, flow in such systems normally occur under laminar regime. In laminar flows, momentum exchange between fluid layers occurs at microscopic level. This feature of microfluidic systems has been greatly utilized in the development of membrane-less microfluidic flow cells. That is to say that, with no macroscopic mixing occurring between the two electrolytes, microfluidic flow cells can function with no need for a physical membrane [7]. With no membrane in place to separate the two half-cells, free diffusion of active ions can take place at the interface between the two electrolytes while they are flowing co-laminarly down a micro-channel.

The first “membrane-less” microfluidic flow cell was developed by Ferrigno et. al. [8] in 2002, and further extended by Choban et. al. [9] in 2004. Since then, this field of research has witnessed great progress in tackling a variety of challenges [10]. A major problem in extending membrane-less microfluidic flow cells to consumer electronics is their reliance on a (syringe) pump for circulating the electrolytes. Evidently, integrating such a micropump in a diagnostic kit significantly increases its complexity and therefore its final price not to mention that a micropump itself needs a battery to be activated. Fortunately, introduction of paper-based microfluidic systems has eliminated the need for any type of mechanical micropump. That is to say that, cellulosic papers can automatically do the pumping job through capillary action with no need for an external power source.

1.4. Paper-Based Microfluidics

Paper-based microfluidics refers to devices that are made of hydrophilic materials. Such materials can transport a wetting liquid through their wicking effect. In other words, capillary pressure generated in the pores of the material can automatically force the contained fluid to flow through the material with no need for an external pressure gradient. Development of paper-based microfluidic devices dates back to early 21st century. Around that time, there was a growing demand for inexpensive, portable diagnostic systems that could detect contagious agents and chemical contaminants. The first paper-based microfluidic device was developed at Harvard University for detecting protein and glucose via color-change reactions [11]. Since then, paper-based

microfluidic devices have found many other applications outside the medical field. For example, they are widely used in environmental monitoring for the detection of E. coli in water resources. They are also used for the detection of pesticides, heavy-metals, or antibiotics in food products [12-14].

In recent years, interest in paper-based systems has soared when it was realized that they can be used for developing inexpensive *microfluidic* fuel cells, flow batteries, and electrolyzers [15-17]. One can particularly mention the novel membrane-less, paper-based flow cell designed by Esquivel *et al*. [16] called PowerPAD. The cell is completely bio-degradable, and so it does not harm the environment when disposed of. The fact that cellulosic papers are abundant, cheap, and eco-friendly, not to mention that paper-based systems can easily be transported, distributed, and safely incinerated with virtually no harm to the environment, has made this prospective flow cell a good candidate for low-power, single-use applications such as rapid-diagnostic kits.

1.5. PowerPAD Flow Battery

PowerPAD is a novel flow cell made of cellulosic paper and beeswax. It relies on quinone species as its redox couples [16]. The cell can generate electrical power that is large enough for energizing single-use diagnostic kits and remote sensors. It is anticipated that through proper design modifications, the range of applicability of PowerPAD can further be enhanced. Figure 1.2 shows this small-sized flow cell. In principle, the initially-unsaturated cell can start generating power in a couple of seconds as soon as a drop of test liquid is placed on its sample pad. In practice, however, the cell is used under fully-saturated conditions.

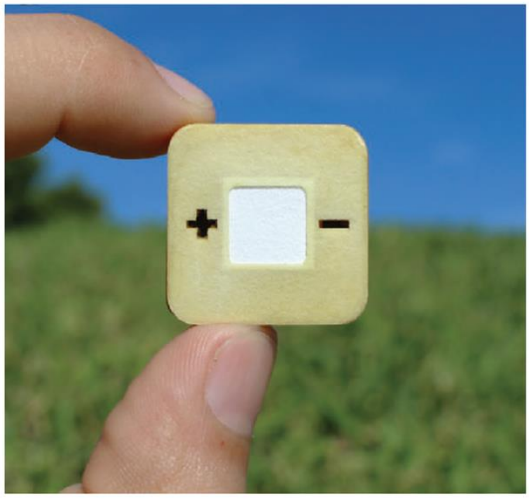

Figure 1.2. A novel paper-based microfluidic cell called PowerPAD [16].

An open access article reproduced with permission from Wiley and Sons.

The fundamental understanding of the unique function of PowerPAD (and other paper-based microfluidic flow batteries similar to it) would benefit from a proper mathematical modelling of the device and its electrochemical performance. With such a model, it would be feasible to investigate the effect of different parameters on the system performance with no need for exhaustive/expensive trial-and-error experimental methods. At present, no such mathematical model is available in the open literature for any paper-based microfluidic flow battery. A major obstacle in developing such a model is the heterogeneous nature of this type of cells. That is to say that, the electrode material is normally different from the absorbent-pad material. In practice, this translates itself into non-trivial, highly-nonlinear interfacial boundary conditions at the electrode/pad interface, which makes obtaining converged numerical results quite difficult. The notion that the system is originally unsaturated and remains partially-saturated during its transient phase of operation (i.e., before it becomes fully-saturated) further complicates any mathematical development and numerical simulation.

1.6. Thesis Objectives

There is an urgent need for developing a robust mathematical/numerical model for designing paper-based flow cells such as PowerPAD. It is the main objective of this Master's thesis to develop a *general* mathematical framework that can be used to understand and design paper-based, capillary-driven, membrane-less microfluidic flow batteries. The methodology will be used to simulate the steady and unsteady behavior of the PowerPAD reported in [16]. After validating the mathematical model against experimental data, it will be used to optimize the design currently used in this particular flow cell with the main objective being to extend its runtime and power output.

1.7. Organization

After this introductory chapter, in Chapter 2 some background knowledge is presented in relation to modelling electrochemical cells, in general, and microfluidic flow cells, in particular. In Chapter 3, the two-step mathematical model developed in this thesis for simulating paper-based flow cells is presented. In the same chapter, the 2D flow geometry used for representing PowerPAD (which is a 3D cell) is also introduced. In Chapter 4, the numerical method selected for solving the governing equations is presented. Chapter 5 is devoted to validating the mathematical/numerical model with published steady/unsteady data for the PowerPAD. In this chapter, crossover is also modelled and its effect on the performance of PowerPAD is investigated. In Chapter 6, the methodology developed in this thesis work is used for optimizing the current design through exploring different design alternatives for the electrode, absorbent pad, and flow architecture. An optimized design is proposed that is shown to outperform the current design in terms of runtime, power output, and efficiency. In Chapter 7 a summary of the key findings of the work is presented and suggestions are made for future studies. This chapter also lists the publications made based on the results of this thesis work.

Chapter 2:

Theory of Paper-Based Electrochemical Cells

2.1. Introduction

Electrochemistry is a branch of physical chemistry which studies reaction of chemical species at the interface between an electronic conductor (electrode) and an ionic conductor (electrolyte). Devices in which such reactions take place are called *electrochemical cells*. As their main components, they comprise the electrodes**,** the electrolyte solutions, and a load-carrying circuit [18]. In electrochemical cells the chemical reactions are of redox type where electrons or ions are removed from the oxidized species with the same number of electrons or ions added to the reduced species. That is to say that, oxidation at one electrode is exactly balanced by reduction at the other electrode.

2.2. Redox Flow-Battery

A redox flow-battery is a good example of an electrochemical cell. In terms of its working principles, it has much in common with the fuel cells. But, unlike fuel cells, where the oxidant and reductant are generally in gaseous form, a flow-battery relies on liquid electrolytes at various oxidation states for its functioning [19]. Both types of cells require a continuous supply of reactants and also a continuous removal of the products to/from the electrodes. A key feature of flow batteries is that, unlike ordinary dry-cells, it is possible to increase their energy-storage capacity by simply increasing the volume of the electrolyte stored in their tanks. It is also possible to control their output power by simply connecting similar cells in parallel or in series. As mentioned in Chapter 1, they are increasingly being used for grid-scale energy storage [20]. In recent developments, biodegradable redox couples such as quinone species have been used as redox couples in both half-cells. And this can be regarded as a significant step in the development of eco-friendly flow-battery technology [21].

In generic form, the redox reactions that take place on the surface of the electrodes of a typical flow battery can be formulated as shown below [19]:

Negative Half-Cell: $A^{m+} \Leftrightarrow A^{(m+x)+} + xe^{-}$

Positive Half-Cell: $B^{n+} + xe^{-} \Leftrightarrow B^{(n-x)+}$ (2.1)

Here, in analogy with the commonly used vanadium redox cell, the redox species have been arbitrarily denoted by A2/A3 (negative side) and B4/B5 (positive side). An overview of a typical redox flow cell, similar to those used in power industry, is shown schematically in Fig. 2.1. To limit species crossover (see Chapter 5) the cell shown in this figure incorporates a physical proton-exchange membrane so that the two electrolytes can be physically separated from each other.

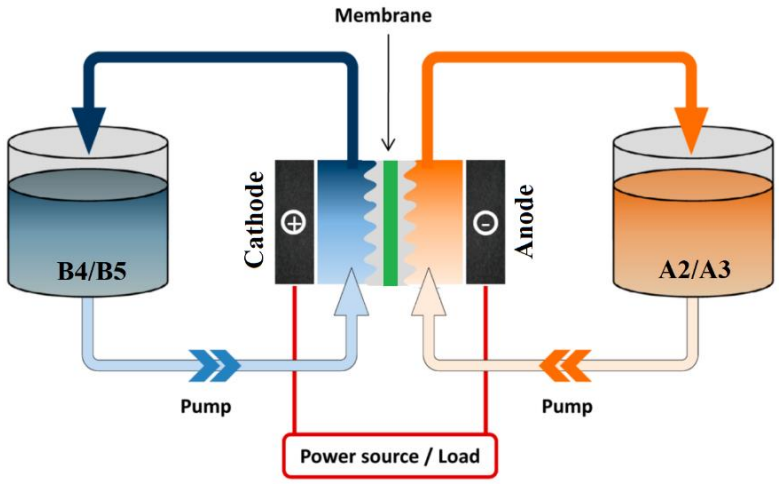

Figure 2.1. Schematic depicting a typical redox flow-cell.

An open access article [21] reproduced from The MDPI under creative commons license (CC BY-NC-ND 4.0).

The *reversible* potential of redox couples in each half-cell (E) is of key importance in the design of flow batteries as it signifies the tendency of a redox species to be reduced or oxidized on the surface of the respective electrode. According to the Nernst equation [19], this potential can be related to the concentration of the reactants:

$$E = E^{0} + \frac{RT}{nF} ln\left(\frac{c_o}{c_r}\right), \quad (2.2)$$

where E^0 is the *standard* or *thermodynamic* potential of the half-cell, R is the universal gas constant, T is the absolute temperature, F is the Faraday's constant, *n* is the number of electrons transferred, and "c" is the bulk concentration with subscripts "o" and "r" referring to the oxidant and reductant, respectively. In this equation, E_0 is the *standard* potential, which can be related to the Gibbs free energy (ΔG) as shown below [19]:

$$E^0 = -\frac{\Delta G}{nF}. \tag{2.3}$$

The net *equilibrium* or *reversible* potential of the whole cell can be obtained knowing their values in the positive (+) and negative (–) half-cells:

$$E_{eq} = E^+ - E^-. \tag{2.4}$$

In practice, however, this potential cannot be obtained in the real world. This is because, like any other thermodynamic system, flow batteries are vulnerable to various types of irreversibility in relation to the transport processes involved: i) mass transport, ii) momentum transport, and iii) charge transport. Thus, electrochemical cells normally operate at potentials significantly lower than their reversible potentials. The difference between *actual* potential and *reversible* potential is called *overpotential*. While in a *galvanic* cell, overpotential means that less energy is generated than the thermodynamically-determined value, in an *electrolytic* cell it means more energy must be supplied to reverse the redox reaction. In both cases, the missing energy is lost as heat. The relationship between a cell's true potential and the electric current is called *polarization* (or, performance) curve. Such curves can be usually obtained experimentally using a potentiostat or galvanostat. They can also be obtained numerically if sufficient information is available about the cell's kinetics.

Figure 2.2 shows a typical polarization curve in galvanic mode for an all-vanadium cell. In this figure, OCV is the open-circuit voltage of the cell, i.e., the maximum voltage that a cell can generate in the *galvanic* mode or the minimum voltage that must be supplied to recharge the cell in the *electrolytic* mode. In general, there are four main sources for potential loss in a flow cell, as listed below [22]:

Activation Overpotential (η_A): This overpotential, which is also called the "kinetic loss", refers to a drop in potential due to irreversibility in the reaction kinetics at both electrodes. Activation losses are formed when electrochemical reactions at the electrode/electrolyte interface have sluggish kinetics. This type of loss becomes more important at low current densities. It is a nonlinear function of the current density; see Fig. 2.2. The voltage drop due to activation overpotential can be calculated using the Butler-Volmer equation.

Ohmic Overpotential (η_O): This overpotential, which is also called "ohmic loss, refers to the potential drop caused by the ohmic resistance of the electrode, wiring, current collector, and the electrolyte. The ohmic resistance is a linear function of the current density; see Fig. 2.2.

Mass-Transport Overpotential (η_M): This overpotential, which is also called "concentration loss", refers to mass transport limitations at both electrodes. It occurs when the electrode's reaction is so fast that the reactant molecules cannot reach the reaction sites on the electrode(s). The situation becomes worse when the products of the electrochemical reactions cannot leave the reaction sites fast enough. In practice, both effects may co-exist and they give rise to a depletion of the reactants or accumulation of the products at the surface of the electrode. This type of potential loss varies nonlinearly with the current density; see Fig. 2.2.

Crossover Overpotential (η_X): In cases where redox couples in the anolyte are different from those in the catholyte, the reactants may cross over the opposite half-cell and react electrochemically with the wrong electrode giving rise to *mixed* potential. Chemical side-reactions occurring in the bulk electrolytes and the parasitic loss associated with current leakage also contribute to this unwanted overpotential. Crossover usually needs an elaborate theoretical analysis and cannot be estimated by such simple relationships.

The different losses listed above can significantly lower a cell's open-circuit voltage (OCV) below its thermodynamic value (E^0); see Fig. 2.2. Depending on a cell working

in the galvanic mode or in the electrolytic mode, a cell's voltage, V_{cell}, can be obtained knowing its different sources of overpotentials [23]:

$$V_{cell} = E_{eq} \pm (|\eta_A| + |\eta_O| + |\eta_M| + |\eta_X|), \quad (2.8)$$

where the *minus* sign refers to the galvanic mode with the *plus* sign referring to the electrolytic mode.

Figure 2.2 shows the polarization curve in the galvanic mode without considering the crossover loss. Polarization curves like this are normally obtained by varying the external load resistance from zero to infinity (ohms). This figure clearly demarcates the regions dominated by the three main sources of overpotential mentioned above: i) the kinetic loss, ii) the ohmic loss, and iii) the mass-transport loss. For reasons to be discussed shortly, cells are usually operated in the region dominated by the ohmic loss—the so-called "operational range". For the cell depicted in Fig. 2.2, the ohmic polarization corresponds to the current density in the range of 0.18 A/cm^2 < i < 0.67 A/cm^2. For reasons to be made clear shortly, cells are usually used in the ohmic region. For a given cell to work under this condition, the external load should be within a certain range. Figure 2.2 shows the two extremes of the external load (by blue lines) which can guarantee that for this cell. We can easily determine the load at which the power output of the cell becomes maximum. To that end, we can resort to the power-performance curve of the cell [23].

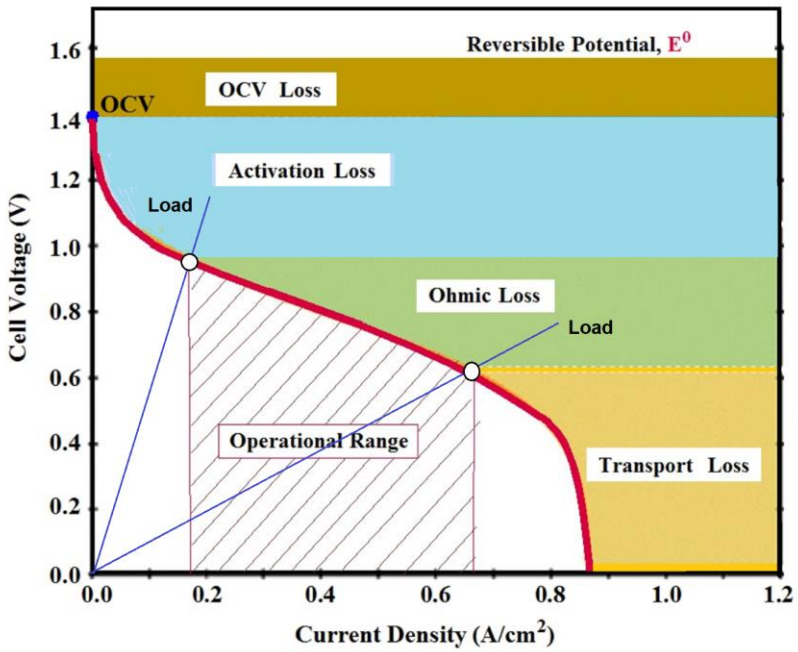

Figure 2.2. A typical polarization curve depicting different types of overpotentials.

A power-performance-curve (PPC) can be obtained by intersecting a given polarization curve by a large number of load lines all emanating from the origin (similar to the two blue lines shown in Fig. 2.2). The power corresponding to the voltage and current of each intersection point then constitutes a single point on the PPC curve. As an example, Fig. 2.3 shows a generic PPC curve obtained for a typical flow cell. This figure clearly shows that, the power output of a cell varies with the external load and reaches a maximum for a certain external load. It is counter-intuitive to see that by lowering the external load (starting, say, from infinity) a cell's power output is increased up to a certain load beyond which it sharply drops when the external load is further decreased. In Chapter 5, we will discuss such issues in some details for the PowerPAD. We also show that the maximum power lies in the region corresponding to the ohmic loss; see Fig. 2.2. What is evident is that, the power-performance curve is a very useful tool for evaluating the performance of a given cell while it is under load. In fact, power-performance curves are widely used by engineers for optimizing a cell which is to be used to energize a given load [23]. A cell can be optimized in such a way that for a given external load its power output becomes maximum; see Chapter 6.

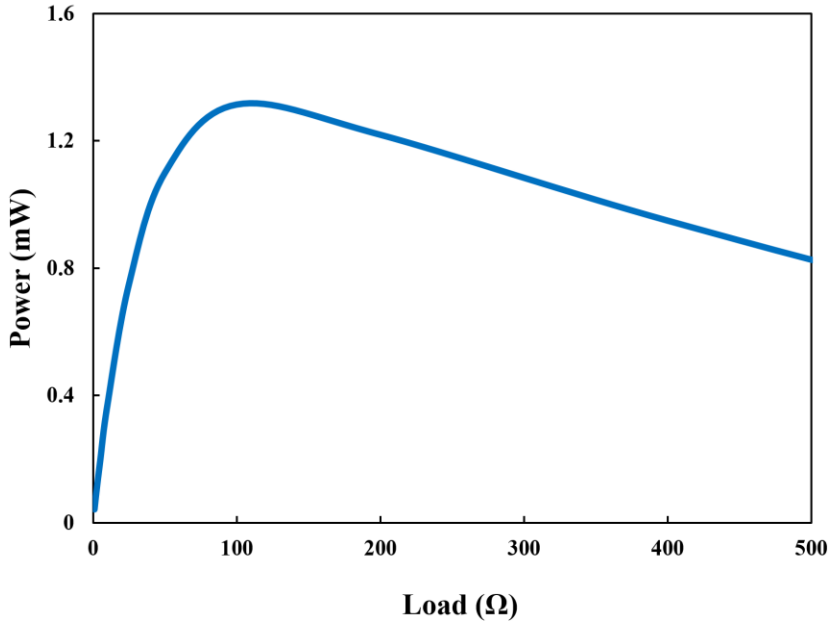

Figure 2.3. A typical power-performance curve (PPC) showing a maximum in power output reached at a certain optimized resistance.

2.3. Electrochemical Modelling

Electrochemical modelling of macro-size and micro-size flow cells have much in common although the latter is a bit more complicated because the size of the charges may play a role when compared with the length scale of the device. Whether macro or micro, electric current is generated in a cell when active species reach the surface of the electrodes and react electrochemically with either the catalyst or the bare carbon fibers. Below we can see a typical electrode reaction:

$$O + ne^{-} \Leftrightarrow r, \tag{2.9}$$

where “o” and “r” refer, respectively, to the reactants and the products. By Faraday’s first law, the rate of an electrode reaction is related to its current density as shown below:

$$\left(\frac{\partial N}{\partial t}\right)_c = \frac{j_c}{nF} \quad ; \quad \left(\frac{\partial N}{\partial t}\right)_a = \frac{j_a}{nF} \tag{2.10}$$

where subscripts “c” and “a” refer to the *cathodic* and *anodic* reactions, respectively. In these relationships, $\partial N/\partial t$ is the number of moles that are reacting with the electrode per unit time, and “j” is the current density. The net electronic current in the electrodes can then be obtained as:

$$I = jA = \left(j_c - j_a\right)A \tag{2.11}$$

where A is the active area of the electrode. The charge current density of each electrode can be related to the activation overpotential and species concentration through the Butler-Volmer equation (BV) as show below [23]:

$$j_1 = j_c = Fk_c\left(c_{IV}\right)^{\alpha_{1,c}}\left(c_V\right)^{\alpha_{1,a}}\left[\frac{c_{IV}^s}{c_{IV}}\exp\left(\frac{\alpha_{1,a}nF}{RT}\eta_c\right) - \frac{c_V^s}{c_V}\exp\left(-\frac{\alpha_{1,c}nF}{RT}\eta_c\right)\right] \tag{2.12a}$$

$$j_2 = j_a = Fk_a\left(c_{II}\right)^{\alpha_{2,c}}\left(c_{III}\right)^{\alpha_{2,a}}\left[\frac{c_{II}^s}{c_{II}}\exp\left(\frac{\alpha_{2,a}nF}{RT}\eta_a\right) - \frac{c_{III}^s}{c_{III}}\exp\left(-\frac{\alpha_{2,c}nF}{RT}\eta_a\right)\right] \tag{2.12b}$$

where superscript “s” refers to the surface values. (Surface concentration can be related to the overpotential by writing the mass-conservation law for each ion, as shown by Shah et al [24].) In these equations, k_a and k_c are respectively the oxidation and reduction rate-constants, α is the charge transfer coefficient (with subscripts *a* and *c* referring to anodic and cathodic reactions), and η is the activation *overpotential* (subscript “A” has been dropped from the overpotential for convenience). The activation overpotential is related to the electrode potential, φ_s, as shown below [24]:

$$\eta_c = \left(\varphi_s - \varphi_f\right)_c - E_c \tag{2.13a}$$

$$\eta_a = \left(\varphi_s - \varphi_f\right)_a - E_a \tag{2.13b}$$

where φ_f is the ionic potential (i.e., the potential induced in the electrolyte due to the movement of *charged* species), and $\left(E_c, E_a\right)$ are the *equilibrium* potential of the electrolyte at the surface of the cathode and anode, respectively. As earlier mentioned, the equilibrium potential can be found using the Nernst equation (see Eq. 2.2). It needs

to be mentioned that, in general, Nernst equation also includes the *activity* of oxidant and reductant, as shown below [19]:

$$E = E^0 + \frac{RT}{nF} \ln\left(\frac{c_o^s}{c_r^s} \cdot \frac{\gamma_o}{\gamma_r} \right) \tag{2.14}$$

where γ [dimensionless] is the *activity coefficient*. While in dilute solutions activity of ions is nearly equal to one, in concentrated solutions, due to significant ion-ion interactions, it can be much smaller than one. (An activity less than one means that the amount of species actually available for electrochemical reaction is less than its nominal concentration in the bulk electrolyte.)

2.3.1. Mass Transfer

The relationships presented in the above section relate the current generated by an electrochemical system to: i) the electronic potential applied to the electrode, φ_s, ii) the ionic potential induced in the electrolyte, φ_f, and iii) the reaction kinetic constants. But, before we can record any current from an electrochemical cell, the active species must reach the surface of the electrodes at the first place. As a matter of fact, the products must also be washed away from the surface of the electrodes, presumably, at the same rate. Evidently, mass transfer to/from the electrodes plays a key role in the proper functioning of an electrochemical cell. In general, there are three mechanisms for mass tranfer: i) convection, ii) diffusion, and iii) migration. The total ionic flux can then be written as a summation of these three types of flux [19]:

$$\mathbf{N}_{tot} = \mathbf{N}_{conv} + \mathbf{N}_{diff} + \mathbf{N}_{mig}. \tag{2.15}$$

The three modes of flux can be modelled as shown below.

Convection Flux:

In ordinary flow batteries the electrolyte is circulated by a pump whereas in paper-based systems it is set into motion by capillary forces. In both cases, the flowing electrolyte directs ionic species to/from the electrode surface. The convective flux of each species is proportional to its velocity in the respective half-cell; that is:

$$\mathbf{N}_{conv} = \mathbf{u}_j c_i \quad ; \quad j = a, c \tag{2.16}$$

where **u** is the velocity vector.

Diffusion Flux:

Ions can diffuse in an electrolyte if there exists a concentration gradient. Such gradients normally arise when ions start being consumed at the surface of the electrode while undergoing electrochemical reactions. With their concentrations being high in the bulk solution, ions start diffusing from the bulk towards the electrodes. On the other hand, products generated at the surface of the electrodes diffuse from the electrode towards the bulk solution, i.e., where their concentration is low. Based on Fick's first law of diffusion, the diffusive flux is proportional to the concentration gradient with the proportionality coefficient called *diffusivity*. Since ions are diffused down a negative concentration gradient, diffusive flux for ionic species normally includes a negative sign as shown below:

$$\mathbf{N}_{diff} = -D_i \vec{\nabla} c_i \tag{2.17}$$

where D_i (a positive number) is the *diffusivity* of each species.

Migration Flux:

As soon as a cell starts generating current, species are consumed and a non-uniform concentration field is developed in the electrolyte. A non-uniform concentration field induces a non-uniform electric potential in the electrolyte, called *ionic potential*. Any gradient in the ionic potential can electrostatically force the ions to migrate from regions of high potential to regions of low potential. It should also be noted that when an electric potential is applied to the electrodes its surface becomes charged. Such an electrode can attract or repel charged species in the electrolyte adjacent to its surface. And this can further contribute to ion migration. The flux of ions due to migration can be modelled as:

$$\mathbf{N}_{mig} = -Z_i \xi_i \left(c_i \vec{\nabla} \varphi_f \right), \tag{2.18}$$

where Z_i is the species *charge number*, ξ_i is its mobility, c_i is the concentration of that ion in the bulk, and φ_f is the ionic potential in the electrolyte.

Knowing the flux contribution by each mechanism, the total flux becomes [19]:

$$\mathbf{N}_{net,i} = \mathbf{u}_j c_i - D_i \vec{\nabla} c_i - Z_i \xi_i \left(c_i \vec{\nabla} \varphi_f \right). \tag{2.19}$$

Based on the Nernst-Planck equation, conservation of mass for each charged species requires that in a partially saturated porous electrode we should have:

$$S\left(\frac{\partial c}{\partial t} \right) + \nabla \cdot \mathbf{N}_i = 0, \tag{2.20}$$

where S is the moisture content also called *saturation*. Assuming that the solution is sufficiently dilute, mobility of each species can be related to its diffusivity by the relationship: (F/RT) Di. Thus, we have:

$$\xi_i = \frac{F}{RT} D_i, \tag{2.21}$$

Thus, we obtain:

$$S\left(\frac{\partial c_i}{\partial t} \right) - \underbrace{D_i \nabla^2 c_i}_{\text{diffusion}} + \underbrace{\mathbf{u} \cdot \vec{\nabla} c_i}_{\text{advection}} - \underbrace{Z_i \frac{F}{RT} D_i \left(c_i \nabla^2 \varphi_f + \vec{\nabla} c_i \cdot \vec{\nabla} \varphi_f \right)}_{\text{migration}} = 0. \tag{2.22}$$

This partial-differential equation is valid for the species in the whole domain whether they reside in the electrode or in the pad. But, for the species that exist inside the electrodes this equation needs a source/sink term on its right-hand-side. Denoting the sink/source term by **R**, for each species it can be related to its surface concentration and its concentration in the bulk electrolyte; that is:

$$\mathbf{R}_i = \left[k_m A (c^s - c) \right]_i \quad , \quad i = \text{II}, \text{III}, \text{IV}, \text{V} \tag{2.23}$$

where k_m is the mass-transfer coefficient. On the other hand, the source/sink term can be related to the current density of each electrode as shown below:

$$\mathbf{R}_{II} = -\mathbf{R}_{III} = -\,a\,j_a\,/\,F, \tag{2.24a}$$

$$\mathbf{R}_{V} = -\mathbf{R}_{IV} = -\,a\,j_c\,/\,F, \tag{2.24b}$$

where “a” is the specific area of an electrode. The mass-transfer coefficient (k_m) in Eq. 2.23 is a comprehensive property which is controlled by many factors such as viscosity and density of the electrolyte, tortuosity and porosity of the electrode, the diffusivity of the ions/species involved in the system, and also the diameter of the carbon fibers. The dimensionless mass-transfer coefficient, called Sherwood number (Sh), can be correlated with the Reynolds number (Re) and the Schmidt number (Sc) as shown below [25-29]:

$$Sh = f(Re,Sc) = m + n_1\left(Re^{n_2}\,Sc^{n_3}\right), \tag{2.25}$$

where (m, n_1, n_2, n_3) are fitting parameters to experimental data. In this equation, “m” is the *diffusion-limited* Sherwood number (i.e., the Sherwood number corresponding to zero flow rate). The limiting value of the Sherwood number has been reported to be roughly equal to m = 2 for fully-saturated materials [27,28]. For such materials, we can use the recent correlation proposed by Barton and Brushett [29], as shown below:

$$Sh = 2 + 0.018\,Re^{0.68}\,Sc^{0.50}. \tag{2.26}$$

In this equation, we have:

$$Sh = \frac{K_m d_f}{D} \quad ; \quad Re = \frac{\rho U d_f}{\mu} \quad ; \quad Sc = \frac{\mu}{\rho D} \tag{2.27}$$

where d_f is the fiber dimeter, D is the diffusivity, U is the *superficial* velocity (i..e., flow rate divided by projected area of the electrode), μ is the dynamic viscosity, and ρ is the density. It needs to be mentioned that while the Reynolds number is the ratio of inertial force to viscous force, the Schmidt number is the ratio of momentum diffusion to mass diffusion. Now, before proceeding any further, we should note that for porous electrodes, the diffusivity (D) of the ions should be replaced with the *effective* diffusivity (D_{eff}), which can be obtained using the Bruggeman correlation [24]:

$$D_{eff} = \varepsilon^{3/2} D. \tag{2.28}$$

As the next step in our electrochemical modelling, we can relate the current density of each electrode (j) to its local current density vector (**i**) through the law of charge conservation; that is:

$$\left(\nabla \cdot \mathbf{i}_f\right)_a = -\left(\nabla \cdot \mathbf{i}_s\right)_a = a\, j_a, \tag{2.29a}$$

$$\left(\nabla \cdot \mathbf{i}_f\right)_c = -\left(\nabla \cdot \mathbf{i}_s\right)_c = a\, j_c, \tag{2.29b}$$

where $\mathbf{i}_f$ and $\mathbf{i}_s$ represent the ionic and electronic current density vectors, respectively. The electronic current density vector of an electrode can be related to its electronic potential through the Ohm's law:

$$\mathbf{i}_s = -\sigma_s \vec{\nabla} \varphi_s, \tag{2.30}$$

where σ_s is the electronic conductivity of the electrode material. By taking the divergence of Eq. 2.30, we can relate an electrode's potential to its current density. But before doing this, we should note that for porous electrodes the electronic conductivity should be converted to the *effective* conductivity using the Bruggeman correlation [24]; that is:

$$\sigma_{s,eff} = \left(1 - \varepsilon\right)^{3/2} \sigma_s. \tag{2.31}$$

With this little adjustment, we reach the Poisson equation for the electrode potential. From this linear PDE, we can obtain φ_s knowing the cathode's current density, j_c:

$$\sigma_{s,eff} \left(\nabla^2 \varphi_s\right)_c = a\, j_c. \tag{2.32}$$

To find the ionic potential in the electrolyte, we start by noting that ionic current can be written as:

$$\mathbf{i}_f = F \sum_i Z_i \mathbf{N}_i. \tag{2.33}$$

On the other hand, based on Eq. 2.22 one can conclude that ionic current-density vector is governed by the bulk concentration, ionic potential, and the velocity field of the electrolyte. But, since the electrolytes are assumed to be electrically neutral (i.e., $\sum_k Z_k c_k = 0$), the velocity field drops from this equation so that we obtain:

$$\mathbf{i}_f = -F \sum_i Z_i D_i \vec{\nabla} c_i - \sigma_f \nabla \varphi_f, \tag{2.34}$$

where σ_f is the electrolyte conductivity defined as:

$$\sigma_f = \frac{F^2}{RT} \sum_i Z_i^2 D_i c_i. \tag{2.35}$$

To find the ionic potential, φ_f, we just have to find the divergence of $\mathbf{i}_f$ in Eq. 2.34 to obtain the following equation:

$$-\sigma_f \nabla^2 \varphi_f + F \sum_i D_i Z_i \left(\nabla^2 c_i \right) = a j_c, \tag{2.36}$$

where we have assumed that the current is collected from the cathode. It is to be noted that, in cases where we can ignore the migration flux, the second term on the left-hand-side of this equation can be dropped so that we end up with another Poisson equation this time around for the ionic potential, φ_f.

To close our electrochemical modelling, we need the velocity field because it controls the Reynolds number and thereby the Sherwood number. To that end, we should note that while the above formulations are common between large-scale and small-scale (say, microfluidic) flow cells, our main interest in the present work lies in microfluidic flow cells [29-31]. Fortunately, microfluidic systems normally work under creeping-flow conditions. This is particularly true for paper-based cells or cells employing flow-through porous electrodes. Thus, in principle, we can rely on the Darcy's law for obtaining the velocity field, which is a linear empirical law in its original form [32,33]. The problem is that for an unsaturated paper-based microfluidic flow cell, permeability and capillary

pressure are nonlinear functions of the moisture content. Thus, we have to rely on the highly-nonlinear saturation form of the Darcy's law for modelling liquid imbibition, which is quite difficult to solve even numerically.

2.4. Imbibition Modelling

As earlier mentioned, paper-based microfluidic flow-cells utilize the wicking effect of cellulosic papers to drive the working water-based electrolytes [34]. The wicking property causes a wetting liquid such as water to *spontaneously* displace a non-wetting fluid such as air from the pores of a cellulosic paper through capillary forces—a process called "spontaneous imbibition". Figure 2.4 shows what is meant by "spontaneous imbibition". As can be seen in this figure, water is imbibed by a dry brick as soon as it is brought in contact with the brick's lower plane. Liquid then starts to climb the brick even against the gravity. This figure clearly shows that imbibition is a slow process. It also shows that it is a nonlinear process.

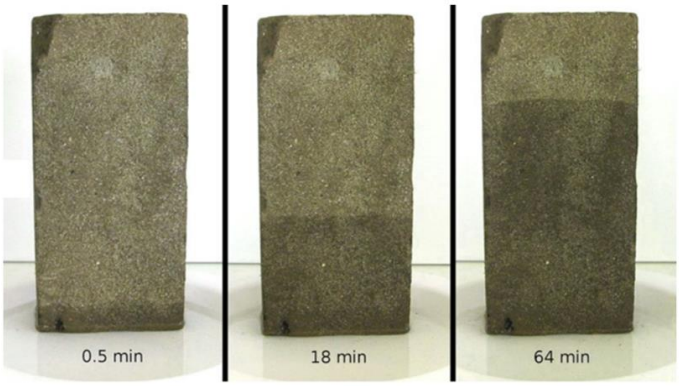

Figure 2.4. Imbibition of water into a dry brick at different times.

For design purposes, liquid imbibition and the flow rate established by a cellulosic paper (when used in a paper-based electrochemical cell) must be properly modelled. In the next section, two imbibition models in common use are introduced in some details.

2.4.1. Lucas-Washburn model

Lucas and Washburn model [36,37] is perhaps the simplest and therefore the most widely-used imbibition model for designing paper-based systems. They first modeled a porous medium by a bundle of parallel capillary tubes all having the same dimeter. For a representative tube, they assumed that the flow is laminar and the tube is long enough for Poiseuille equation to be valid. This classic equation relates the flow rate in a tube (Q) to its diameter (d), fluid's viscosity (μ), and the pressure difference between the two ends of the tube (Δp) as given below:

$$Q = \frac{\pi d^4}{128\mu}\left(\frac{\Delta p}{L}\right), \tag{2.37}$$

where L is the length of the tube; see Fig. 2.5.

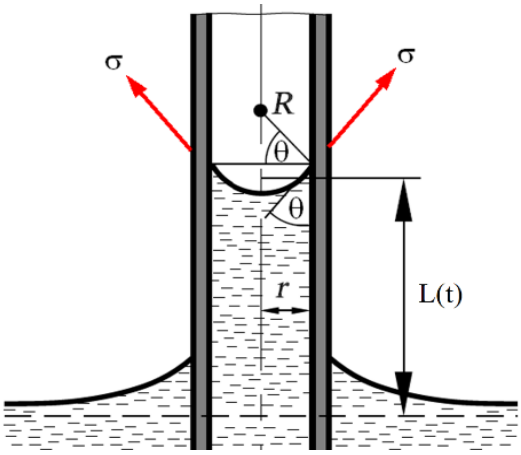

Figure 2.5. Modelling imbibition in a porous material by a capillary tube.

Lucas and Washburn model [36,37] assumed that the flow is driven by the capillary pressure, and so they replaced $\Delta p/L$ by p_c/L; that is:

$$Q = \frac{\pi d^4}{128\mu}\left(\frac{p_c}{L}\right). \tag{2.38}$$

They also assumed that this equation is valid at each instant of time, i.e., during the transient phase of the capillary-rise phenomenon. But during this transient phase, Q(t) can also be related to L(t) as shown below:

$$Q(t) = AU = \frac{\pi d^2}{4}\frac{dL}{dt}, \tag{2.39}$$

where U = dL/dt is the average velocity. By combining Eq. 2.38 with Eq. 2.39 Lucas and Washburn reached to the following equation for L(t):

$$LdL = p_c\left(\frac{d^2}{32\mu}\right)dt = \frac{2\Gamma}{R}\left(\frac{d^2}{32\mu}\right)dt \quad \Rightarrow \quad L(t) = \sqrt{\left(\frac{\Gamma d\cos\theta}{4\mu}\right)t}\ , \tag{2.40}$$

where Γ is the surface tension, and θ is the contact angle. Another look at this equation reveals that it has the nature of diffusion phenomena because the dependent parameter varies with the square root of time. For this reason, this equation is sometimes recast in the form of: $L(t) = \sqrt{Dt}$, where D is the so-called viscosity-scaled diffusivity defined as:

$$D = \frac{\Gamma d\cos\theta}{4\mu}. \tag{2.41}$$

In spite of its apparent simplicity, Lucas-Washburn equation was found to reasonably well represent liquid imbibition in certain homogeneous porous materials such as bricks. Although this simple model was widely used in the past for designing paper-based microfluidic systems, it must be said that it has many shortcomings [38]. The most serious drawback of this equation is that it models a porous material by a single tube size while porous materials are often realized to have a broad range of pore sizes. Another shortcoming of their model is that Lucas and Washburn [36,37] did not give any clue as to how this representative diameter should be determined. Moreover, the Lucas-Washburn model is based on the assumption that the material is fully saturated behind the advancing front—an assumption which is often realized not to be true. To these should be added the fact that Lucas-Washburn model is a one-dimensional model and this severely limits its range of applicability. In addition, the model cannot represent multi-layered materials such as PowerPAD where the system is two-layered.

2.4.2. Richards Equation

Richards equation is one of the simplest theoretical models available in the literature for predicting liquid imbibition in unsaturated porous materials [39]. This robust theoretical model was originally derived for modelling diffusion/infiltration of moisture in granular materials such sands and rocks. It took the imbibition community roughly 70 years to realize that this robust model works as well for modelling imbibition in fibrous materials such as filter papers, which are made of non-woven cellulosic fibers [40]; see Figure 2.6. A literature review has revealed that, quite surprisingly, this imbibition model has not been used in the past for designing any paper-based flow battery.

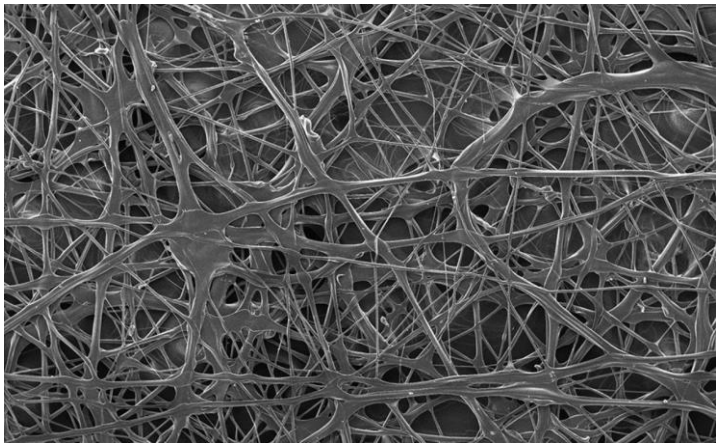

Figure 2.6. A typical non-woven, cellulosic material used in filter papers.

It is worth mentioning that Richards model ignores the viscous drag introduced by the displaced fluid. In other words, it is a *single-phase* porous-media model in which the effect of the displaced fluid asserts itself only through surface tension. So, in a sense, it best represents unsaturated porous beds in which the displaced fluid exists as entrapped pockets. Interestingly, however, it has been found to be valid also for two-phase systems where the displaced fluid is a flowing gas. Thanks to the small viscosity of gases such as air the viscous drag caused by the gas flow can be ignored in comparison with that caused by the displacing (or, invading) liquid. Figure 2.7 schematically shows different scenarios that might emerge in real world for a porous

bed eligible to be modelled using the Richards equation. Its range of applicability is seen to span fully-saturated beds and two different types of unsaturated beds. In other words, Richards equation can be used with adequate accuracy for modelling all three cases depicted in this figure, subject to the main restriction that the non-wetting phase (air) introduces no viscous drag.

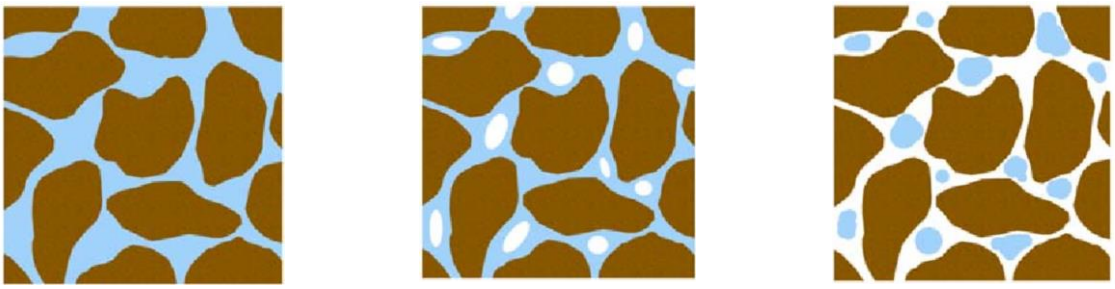

(a) (b) (c)

Figure 2.7. Schematic showing different types of flow through a porous bed: (a) fully-saturated bed; (b) single-phase unsaturated bed, and (c) two-phase unsaturated bed.
An open access article [41] under creative commons license (CC0 1.0 Universal Public Domain Dedication).

Richards equation is derived starting from the Darcy's law in which permeability and pressure terms are allowed to vary with moisture content (S) [39]:

$$\vec{\mathbf{q}} = -\frac{k(\mathbf{r},S)}{\mu}\left[\vec{\nabla} p_c(\mathbf{x},S)\right], \tag{2.42}$$

where $\vec{\mathbf{q}}$ is the flux of the liquid, k(**x**,S) is the saturation-dependent permeability, $p_c(\mathbf{x},S)$ is the saturation-dependent capillary pressure, and **x** is the position vector. In this equation, S is the degree of *saturation* for the wetting phase, which is defined as: $S = \beta/\varepsilon$ where β is the volume of liquid imbibed by the porous material, and ε is the total volume of its void spaces (called *porosity*). Since β varies between 0 and ε, it is evident that S varies between 0 and 1. The flux vector in the Darcy's equation can be

related to the saturation field, S(**x**,t), through the continuity equation for the liquid phase. This equation can be written as [39]:

$$\varepsilon\left(\frac{\partial S}{\partial t}\right) = -\nabla\cdot\vec{\mathbf{q}}. \tag{2.43}$$

By combining Eq. 2.42 and 2.43, we can obtain the *mixed* form of the Richards equation, which incorporates both the saturation and the capillary pressure:

$$\frac{\partial S}{\partial t} = \nabla\left(\frac{k(\mathbf{r},S)}{\varepsilon\mu}\nabla p_c(\mathbf{r},S)\right). \tag{2.44}$$

Although the mixed form is appropriate for multi-layered systems, thanks to its ease of boundary conditions, the *saturation* form of the Richards equation (i.e., the form which incorporates just S) is more commonly used in numerical simulations. The saturation form of the Richards equation can be obtained by writing the capillary pressure as:

$$\vec{\nabla}p_c(\mathbf{r},S) = \frac{\partial p_c}{\partial S}\vec{\nabla}S. \tag{2.45}$$

With this little maneuvering, the Richards equation becomes:

$$\frac{\partial S}{\partial t} = \nabla\cdot\left[\frac{k(\mathbf{x},S)}{\varepsilon\mu}\left(\frac{\partial P_c(\mathbf{x},S)}{\partial S}\right)\vec{\nabla}S\right] = \nabla\cdot\left[D(\mathbf{x},S)\vec{\nabla}S\right], \tag{2.46}$$

where, $D(\mathbf{x},S)$ is the so-called *viscosity-scaled diffusivity*. Based on the Brooks and Corey correlations [42] (see Appendix A), the diffusivity can be written as:

$$D(S) = D_0 S^n \tag{2.47}$$

where for fibrous materials, we can use Huinink equation for obtaining the maximum diffusivity, D_0 [43]:

$$D_0 = \frac{\Gamma}{\mu\lambda}\left(\frac{d_{max}\cos\theta}{2}\right). \tag{2.48}$$

In this equation, $\lambda = 1/(n-2)$ is an index indicating the degree of tortuosity of the porous material—the smaller, the better. These two model parameters (n, D_0) can be obtained by fitting Richards model predictions to the imbibition data of the porous material used in any cell; see Chapter 4. Having found the saturation field, S(**x**,t), it can be inserted in the modified Darcy's law to find the velocity field, as shown below:

$$\mathbf{u} = \frac{K(S)}{\mu}\nabla p_c = \frac{K(S)}{\mu}\frac{\partial p_c}{\partial S}\nabla S = -\frac{K_{max}P_{min}}{\mu\varepsilon\lambda}S^{(2+1/\lambda)}\nabla S. \tag{2.49}$$

The velocity field obtained this way can then be used in the advection-diffusion mass-transport Fick's equation to find the time-evolution of the concentration field for each species. The velocity field can also be used to calculate the Reynolds number as a function of time.

2.5. Summary

In this Chapter we have presented some basic knowledge about the mathematical modelling of a general class of paper-based, capillary-driven electrochemical cells. The methodology comprises imbibition modelling in addition to electrochemical modelling. In the next Chapter we will apply this two-step model to a novel paper-based, capillary-driven flow cell called PowerPAD.

Chapter 3:

Mathematical Modelling of PowerPAD

3.1 Introduction

In Chapter 2, a systematic theoretical methodology was developed for designing a general class of paper-based microfluidic flow batteries. The methodology can be applied to any paper-based flow cell provided that the kinetics of its redox couples is known. In this Chapter we apply the methodology to the PowerPAD flow cell, which is an all-quinone capillary-driven microfluidic flow cell.

3.2 PowerPAD Characteristics

As mentioned in Chapter 1, the main objective of this work is to understand how paper-based capillary-driven flow cells work and how to model them. In other words, understanding the unique functionality of this type of flow cells and what factors control their power output and runtime are our main objectives in this research work. We are also interested in identifying viable options through which we can enhance the performance of such cells, and this requires a proper parameter study to figure out appropriate design optimizations. Although our methodology is general and could be applied to any such cells, here we apply it to the PowerPAD (as our primary battery) for which experimental data are available in the literature [16]. An experimentally-validated model can be used as an efficient tool for design optimization of this flow cell and cells similar to that.

Figure 3.1 shows an exploded view of the PowerPAD. The cell is activated when a drop of water is placed on its sample pad. The solid electrolytes placed right below the sample pad are then dissolved and the liquid electrolytes produced this way are imbibed by the electrodes (from their top planes) so that electrochemical reactions can take place on its bare carbon fibers. In the current design, the fluids flow directly through the electrodes in the vertical direction. But, as soon as they enter the absorbent pad they start diffusing in the lateral direction until they come into contact with each other at

some point in time. The two liquids then continue flowing co-laminarly downwards and exchange ions at their interface before being collected by an absorbent pad. This process is continued until the pad becomes fully-saturated and the flow rate drops to zero. For reasons to be discussed in Chapter 5, the cell continues generating power until it is depleted of its active reactants. The cell is then disposed of at the end of its working life with no harm to the environment.

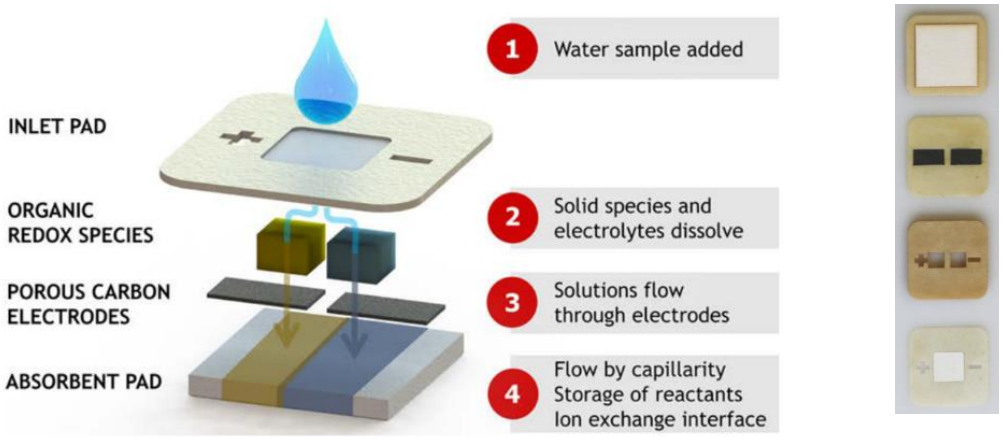

Figure 3.1. Schematic depicting the main components of the PowerPAD.

An open access article [16] reproduced with permission from Wiley and Sons.

It is important to note that PowerPAD is a 3D cell because the saturation fields in its electrodes and absorbent pad depend on all three spatial Cartesian coordinates (x,y,z), which is the coordinate to be used for mathematical formulation. As to the dimensions of the key components of this flow cell (i.e., the electrode and the absorbent pad), based on the data given in [16], we have:

Electrode Dimensions: 5 mm x 5 mm x 0.37 mm.

Absorbent Pad Dimensions: 20 mm x 20 mm x 0.83 mm.

For the absorbent pad, 0.83 mm (underlined above) refers to the thickness of the base sheet of filter paper as received from the manufacturer. By stacking different layers of the base sheet, other thicknesses could be obtained for use as absorbent pad. In [16] the maximum thickness was labelled 4h obtained by stacking four layers of the base sheet thickness (labelled h).

Another important dimension of the cell is the gap between the electrodes which was set at 2 mm in [16]. Based on the experimental data reported in [16], the power density of the PowerPAD is around 7 mW/cm^2. We also know that the thickness of the absorbent pad can be used to control the polarization curve of the cell. In fact, the maximum output power (which is equal to 1.7 mW) could be obtained with the thickest pad, labelled 4h in Fig. 3.2. Another look at this figure reveals that the open-circuit-voltage (OCV) of the cell is roughly equal to 0.8 V (with an error of ±0.5 V) [16].

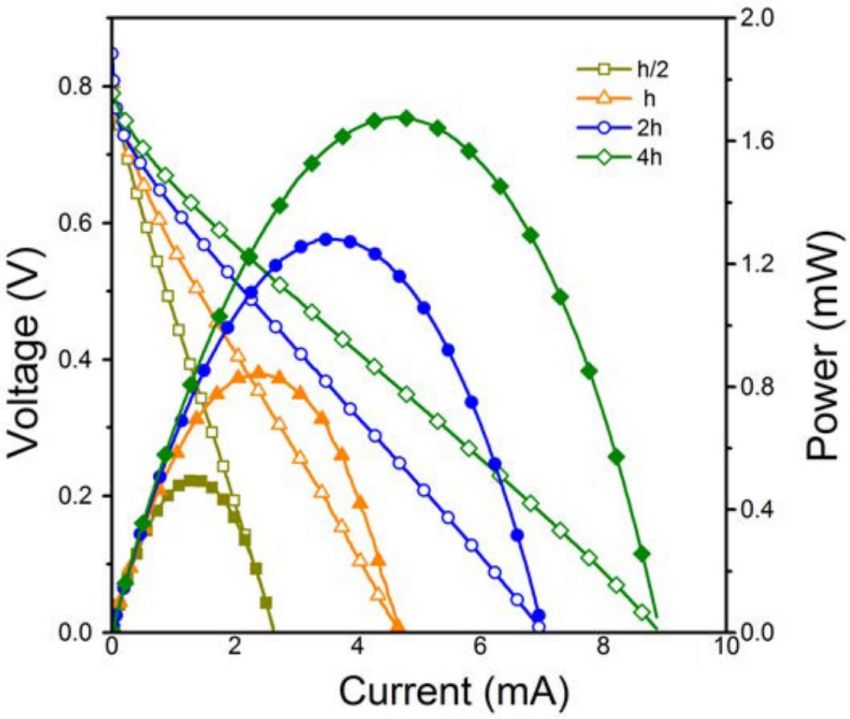

Figure 3.2. Discharge polarization curves of PowerPAD flow battery.

An open access article [16] reproduced with permission from Wiley and Sons.

Another important characteristic of this cell is that, when it is operated at the lowest load, it delivers a higher power output but for a shorter service time. In contrast, when it works under the highest load (2 kΩ), it delivers a lower power output for longer operation times; see Fig. 3.3. Moreover, for any given load, the power output and runtime of the cell is improved with thicker absorbent pads; see Fig. 3.3. Also, depending on the thickness of its absorbent pad and the magnitude of the external load, the cell can continue generating power for more than an hour. In fact, the longest

runtime of the cell, which was around 85 min, was obtained using the 4h-pad system for an external load of 2000 Ω; see Fig. 3.3. This particular system, which will be referred to as 4h-2000 case in subsequent sections, will serve as our “base case” in the rest of the work. To be more specific, our parameter study and design optimizations will be devoted to this particular system.

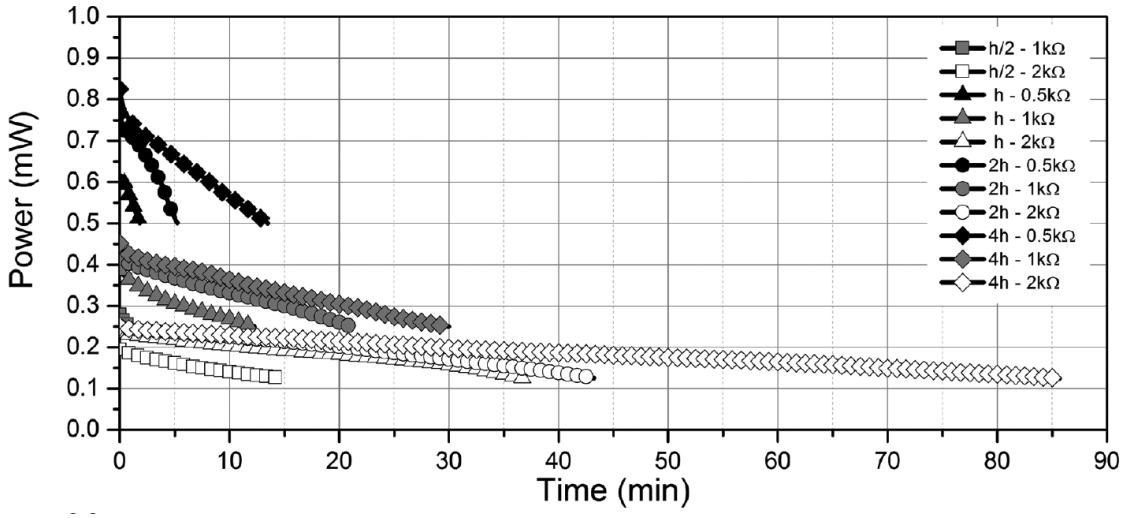

Figure 3.3. Effect of pad thickness on the performance of PowerPAD.
An open access article [16] reproduced with permission from Wiley and Sons.

A parameter study needs a mathematical model at the first place. The mathematical model developed in Chapter 2 is applicable to the PowerPAD provided that the model is fine-tuned to the kinetics of the quinone redox couples used in this particular cell. The problem is that, as mentioned above, PowerPAD is a three-dimensional cell and this can make obtaining numerical results in due time difficult. Further complication arises from the notion that the electrode and the pad materials have different microstructures. As a result, the boundary conditions at their interface turn out to be highly nonlinear (see Chapter 4) and this can further complicate obtaining converged numerical analysis. The fact that the system is initially unsaturated and remains partially saturated during its transient phase of operation means that we have to rely on the saturation form of the Darcy’s equation (i.e., the Richards equation) which is, as earlier mentioned, quite difficult to solve even numerically. To reduce the likelihood of any numerical instability and/or convergence issues, some simplifying assumptions are definitely needed in our

mathematical formulations. In the next section these assumptions are presented and their suitability is discussed.

3.3 Simplifying Assumptions

There are several simplifying assumptions/approximations that are commonly used in the electrochemistry community when modelling/simulating microfluidic flow batteries. The main assumptions used in the present work are:

- Electrolytes are incompressible.
- Physical and electrochemical properties of materials/species are constant.
- Temperature is uniform throughout the domain.
- Flow is occurring under creeping conditions.
- Electrolytes always remain electrically neutral.
- Dilute-solution theory is applicable.
- Two-dimensional analysis is adequate.

Also, although in Chapter 5 we will consider the effect of parasitic electrochemical side-reactions in our analysis, we intend to exclude side-reactions such as hydrogen evolution (due to water decomposition) and CO_2 evolution (due to oxidation of carbon-based electrodes) from our analysis.

Even with so many assumptions and approximations, it is speculated that, qualitatively, we should be able to validate our mathematical model with the experimental data reported for the PowerPAD in [16]. Slight deviation(s) from these assumptions is probable in the real world, and so we should prepare ourselves for some quantitative differences between model predictions and the experimental data published in [16]. What is important is that the physics of the problem should not be grossly affected by any of these assumptions, and this can only be judged by comparing model predictions with experimental data.

The assumption that temperature remains constant during the PowerPAD's operational lifetime is a *critical* one because, in general, electrochemical reactions are known to be exothermic. And a temperature rise can indeed affect a cell's performance through affecting the transport properties of its electrolytes (for example, viscosity) and its redox species (for example, diffusivity). But the fact is that there is no mentioning of any

temperature rise in [16] and this suggests that perhaps temperature rise was insignificant for this particular flow cell [16]. And this is the main reason why we have resorted to the constant-temperature assumption in this work. This is fortunate because temperature rise can significantly add to the complexity of any mathematical model. To be more specific, temperature-dependent mathematical models require that the transport properties involved in the cell is correlated with time through appropriate (empirical) equations, and these equations are simply not available for quinone species used in the PowerPAD. Another problem with the temperature is that any temperature gradient in the cell gives rise to heat transfer. This means that the energy equation should also be solved coupled with other equations involved in the problem and this further complicates the analysis. Due to the pioneering nature of the present work, such complications were considered to be beyond the scope of the present work; see, Chapter 7.

Another key assumption of the work is that the PowerPAD (which is a 3D device) can be represented by a 2D model. Due to its importance, in the next section we elaborate more on this assumption.

3.4 Two-Dimensional Model

As mentioned above, PowerPAD is a three-dimensional flow cell. Thus, in principle, one should go for a 3D analysis for its evaluation and optimization. The problem is that a 3D study is computationally very demanding. For example, while a 2D run may take just 20 min to converge on a personal computer (for steady mode of operation), a 3D run may need a full day to converge—if it ever converges. In a stimulating numerical work, Krishnamurthy et al. [44] showed that for pressure-driven microfluidic flow cells equipped with flow-through electrodes, the difference between 2D and 3D results was less than 2%. With this in mind, a 2D analysis was adopted in the present work to represent the PowerPAD. In Chapter 5 we will show that numerical results obtained using the 2D analysis closely match *steady* experimental data reported in [16] for the PowerPAD. Validating the 2D model with 3D data in *unsteady* mode of operation turned out to be more challenging; see Chapter 5.

Figure 3.4 schematically shows the 2D geometry adopted in this work for representing the PowerPAD. This figure also shows the Cartesian coordinate system used for the mathematical development and its origin. It is important to note that in the current design (called “vertical-flow design”) the fluids cannot enter the gap between the two electrodes either because the inner side-planes were made impermeable using beeswax or due to the impeding action of surface tension at these side-planes.

In any 2D analysis, one of the coordinates will serve as the neutral direction. In the present work, it is assumed that the y-direction is this direction. In other words, there will be no gradient in the y-direction for any variable involved in our physical problem. This also means that the flow is restricted to the xz-plane; see Fig. 3.4. To predict the electrochemical behavior of the PowerPAD, we have to decide on the equations which govern this 2D cell. Note that our 2D model differs from the 3D geometry only in the width of the absorbent pad. That is to say that, the length/width/height of the electrodes are the same for both celss. But, while in the 2D model the width of the pad is 5 mm, for the 3D device it is equal to 20 mm. As such, the volume of the two pads are different from each other. To be more specific, the volume of the 3D cell is roughly *four* times that of the 2D cell. This ratio plays a key role in our unsteady analysis when we try to validate our 2D model against 3D experimental data; see Chapter 5.

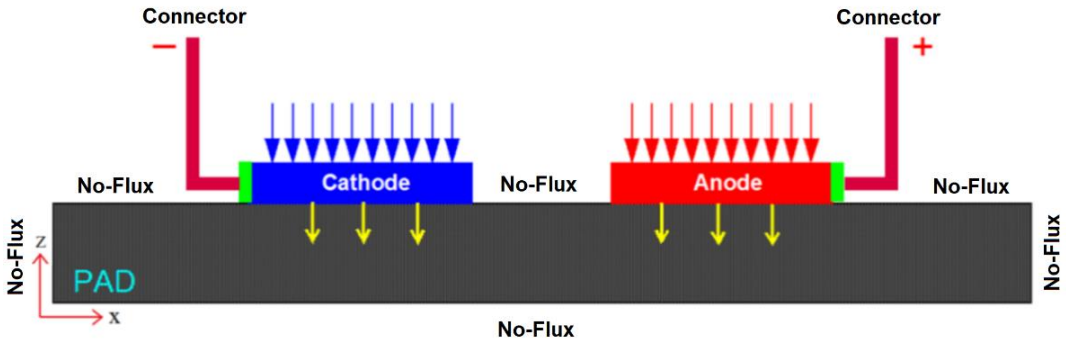

Figure 3.4. Schematic showing the 2D model used for representing the PowerPAD (not to scale).

3.5 Governing Equations

The equations governing the 2D cell depicted in Fig. 3.4 include those controlling its electrochemical behavior and those controlling its imbibition characteristics. So, our mathematical model comprises two steps.

3.5.1 Electrochemical Equations

PowerPAD is an all-quinone cell. In this particular cell H_2BQS (dissolved in KOH base) serves as the fuel with pBQ (dissolved in C_2H_2O4 acid) as the reductant. Oxidation of the fuel produces electrons in the negative half-cell which are transferred to the positive half-cell and consumed by the reductant. The kinetics of the quinone redox couples used in the PowerPAD are quoted to be as shown below [45]:

Negative Half-Cell: $\mathrm{H_2BQS^- \Leftrightarrow BQS^- + 2e^- + 2H^+}$ (3.1)

Positive Half-Cell: $p\mathrm{BQ + 2H^+ + 2e^- \Leftrightarrow H_2BQ}$ (3.2)

The cell is seen to produce two electrons (n = 2) which is generally regarded as a good feature for quinone redox couples. Note that the first reaction produces two protons that can contribute to the second reaction after diffusing to the positive half-cell. Note also that the negative half-cell involves OH^- ions but they do not get involved in any kind of electrochemical reactions [45]—their main role is to ensure that a larger negative potential can be generated in the negative half-cell. So, all in all, five ions/species are directly involved in the electrochemical reactions for this particular flow cell: H_2BQS, BQS, pBQ, H_2BQ, and H^+. Among these, H_2BQS and pBQ are the *active* species whereas BQS and H_2BQ are the products. In analogy with vanadium species, in subsequent sections the four quinone species used in the PowerPAD will be denoted by: C_{II}, C_{III}, C_{IV}, and C_V. With KOH used as the *basic* electrolyte in the negative side and $C_2H_2O_4$ as *acidic* electrolyte in the positive side, the cell obviously works based on the mixed-media concept, which is good at the time of the cell's disposal as they can neutralize each other. Of key importance in our analysis is the equilibrium potential of the negative and positive half cells which are, respectively, equal to –0.46 V and +0.49 V (vs. SCE). Thus, the cell's theoretical OCV is equal to 0.95 V. Table 3.1 presents the

kinetic and transport properties of the quinone species used in the PowerPAD [46]. For comparison purposes, diffusivity of H^+ and OH^- have also been given in this table.

Table 3.1. Kinetic properties of quinone species used in the PowerPAD [46].

Species	Diffusion Coefficient (D) ($cm^2.s^{-1}$)	Charge Transfer Coefficient (αn)	Rate Constant (k) ($cm.s^{-1}$)
H_2BQS/BQS	5.03×10^{-6}	0.508	2.36×10^{-3}
pBQ/H_2BQ	3.80×10^{-6}	0.582	1.55×10^{-4}
H+	9.30×10^{-5}	—	—
OH–	6.80×10^{-5}	—	—

The concentration of H_2BQS (fuel) used in the PowerPAD was equal to 0.2 M and this active species was dissolved in 2 M potassium hydroxide (KOH) as the anolyte. On the other hand, the concentration of pBQ (oxidant) was 0.2 M and it was dissolved in 1 M oxalic acid ($C_2H_2O_4$). For convenience, these data have been tabulated in Table 3.2. The species concentrations used in the PowerPAD are small enough to warrant labeling these solutions as *dilute*.

Table 3.2. Initial concentration of quinone species in the PowerPAD [16].

Species	Concentration	Role
H_2BQS/BQS	0.2 M / 0 M	Fuel/Product
pBQ/H_2BQ	0.2 M / 0 M	Oxidant/Product
$C_2H_2O_4$	1 M	Catholyte
KOH	2 M	Anolyte

Of crucial importance in our theoretical analysis of the PowerPAD is the Nernst equation representing its kinetics. Based on the kinetics of the redox couples given by Eq. 3.1 and 3.2, the Nernst equation for the whole cell can be written as [47]:

$$OCV = E^{+} - E^{-} = 0.95 + \frac{RT}{2F}\ln\left(\frac{\left[c_{H_2BQS}\right]\cdot\left[c_{pBQ}\right]\cdot\left[\gamma_{H^+}c_{H^+}/c_{acid,0}\right]^2}{\left[c_{BQS}\right]\cdot\left[c_{H_2BQ}\right]}\right) \tag{3.3}$$

where $\gamma_{H^+} = 0.13$ is the activity of protons in the acidic media [48]. It is worth-mentioning that although this equation has an apparent singularity at $\left[c_{H_2BQ}\right] = 0$ or $\left[c_{BQS}\right] = 0$ these extreme values cannot be witnessed in the real world which is why, in practice, we always end up with a final value for the OCV. Note also that PowerPAD is a single-use cell which works in galvanic mode only, and so we always have: $\left[c_{H_2BQ}\right] \neq 0$. This is certainly true for the PowerPAD which has a non-zero SOC defined for each half cell as shown below:

$$SOC^{-} = \frac{\left[c_{H_2BQS}\right]}{\left[c_{H_2BQS}\right] + \left[c_{BQS}\right]} \quad ; \quad SOC^{+} = \frac{\left[c_{pBQ}\right]}{\left[c_{pBQ}\right] + \left[c_{HBQ}\right]} \tag{3.4}$$

where under equilibrium conditions we have: $SOC = SOC^{+} = SOC^{-}$. The SOC of PowerPAD has not been explicitly mentioned in [16]. But based on the data reported in [45] for a similar but pressure-driven microfluidic cell, it appears to be around 95%. (Which is also the SOC for which the data in Table 3.1 have been obtained experimentally in [46].) In terms of SOC, the OCV of the PowerPAD can be re-written as:

$$OCV = 0.95 + \left(\frac{RT}{2F}\right)\ln\left(\frac{SOC\left[0.13C_{H^+}\right]}{1 - SOC}\right)^2 \tag{3.5}$$

Surpringly, the experimental OCV reported for PowerPAD in [16] is equal to 0.8 V whereas the value given by Eq. 3.5 is larger than 0.95 V (simply because the logarithmic term in this equation is positive in discharge mode). This discrepancy suggests that there are mechanism(s) involved in this particular flow cell that negatively

affect the cell's OCV. (For vanadium cells, in contrast, there are mechanisms that make the experimental OCV larger than its theoretical value [47].) The combined effect of all these mechanisms can be lumped into a constant denoted by Λ in the modified Nernst Equation shown below:

$$OCV = E^{+} - E^{-} = 0.95 + \frac{RT}{2F}\ln\left(\frac{\left[c_{H_2BQS}\right]\cdot\left[c_{pBQ}\right]\cdot\left[\gamma_{H^+}c_{H^+}/c_{acid,0}\right]^2}{\left[c_{BQS}\right]\cdot\left[c_{H_2BQ}\right]}\right) - \Lambda \qquad (3.6)$$

The experimental OCV can then be recovered by simply setting $\Lambda = 0.19$ V for SOC = 0.95 [46]. Figure 3.5 shows a plot of this equation. This figure shows that with this value for the $\Lambda-$term, the theoretical OCV becomes equal to 0.8 V for SOC = 0.95, as it should.

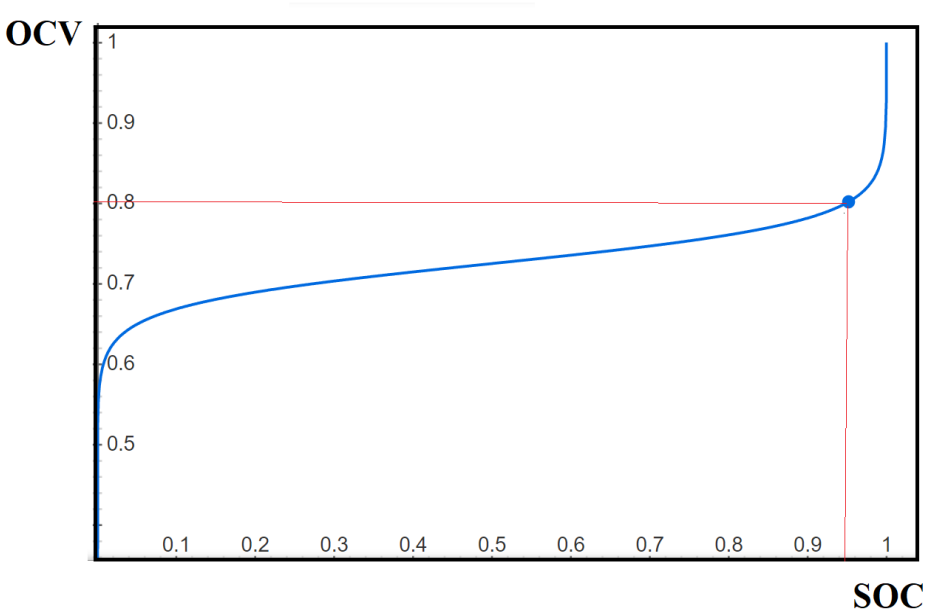

Figure 3.5. Variation of PowerPAD's OCV with SOC under steady conditions. The symbol in this figure corresponds to SOC = 0.95.

As to the physics behind the $\Lambda-$term, it can be argued that there are several effects that can simultaneously contribute to this term with one of them being the *activity* of ions. It is a well-established fact that in cells where convective mixing is absent (e.g., PowerPAD) strong ionic interactions makes the *activity* of the species less than one

[48]. In other words, in such cells the *effective* ions available for electrochemical reactions are always less than their *nominal* concentrations. This rule also applies to the protons that is known to have an activity equal to 0.3 in acidic media [49], as earlier mentioned—it is much less in basic media. Therefore, the activity of quinone species are expected to be less than one and not necessarily equal to each other.

Another mechanism that can significantly contribute to the $\Lambda-$term is the “Galvani potential drop” at liquid/liquid interface [50-53]. In the PowerPAD, Galvani potential drop is mainly caused by the *mobility* of H^+ ions being different at the two sides of the interface. The fact is that, as soon as the cell starts generating current, H+ is consumed in the positive half-cell and is generated in the negative half-cell. To conserve electro-neutrality, protons try to cross the interface. The problem is that in the PowerPAD the anolyte is *basic* whereas the catholyte is *acidic*. As such, the protons in each half-cell have a different *mobility* (say, *diffusivity*). A diffusional potential gradient is then developed at the interface in order to speed up the transport of protons in the negative side (which have a low mobility) and slow down the transport of protons in the positive half-cell (which have a high-mobility) [53]. The combined effect of mobility imbalance is the development of a sharp gradient in the electric potential at each side of the interface, as can be seen schematically in Fig. 3.6. As soon as *equilibrium* is reached, the net potential difference across the interface becomes much less than the theoretical potential, as can be seen schematically in Fig. 3.6.

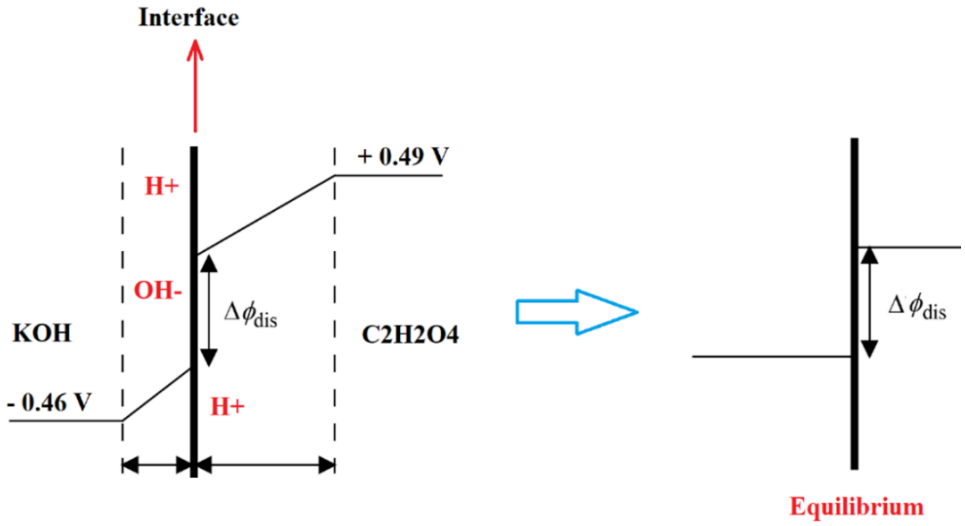

Figure 3.6. Development of Galvani potential drop at an interface.

The Galvani potential drop can be estimated using an equation similar to the Nernst equation [52]:

$$\Delta\phi = \Delta\phi^{0} + \frac{RT}{zF}\ln\frac{\left[\gamma_{H^+}c_{H^+}/c_{acid,0}\right]^{+}}{\left[\gamma_{H^+}c_{H^+}/c_{base,0}\right]^{-}}, \tag{3.7}$$

where $\Delta\phi^{0}$ is the standard transfer-potential of the ions crossing the interface—this potential is proportional to its Gibbs energy of transfer [53]. (A similar relation can be written for the other ions at the interface including OH^{-}.) The standard potential of ions has been reported in the literature to be in the range of 0.1 V to 0.5 V [53]. So, Galvani potential by itself can easily account for a major portion of the Λ−term in Eq. 3.4. It should also be mentioned that, as is well-established in the literature [54], all-quinone flow cells are very sensitive to pH-differential. For the PowerPAD, the pH-differential is initially equal to 10.5 but it drops as time progress starting from the interface. It is speculated that this effect may also have contributed to the Λ−term. We should also note that there are several other uncertainties which can contribute more or less to the Λ−term such as: i) temperature variation, ii) viscosity and density variation, iii) variation in the mass-transfer coefficient, and iv) uncertainty about the initial state-of-charge (SOC) of the cell.

Having decided on Eq. (3.6) as the final form of Nernst equation for the PowerPAD, we can now proceed with analyzing the unsteady mode of operation of this cell. During this mode of operation, species are consumed, and so the cell's SOC (and therefore its OCV) drops with time. Knowing SOC at an initial time $t = t_0$ we can obtain SOC at a later time $t = t_1 > t_0$ provided that variation of the current with time is known. The following equation can be used for determining SOC as a function of time in the *discharge* mode [55]:

$$\mathrm{SOC}(t_1) = \mathrm{SOC}(t_0) - \frac{\int_{t_0}^{t_1} I(t)dt}{q_{th}}. \tag{3.8}$$

where I(t) is the current and q_{th} is the theoretical capacity defined as:

$$q_{th} = n \cdot c_0 \cdot V \cdot F, \tag{3.9}$$

where c_0 is the initial concentration, V is the total volume of the electrolyte in the system, and F is the Faraday's constant. Figure 3.7 schematically shows what happens when an external load is connected to a flow cell such as PowerPAD. The point at which the load line intersects the polarization curve is called the *Operating Point*. Since the capacity of the cell is finite, polarization curve is time-dependent and shifts downwards as time progresses. As a result, the operating point also shifts downwards although it always stays on the load line. In other words, the cell generates less and less current (and therefore less power) as time progresses. Note that the internal resistance of the cell scales with the inverse of its instantaneous SOC which is why the slope of the polarization curves has been purposely made steeper and steeper in the course of time; see Fig. 3.7. This figure also shows that OCV is a decreasing function of time, as it should.

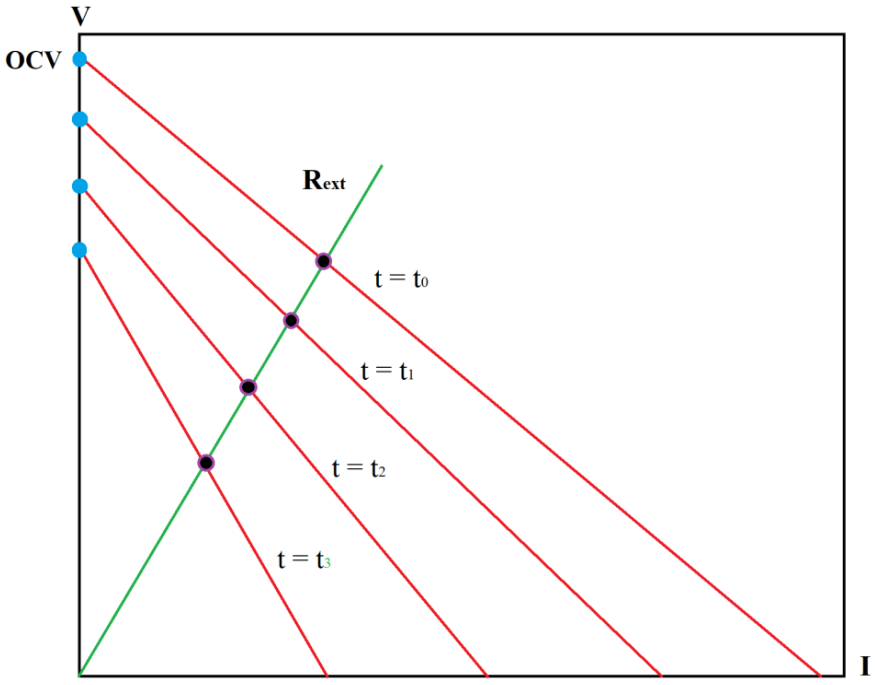

Figure 3.7. Schematic showing the operating point of PowerPAD and its variation with time.

Knowing voltage and current (V,I) at all operating points, we can plot power output as a function of time when an external load is connected to the PowerPAD. As will be discussed in Chapter 4, our numerical scheme requires that the potential of the cathode be given as an input boundary condition. The code can then compute the current density corresponding to this boundary condition. In Fig. 3.8 the voltage corresponding to several intersection points has been denoted by $V_0, V_1,$ and V_2. The question is how to find the voltage corresponding to these operating points as a function of time? To answer this question, it should be noted that at any given operating point, the cell voltage should satisfy Ohm's law dictated by the external load. That is to say that, at an arbitrary intersection point we should have:

$$V_{cell} = R_{ex} I \,, \tag{3.10}$$

where R_{ex} is the external load.

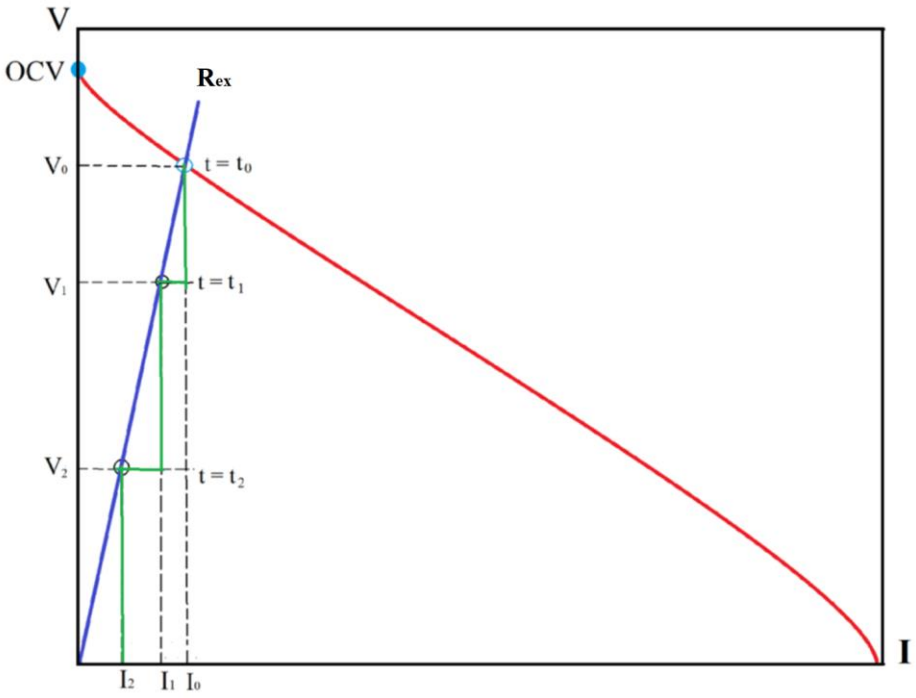

Figure 3.8. Variation of the operating points of a typical flow cell with time.

On the other hand, the cell voltage can be related to the cathode's potential (φ_s) and the cell's internal resistance, R_{in}, as shown below:

$$V_{cell} = \varphi_s - R_{in} I \,. \tag{3.11}$$

By combining Eq. (3.10) with Eq. (3.11) we obtain:

$$I = \frac{\varphi_s}{R_{ex} + R_{in}} \,. \tag{3.12}$$

where for sufficiently high R_{ex} we can drop R_{in} from this equation. In Appendix B we have shown in some details that the current (I) can also be related to the gradient of the cathode's potential in the x-direction $\left(\partial\varphi_s/\partial x\right)$ at the place where current connectors are glued. Thus, we should have:

$$I = W \int_0^{H_e} -\sigma_s^{eff} \left(\frac{\partial \varphi_s}{\partial x}\right) dz, \tag{3.13}$$

where W and H_e are the width and height of the electrode, respectively. By combining Eq. (3.12) and Eq. (3.13) the following equation is obtained for the φ_s:

$$W\int_0^{H_e} -\sigma_s^{eff}\frac{\partial\varphi_s}{\partial x}\,dz = \frac{\varphi_s(t)}{R_{ex}+R_{in}(t)}\,. \tag{3.14}$$

This crucial equation can be re-cast in the following form:

$$\boxed{\varphi_s + W\sigma_s^{eff}\left(R_{ex}+R_{in}\right)\int_0^{H_e}\frac{\partial\varphi_s}{\partial x}\,dz = 0.} \tag{3.15}$$

This integro-differential equation will serve as the cathode's boundary condition and it must be satisfied by φ_s at each instant of time t > 0 in the course of our unsteady analysis. In this equation, the internal resistance comprises the ohmic resistance of the electrode, the wiring, and the connectors, which are presumably constant. For the electrolyte, however, it must be taken care of differently because it is not constant. That is to say that, it is increased in the course of time simply because protons are being consumed. In other words, conductivity of the electrolyte (see Eq. 2.33) is reduced during the unsteady mode of operation. Fortunately, we can take care of the conductivity issue directly in our code. In terms of SOC, the time-dependent ionic conductivity of the electrolytes can be obtained from the following relationship [55]:

$$\sigma_f(t) = SOC(t)\left(\frac{F^2}{RT}\sum_i Z_i^2 D_i c_i\right) \tag{3.16}$$

It is worth-mentioning that the ohmic resistance of the electrode and wiring can usually be ignored as compared with that of the electrolyte. Actually, it can certainly be ignored when compared with that of the external load, which is of the order of 10^3 Ω in this work. But, the ohmic resistance of the current collector is usually not negligible and can be as large as 25 Ω for silver-oxide glue as reported in [56]. Still, collector's resistance appears to be negligible when compared with the external load mentioned above. With all these in mind, the internal resistance is estimated to be around 30 Ω for the PowerPAD. And this completes our mathematical development for the unsteady mode

of operation. We can use this methodology for investigating the unsteady behavior of the PowerPAD and predict its runtime and/or power decay with time. We can also investigate how the cell's performance is affected when one of its influential parameters (for example, the pad's thickness) is varied.

3.5.2 Imbibition Equations

In Chapter 2 Richards model has been introduced as the model of choice for designing paper-based systems such as PowerPAD. For this particular cell, however, since the electrodes and pads are made of different types of fibers (cellulose vs. carbon) Richards equation should be solved for each layer. The two solutions are then coupled through appropriate interfacial boundary conditions. Assuming that the flow is two-dimensional and occurring in the xz-plane, for PowerPAD, the *saturation* form of the Richards equation can be expressed as [39]:

$$\frac{\partial S}{\partial t} = \frac{\partial}{\partial x}\left(D(S)\frac{\partial S}{\partial x}\right) + \frac{\partial}{\partial z}\left(D(S)\frac{\partial S}{\partial z}\right), \tag{3.17}$$

where based on the Brooks-Corey correlation [42] we have: $D(S) = D_0 S^n$ where D_0 is the maximum diffusivity corresponding to the fully-saturated case (S = 1). It is worth-mentioning that Richards model has recently been used with great success for designing microfluidic systems [58]. To the best of our knowledge, however, it has not been used in the past for designing any type of paper-based, capillary-driven microfluidic flow cells. But, before we can use this model for the latter purpose, we have to determine the model parameters (n, D_0) both for the electrode and for the absorbent pad. As mentioned in Chapter 2, these two model parameters can be obtained through curve-fitting to the imbibition data obtained experimentally for the porous materials used in the PowerPAD. To that end, it should be noted that three different porous materials are involved in the PowerPAD, as listed below:

- Electrode which is made of Toray TGP–120 non-woven carbon fibers.
- Sample pad which is made of Ahlstrom 238 non-woven cellulosic fibers
- Absorbent pad which is made of Ahlstrom 222 non-woven cellulosic fibers.

Since our theoretical analysis involves only the electrode and the absorbent pad, we do not need the imbibition data for the 238 grade. Based on the wicking data presented in Ahlstrom catalogue, we can easily obtain (D_0, n) for Ahlstrom 222 filter paper using the technique described in [59]. For the Toray paper, however, no wicking data could be found in their catalogue (evidently because, in its original form, Toray paper is not a hydrophilic material), and so we relied on the Brooks-Corey correlations for their estimation; see Appendix A. Table 3.3 shows (D_0, n) parameters needed in the Richards model for both materials. This table also presents some other useful information about these two main components of the system. It needs to be mentioned that the D_0 data in this table are based on the viscosity and density of the quinone electrolytes, which are respectively equal to 5 mPa.s and 1300 kg/m^3 [46]. Also, note that while the contact angle between water and carbon fibers is around 73°, the contact angle between water and cellulose fibers is reported to be around 83° [58]. Since the electrolytes are water-based, we use these values in our simulations.

Table 3.3. Richards model parameters (D_0,n) for the porous materials used in the PowerPAD.

Material	n	D_0 (cm^2/s)	h (μm)	ε (%)	d_p (μm)	d_f (μm)
Toray TGP–120	6.0	1.41 x 10^{-4}	370	78	28	7
Ahlstrom 222	2.6	1.11 x 10^{-5}	830	70	18	16

h = Thickness; ε = Porosity; d_p = Pore diameter; d_f = Fiber diameter

Knowing the model parameters (D_0, n) for the porous materials used in the PowerPAD, we can proceed with solving the Richards equation for the saturation field, S(x,z,t), as a function of time until the system becomes fully-saturated. Having found S(x,z,t) we can use it in the Darcy's law to calculate the velocity field [60]:

$$\mathbf{u} = -\frac{K_{max}\, P_{c,min}}{\mu \varepsilon \lambda}\, S^{(2+1/\lambda)}\, \nabla S, \tag{3.18}$$

where $\lambda = 1/(n-2)$. For fibrous materials we have:

$$K_{max} = \varepsilon d_{max}^2/8 \;\; ; \;\; p_{c,min} = 4\Gamma\cos\theta/d_{max} \tag{3.19}$$

where d_{max} is the maximum pore size of the filter paper (also called *retention* size), Γ is the surface tension, and θ is the contact angle. Having obtained the saturation field, we can use it to find the volume of liquid absorbed by the pad (V) at each instant of time:

$$V(t) = \iiint_V \varepsilon S(x,z,t)\, dV = \varepsilon w \iint_A S(x,z,t)\, dA, \tag{3.20}$$

where "w" is the width of the pad (or electrode) in the y-direction. (In our 2D model, we have w = W.) Knowing $V(t)$ we can calculate the instantaneous flow rate, Q(t), by taking its time-derivative:

$$Q(t) = \frac{dV}{dt} = \iiint_V \varepsilon\left(\frac{dS}{dt}\right) dV = \varepsilon w \iint_A \frac{dS}{dt}\, dA. \tag{3.21}$$

The flow rate obtained this way can be used to find the average velocity from which we can find the Reynolds number. The Reynolds number is needed in the Sherwood number correlation for obtaining the mass-transfer coefficient. It is also needed to ensure that the Darcy's law is indeed applicable in our study—strictly speaking, it is valid for Re < 1—in all our simulations it was found to be less than 0.1.

Solving Richrads equations needs appropriate initial and boundary conditions. Although, the topic of initial and boundary and initial on all pertinent variables (saturation, concentration, electric-potential) will be addressed in Chapter 5, due to their importance, here, we introduce interfacial boundary conditions at the electrode/pad interface. As is well-established in the literature, at the electrode/pad interface, capillary pressure and flux should be continuous [61]. Based on the Brooks-Corey power-law correlations for the capillary pressure presented in Appendix A, continuity of capillary pressure means that at the interface we should have:

$$p_{c,1} = p_{c,2} \;\Rightarrow\; S_2 = \left(\frac{p_{min,1}}{p_{min,2}}\right)^{-\lambda_2} S_1^{(\lambda_2/\lambda_1)}. \tag{3.22}$$

On the other hand, continuity of flux means that at interface we should have:

$$\hat{\mathbf{n}}\cdot\mathbf{q}_1 = \hat{\mathbf{n}}\cdot\mathbf{q}_2 \quad \Rightarrow \quad \hat{\mathbf{n}}\cdot k_1 \nabla p_{c,1} = \hat{\mathbf{n}}\cdot k_2 \nabla p_{c,2} \tag{3.23}$$

where $\hat{\mathbf{n}}$ is the unit normal vector. In terms of S this boundary condition becomes:

$$\left(\frac{1}{\lambda_1}\right) k_{max,1}\ p_{min,1}\ S_1^{(2+1/\lambda_1)} \left(\frac{\partial S_1}{\partial z}\right) = \left(\frac{1}{\lambda_2}\right) k_{max,2}\ p_{min,2}\ S_2^{(2+1/\lambda_2)} \left(\frac{\partial S_2}{\partial z}\right), \tag{3.24}$$

where (λ_1, λ_2) are positive numbers related to power-law index n (see Eq. 2.45). Note that in these relationships, subscript 1 refers to the electrode with subscript 2 referring to the absorbent pad.

3.6. Summary

In this Chapter we have discussed how the mathematical model developed in Chapter 2 can be applied to a novel flow cell called PowerPAD. New ideas have been developed in the present Chapter about how to model this particular cell in unsteady mode of operation. Also, appropriate interfacial boundary conditions have been worked to show the sever nonlinearity of these boundary conditions. In the next Chapter we will describe how the formulations presented in this Chapter can be solved numerically.

Chapter 4:

Numerical Method

4.1. Introduction

The equations governing the electrochemical performance of PowerPAD are too complex to render themselves to an analytical solution thus a numerical method is sought. In this chapter the numerical method adopted for solving these equations is presented. We also validate the numerical scheme using published data.

4.2. COMSOL Multiphysics

A numerical simulation is an attempt to model a real system on a computer so that by changing parameter values predictions can be made about the system behavior [62]. In recent years, computer simulations have become an indispensable tool in applied science for design purposes. With the advent of computers and robust numerical methods, these days it has become quite straightforward to accurately simulate multi-physics problems such as fuel cells and flow batteries [63]. A literature survey reveals that in the past, three different software have been widely used for numerical analysis of electrochemical cells: 1) COMSOL, 2) FLUENT, and 3) OpenFOAM. In this study, we have decided to rely on the COMSOL finite-element software (version 5.5) for our simulations thanks to its highly efficient “PDE module” for solving coupled systems of PDEs [64]. To that end, we had to define all equations pertinent to the PowerPAD by writing appropriate scripts in this software. As mentioned in Chapter 3, designing paper-based flow cells such as PowerPAD involves two diffident steps: 1) imbibition step, and 2) electrochemical step. Although the same PDE solver has been used for both steps, validation had to be done separately for each step. In the next sections, code-verification results are presented for both steps.

4.3. Verifying the Numerical Scheme

The numerical scheme and the script written to solve the equations governing the imbibition equations and the electrochemical equations should be verified before simulating the PowerPAD.

4.3.1. Imbibition Verification

To verify our Richards code for predicting the imbibition phenomenon, we have tried to reproduce numerical results reported in the literature for both homogeneous and non-homogeneous systems. In an interesting experimental and numerical work, Perez-Cruz et al. [43] determined (n, D_0) of Whatman 3MM filter paper by fitting Richards model to the imbibition data for a rectangular geometry. For this filter paper, "n" was reported to be 6 which corresponds to $D_0 = 10^{-5}$ m^2/s. Using these parameters, we have tried to reproduce their numerical data for a sudden expansion geometry made of the same material. Figure 4.1 shows the geometry used by them. It is seen to comprise two rectangular parts of width 6 mm and 18 mm, respectively. The length of the narrow section is 25 mm and the length of the wide section is 30 mm making the total length of the strip equal to 55 mm [43]. We have been able to reproduce their numerical results using roughly 20,000 triangular elements for the same initial and boundary conditions. That is, at t = 0, we have assumed that S = 0 everywhere. The left edge of the strip is then brought into contact with water and is kept at S = 0.84 in the course of the simulation [43]. All other boundaries are assumed to be of no-flux type. Note that in this figure the fluid flows from left to right as soon as its left edge (marked in red) is brought into contact with a liquid such as water.

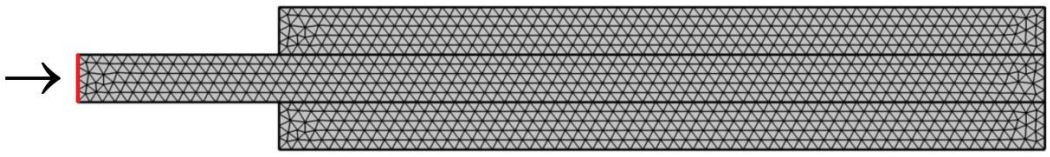

Figure 4.1. Sudden-expansion geometry used for code-verification. For illustrative purposes, a coarse mesh has been depicted in this figure.

Figure 4.2 shows a comparison between our numerical results and the experimental results reported in [43]. As can be seen in this figure, as far as the wetting height is concerned, our numerical scheme is well capable of reproducing the numerical results reported by Perez-Cruz et al. for this particular geometry [43].

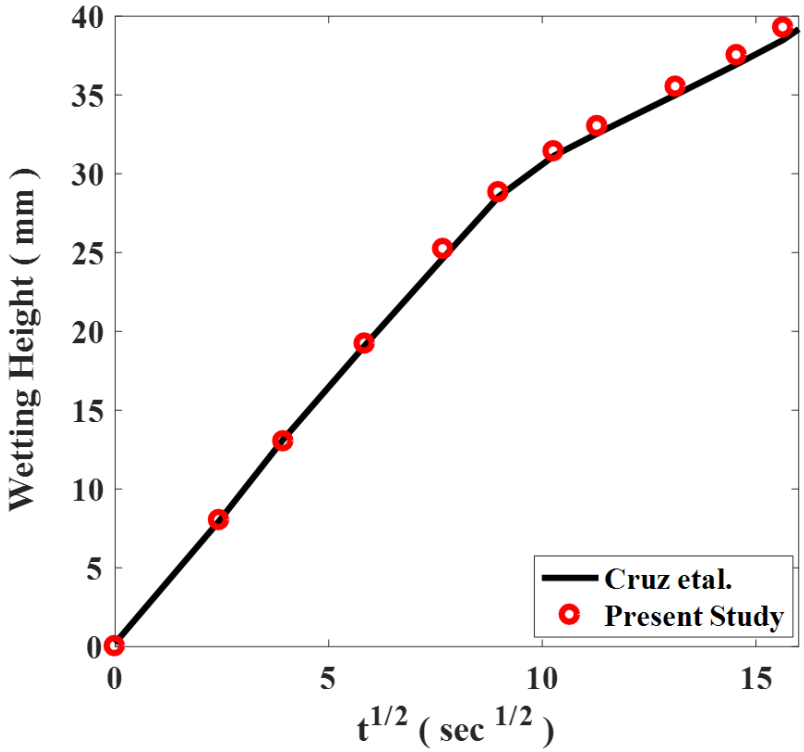

Figure 4.2. Comparison between our imbibition results with published data [43].

To verify our imbibition scheme in its dealing with *non-homogeneous* systems, we have tried to reproduce the results reported by Landeryou et al. [65] for their two-layered parallel-flow system shown in Fig. 4.3. As can be seen in this figure the flow configuration comprises two separate layers stacked on top of each other with the fluid entering the system (which is initially completely dry) from its left plane and propagates to the right in a diffusive manner. Actually, this figure shows a situation in which permeability of the upper layer is larger than that of the lower layer so that the wetted length is larger in the upper layer as compared with the lower layer.

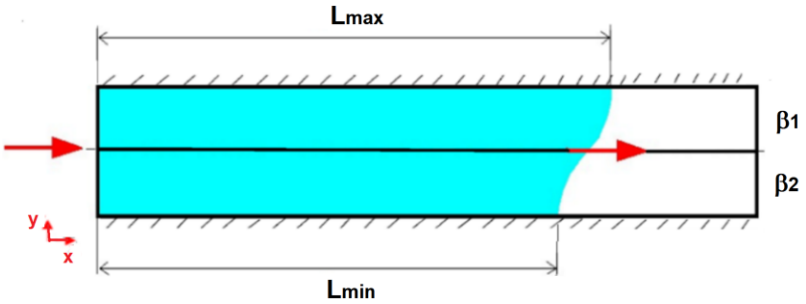

Figure 4.3. Schematic showing the two-layered system used by Landeryou [65] (not to scale).

We have relied on the same formulations and boundary conditions as used in [65] in these simulations. Figure 4.4 shows a typical rectangular mesh used for discretizing the domain. To better resolve the interface, finer mesh have been used in this area.

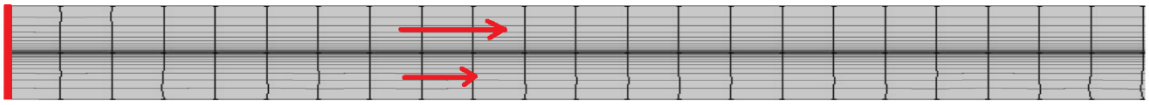

Figure 4.4. A typical rectangular coarse mesh used in the simulation for the two-layered system depicted in Fig. 4.3. Liquid imbibition starts as soon as the right edge (marked in red) is brought into contact with water.

Figure 4.5 shows a comparison between our numerical results with the numerical results reported in [65] for the mass of the liquid imbibed by the system (per square root of time). In plotting this figure, it has been assumed that both layers have the same permeability while their minimum capillary pressure (in other words, their maximum pore size) is different. As can be seen in Fig. 4.5, a good agreement does exist between the two sets of results.

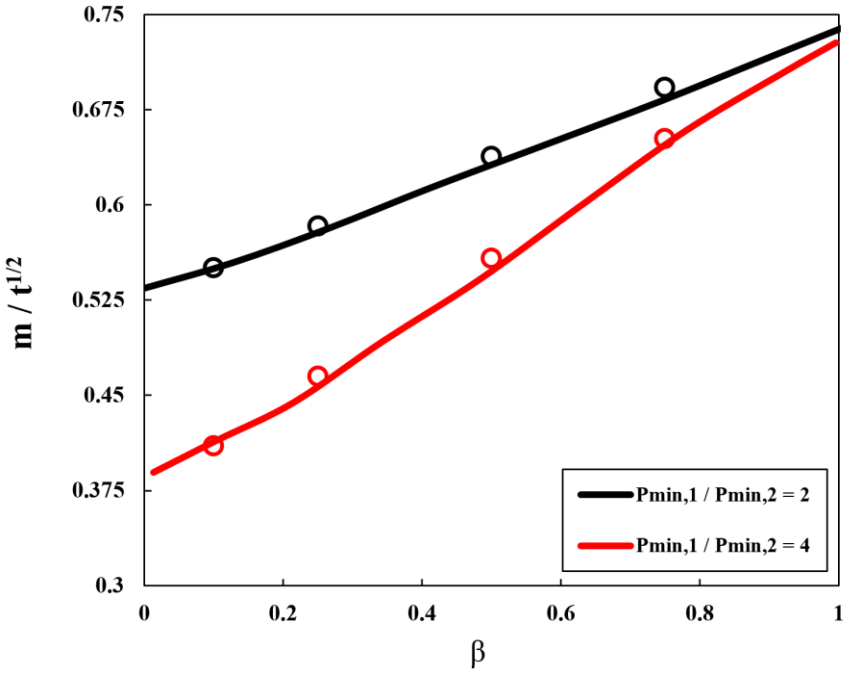

Figure 4.5. A comparison between our prediction for the mass-of-liquid imbibed by the two-layered system (lines) with published data [65] (symbols) $(k_{s,1}/k_{s,2} = 1)$.

The above results clearly demonstrate that the numerical scheme developed in this work for simulating liquid imbibition is working properly.

4.3.2. Electrochemical Verification

As earlier mentioned, our methodology is general and can be used for any redox couples provided their electrochemical properties and kinetics are given. In the PowerPAD, redox couples are of quinone type with the active species being pBQ and H2BQS, which are used in the positive and negative half cells, respectively. To our surprise, there was no numerical data published in the open literature for any "all-quinone" flow battery, and so we have decided to try an all-vanadium flow battery for which a large number of numerical data are available in the literature; see, for example [44]. For an all-vanadium flow cell, the kinetics are as shown below:

Negative Side: $V^{2+} \Leftrightarrow V^{3+} + e^{-}$ (4.1)

Positive Side: $VO_2^{+} + 2H^{+} + e^{-} \Leftrightarrow VO^{2+} + H_2O$ (4.2)

The thermodynamic potential of the negative half-cell is equal to $E^0 = -0.496\,V\ (SCE)$ whereas for the positive half-cell it is equal to $E^0 = +0.750\,V\ (SCE)$. So, the net theoretical standard potential of an all-vanadium cell is equal to 1.26 V. Figure 4.6 shows a skecth of the 2D flow geometry used by Krishnaymurthy et al. [44]. The flow is seen to be occurring in the xy-plane with z-direction serving as the neutral direction. This figure also shows the position of the current collectors. As can be seen in this figure, after exiting the porous electrodes, the two electrolytes meet each other in the central channel where they flow side-by-side in a co-laminar fashion. Note that the channel is closed at y = 12 mm so that the two streams can only flow side-by-side in the negative y-direction with the exit plane located at y = 0. In this figure the inlet velocity (U) is the average velocity which is obtained knowing the inlet area and the flow rate of the syringe pump, Q.

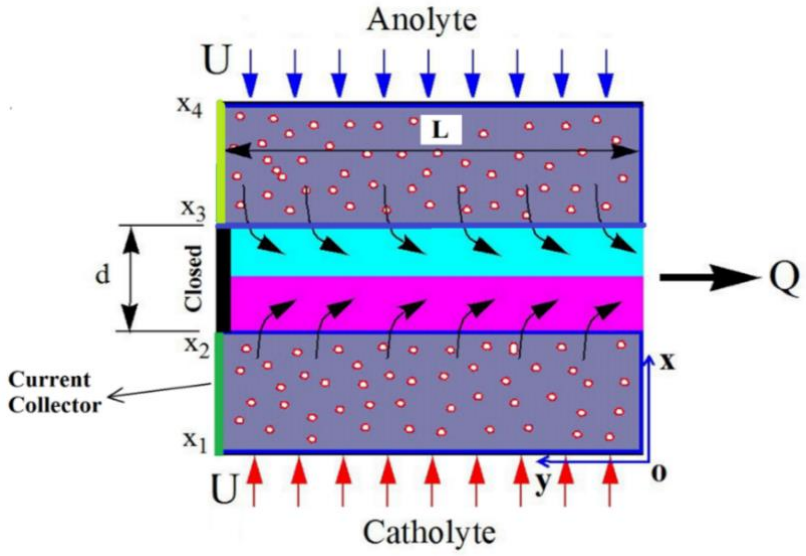

Figure 4.6. Schematic showing the 2D pressure-driven microfluidic cell used in [44].

Using the same parameter values and the same set of equations as used in [44], we managed to obtain steady mesh-independent results in less than 15 min using 13,728 quadrilateral elements with some clustering at the interface. Figure 4.7 shows a

comparison between our 2D numerical results (lines) and the 2D numerical results (symbols) reported in [44]. The comparison is seen to be good confirming that our electrochemical solver is working properly. Note that in obtaining these results, like Krishnamurthy et al. [44], we have ignored the migration term in the Nernst-Planck equation; see Appendix D.

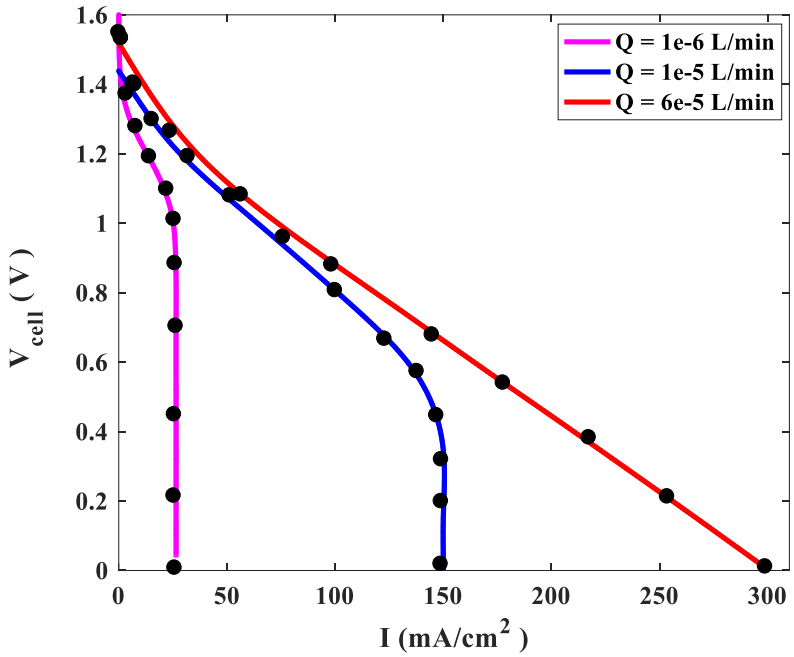

Figure 4.7. Verification with all-vanadium numerical results reported in [44] for polarization curve of a pressure-driven microfluidic flow-through cell.

To verify the code in its dealing with all-quinone cells, we have tried to reproduce the experimental data reported in [45] for a pressure-driven cell similar to that depicted in Fig. 4.6. This all-quinone cell, fortunately, is based on the same type of redox couples used in the PowerPAD, and so it is a good candidate for verification purposes. Figure 4.8 shows a comparison between the numerical results obtained in the present work with the experimental results reported in [45]. The results are seen to be of the same order of the experimental data although there are quantitatively some differences. In Chapter 5, we will see that parasitic reactions due to species crossover can be the main cause of the quantitative difference between the two sets of results.

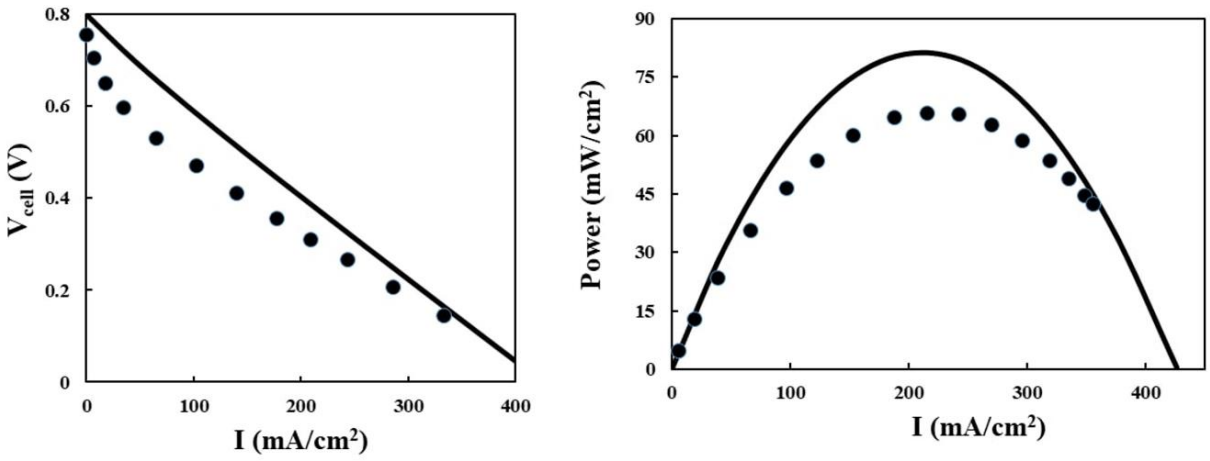

(a) (b)

Figure 4.8. Verification with published all-quinone data reported in [45] for a pressure-driven microfluidic cell. a) polarization curve. b) Power density curve. Solid lines are our numerical results.

4.4. Summary

The numerical results presented in this Chapter have demonstrated that our mathematical/numerical model is well capable of recovering published results for pressure-driven microfluidic flow cells [44,45]. In fact, validation with all-quinone results reported in [45] was of crucial importance to us because their quinone species were the same as those used in PowerPAD. It demonstrated that our mathematical model for quinone is working, It also demonstrated that the electrochemical properties given in Table (3.1) for quinone species are reliable. Still, we should concede that we have not yet validated our quinone code in unsteady mode. Nor have we validated the code in its handling the more delicate problem which involves imbibition model in parallel to the electrochemical model. To that end, a new code was developed which included both models. The new code was a transient code from the beginning. In the next Chapter we will show that the new code can be validated against steady data reported for the PowerPAD in [16] albeit through a pseudo-steady approach. We will also show that the new code can be validated against unsteady results after slightly correcting the unsteady term in the Nernst-Planck equation for the volume difference between 2D and 3D cells.

Chapter 5:

Validation of the Mathematical Model

5.1. Introduction

In this chapter, we use the mathematical model developed in Chapter 3 in order to simulate the operation of the PowerPAD in steady and unsteady modes. The main objective of this Chapter is to validate the mathematical model against steady/unsteady experimental data reported in the literature for the PowerPAD [16]. Of particular importane is the unsteady mode of operation because it can help us figure out the principle(s) underlying the long-term operation of this particular cell. The effect of crossover on the performance of the cell is also investigated in this chapter for the PowerPAD.

5.2. Computational Domain

Figure 5.1 shows the computational domain and a typical quadrilateral mesh used for discretizing the 4h-pad system (our baseline). Note that, for illustrative purposes, a coarse mesh has been shown in this figure. Depending on the thickness of the pad, roughly 15,000 elements (including some clustering at the electrode/pad interface using *boundary* elements) have been used to ensure grid-independency. The time step was dynamically set by COMSOL to achieve the highest efficiency and was monitored to be of order 10^{-4} s depending on the parameter settings. A personal core i7 computer was used for the computations and, thanks to 2D nature of the model, converged results could be obtained in steady mode in less than 20 minutes. For the unsteady mode, the code could deliver converged results even after three hours.

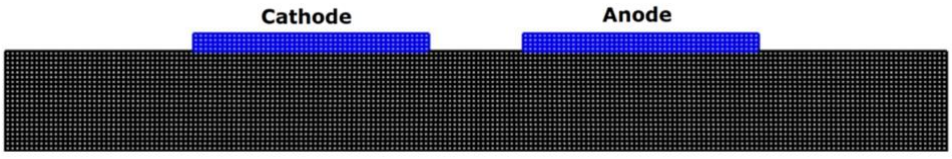

Figure 5.1. A typical mesh used for discretizing the 4h-pad system.

Before proceeding any further, an important issue to address is whether to include migration terms in the analysis or not. In Appendix C we have shown that, as a good approximation, we can drop the migration term from the Nernst-Planck equation. So, in all results to be presented shortly, migration term has played no role on the results. This approxmation will be used for both modes of operation: steady and unsteady.

5.3. Steady Mode of Operation

In the context of fuel cells and flow batteries, the steady mode of operation is often used to obtain the polarization curve of a flow cell. If possible, polarization curves of flow cells should preferably be obtained experimentally using a potentiostat. This is actually the technique used in [16] for obtaining the polarization curves of the PowerPAD [16]. But polarization curves can also be obtained numerically using an appropriate software. Although the numerical scheme (say, code) developed in the present work was originally meant for simulating the unsteady mode of operation for the PowerPAD, the code could also be used for finding the polarization curves of this flow cell through a pseudo-steady (*transient*) approach. The technique is as follows: for a given input voltage (V_{cell}), the unsaturated cell is allowed to imbibe the liquid electrolytes until it becomes fully saturated. At this point in time (i.e., when the flow rate becomes vanishingly small) we record the current generated corresponding to this voltage. This process can provide us with just a single point on the polarization curve. By repeating this process for a large number of input voltages, we can find out other points on the polarization curve. By fitting a curve between these points, we can obtain the polarization curve of the PowerPAD.

Since the code used for these simulations is a transient code, we have to decide on the appropriate initial conditions in addition to the boundary conditions. To that end, we assume that the cell is initially dry (S = 0). We also fix the saturation at the inlet section of the electrode at S = 1 at all times. As to the boundary conditions needed for the saturation field, we impose no-gradient on S at all surfaces other than the inlet section of the electrodes, where we have S = 1 at all times. In Chapter 3 we have shown that at the interface between the electrode and the pad the saturation field in the electrode (S_1)

and that in the pad (S_2) should satisfy certain relationships. For convenience those relationships have been provided below; see Chapter 3 for more details:

$$S_2 = \left(p_{min,1}/p_{min,2}\right)^{-\lambda_2} \; S_1^{(\lambda_2/\lambda_1)}. \tag{5.1}$$

$$\left(\frac{1}{\lambda_1}\right) k_{max,1} \; p_{min,1} \; S_1^{(2+1/\lambda_1)} \left(\frac{\partial S_1}{\partial z}\right) = \left(\frac{1}{\lambda_2}\right) k_{max,2} \; p_{min,2} \; S_2^{(2+1/\lambda_2)} \left(\frac{\partial S_2}{\partial z}\right), \tag{5.2}$$

where k_{max} and p_{min} can be obtained through Brooks-Corey correlations [42]; see Appendix A. To close the problem, we also have to decide on the boundary conditions needed for the concentration and electric-potential fields. First of all, we assume that the electrolytes enter the electrode with an SOC = 95% so that the concentrations of active species (H_2BQS and pBQ) are always equal to 0.19 M at the inlet section. This also means that the concentration of the products (BQS and H_2BQ) are, respectively, equal to 0.01 M at the inlet section of the electrodes. On *all* other planes, we impose no-gradient condition in our code for the concentration of all other species. As to the boundary conditions needed for the electric potential, the cathode voltage is given as an input with the anode potential set equal to zero. Insulation boundary condition (i.e., no-gradient) is used for the electronic potential on *all* other planes. The net current is collected through the outer side plane of the cathode; see Fig. 3.4. With these initial and boundary conditions, we can proceed with our pseudo-steady analysis.

Figure 5.2 shows a comparison between our *pseudo-steady* numerical results (lines) with the *steady* experimental data (symbols) reported in [16] for three different pad thicknesses (h, 2h, and 4h). This figure shows that, as far as polarization curves are concerned, the numerical scheme developed in the present work is doing a decent job in recovering PowerPAD's polarization curves.

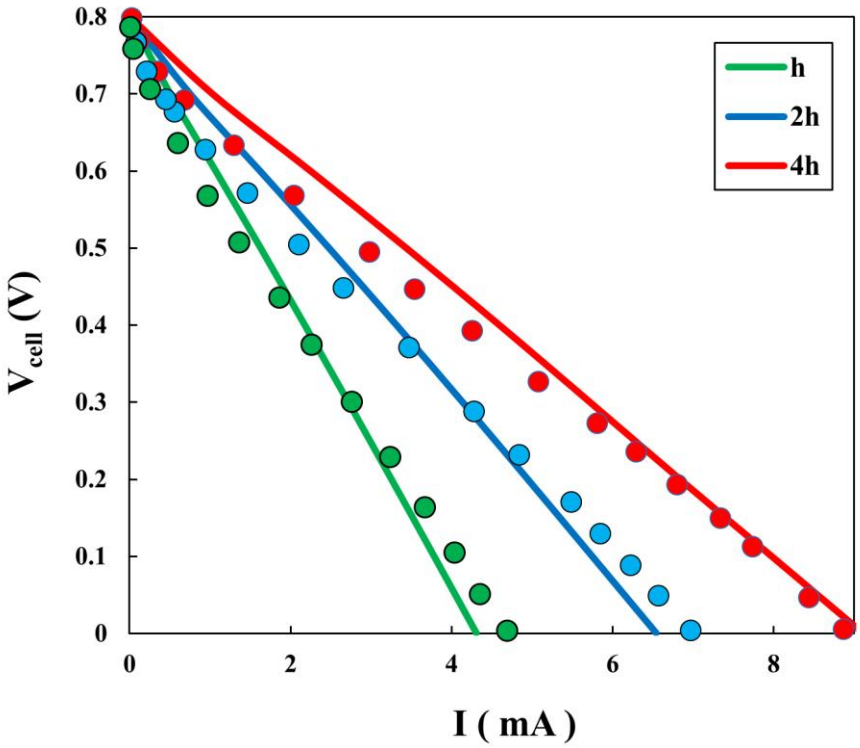

Figure 5.2. Verification with PowerPAD experimental data reported in [16].
An open access article reproduced with permission from Wiley and Sons.

It is worth-mentioning that, PowerPAD can generate electricity even during the transient mode. That is to say that, provided the cell is connected to a load, as soon as the two electrolytes meet each other on the mid-plane, the cell can generate electricity and energize the load. This particular "time" (called activation time) was not reported in [16], perhaps because it was deemed unnecessary. We can easily compute the activation time through our *transient* code. Figure 5.3 shows typical transient results obtained for the 4h-pad system. This figure shows that, the activation time of this particular cell with this particular pad is equal to t = 0.33 s. Our numerical results show that, due to saturation discontinuity at the interface between the electrode and the absorbent pad, when equilibrium is reached, for the electrode we have S = 1 while for the absorbent pad we have S_{eq} = 0.93. In other words, for a two-layered system such as PowerPAD, a fully-saturated pad actually means a uniformly-saturated pad. The time needed for equilibrium to prevail (i.e., for the system to become, say, fully-saturated/fully-uniform) is roughly equal to 12.5 seconds for this set of parameters; see Fig. 5.4.

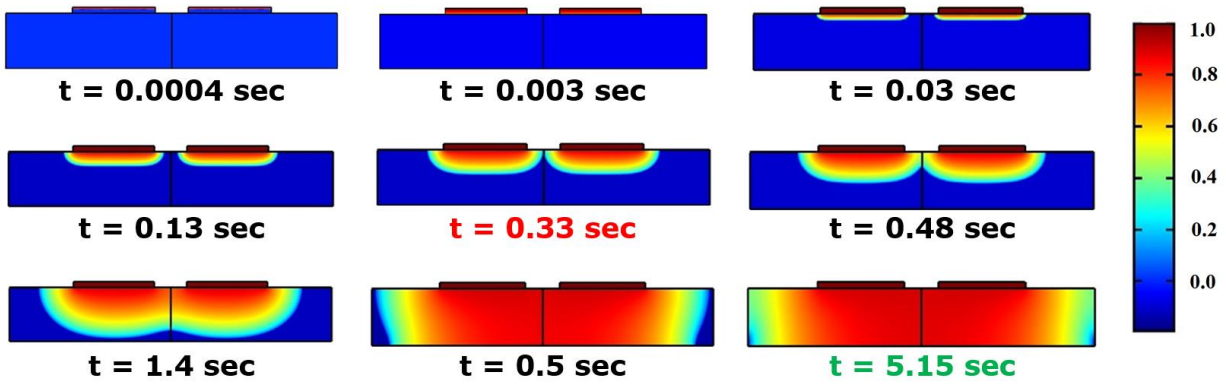

Figure 5.3. Time evolution of the saturation field for the PowerPAD (4h-pad system).

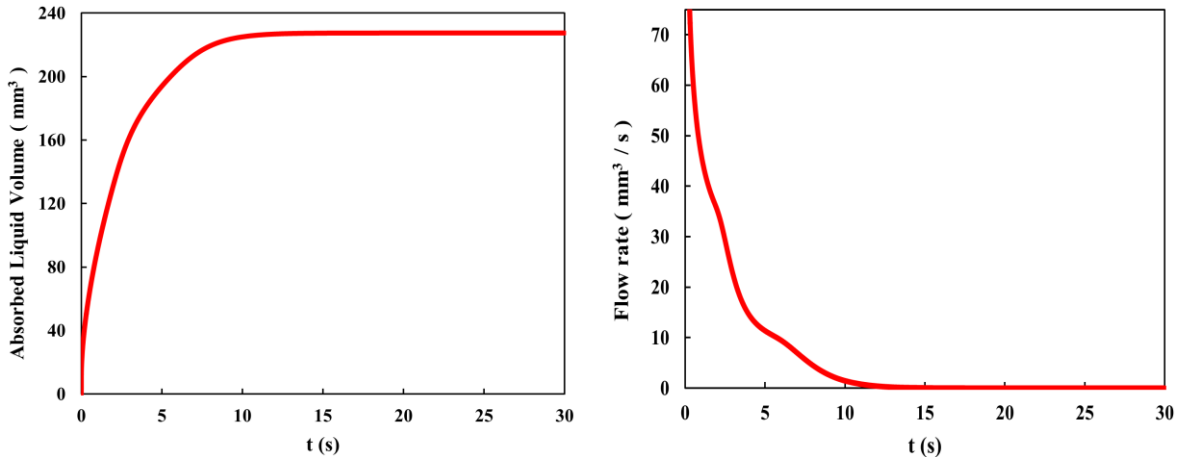

(a) (b)

Figure 5.4. Time variation of: (a) absorbed liquid volume, and (b) flow rate.

5.4. Unsteady Mode of Operation

Unsteady mode of operation refers to the situation in which a fully-saturated cell (i.e., a cell fully loaded with the fuel and oxidant) is connected to an external load. PowerPAD can then energize the load in the same way that a dry cell would energize this load. Figure 5.5 shows schematically what happens when a 2000-Ohm load is connected to the PowerPAD. As discussed in Chapter 3, the intersection point between the load and the polarization curve serves as the *operating point* of the cell. Table 5.1 shows the coordinates of the intersection points for all three pad systems in the VI-plane. We need

the coordinates of these points in the VI-plane as initial conditions in our unsteady analysis, as described in more details below.

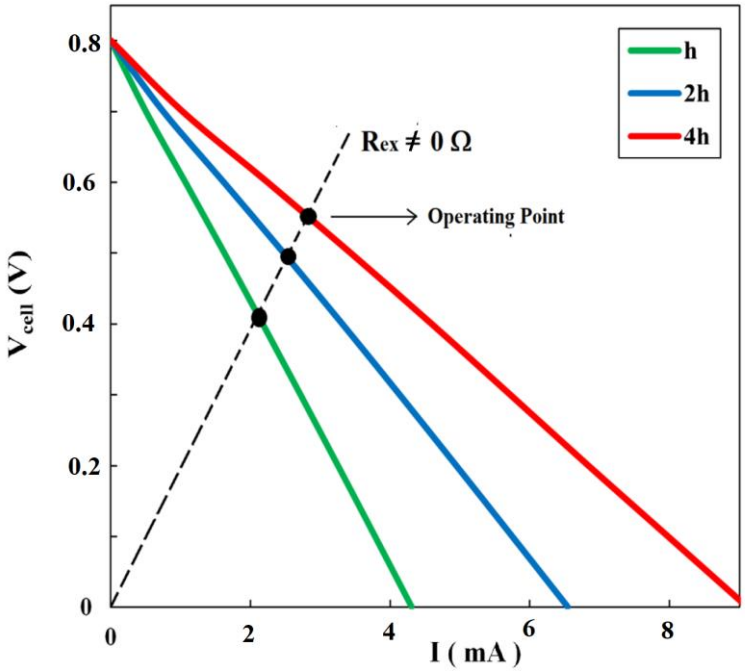

Figure 5.5. Schematic showing the operating points for different pad thicknesses at a typical external load.

Table 5.1. Characteristics of the operating points.

PAD Label	Voltage (V)	Current (mA)	Power (mW)
h	0.728	0.365	0.266
2h	0.750	0.377	0.282
4h	0.763	0.380	0.290

During the unsteady mode of operation, the unsteady form of the Nernst-Planck equation must be satisfied by the concentration field, c (x.z.t), inside the fully-saturated electrodes. This equation reads as:

$$\varepsilon\left(\frac{\partial c_i}{\partial t}\right) - D_i^{eff}\left(\nabla^2 c_i\right) = -R_i \quad ; \quad i = 1,2,\ldots,5 \tag{5.3}$$

where we have ignored the migration term. A similar equation can be written for the absorbent pad with no source/sink term—for the pad the unsteady term must be

multiplied by $S_{2,\,eq.}$ This equation needs appropriate initial and boundary conditions to be amenable to a numerical solution. To that end, as soon as the pad becomes fully saturated, we reset the time to t = 0. At this initial time, we set saturation inside the pad equal to S_{eq} (taken from our steady analysis) while we already know that for the electrode it is equal to S = 1. These are our initial conditions for the saturation field. As to the initial concentration field, we assume that it is uniform at t = 0 even though during pseudo-steady analysis the concentration field becomes slightly non-uniform. (Presumably, a potential consumer will buy a fully-saturated/fully-charged cell with uniform concentration not a cell used by the developer for measuring its polarization curve.) As concentration boundary condition, we impose no-gradient on all planes including the inlet section because there is no further supply of the reactants in this mode of operation. As to the initial conditions for the electric potential, we use the data in Table 1. For the boundary condition, at all times, we impose Eq. (3.15), given below for convenience:

$$\varphi_s + W R_{tot} \sigma_s^{eff} \int_0^{H_e} \frac{\partial \varphi_s}{\partial x} \, dz = 0. \tag{5.4}$$

where R_{tot} is the total ohmic load. But, before proceeding with the simulation we should note that the volume of the absorbent pad in our 2D model is roughly 1/4 of that in 3D cell. As previously mentioned, (see Eq. 3.9) the volume of the electrolyte is of key importance in our analysis because it closely controls the unsteady behavior of the cell through Eq. 3.8. In other words, the rate at which the concentration of active species drops with time is not the same between 2D model and the 3D systems unless we modify the unsteady term in Eq. 5.3. (This term has actually entered this equation through a control-volume analysis, which is why volume of the electrolyte affects it.) Figures 5.6 and 5.7 show the numerical results obtained using the above-mentioned correction factor for the unsteady term in the Nernst-Planck equation. These figures show a comparison between our numerical results obtained using this volume-corrected 2D model (lines) with the experimental data reported for the original 3D device in [16] (symbols).

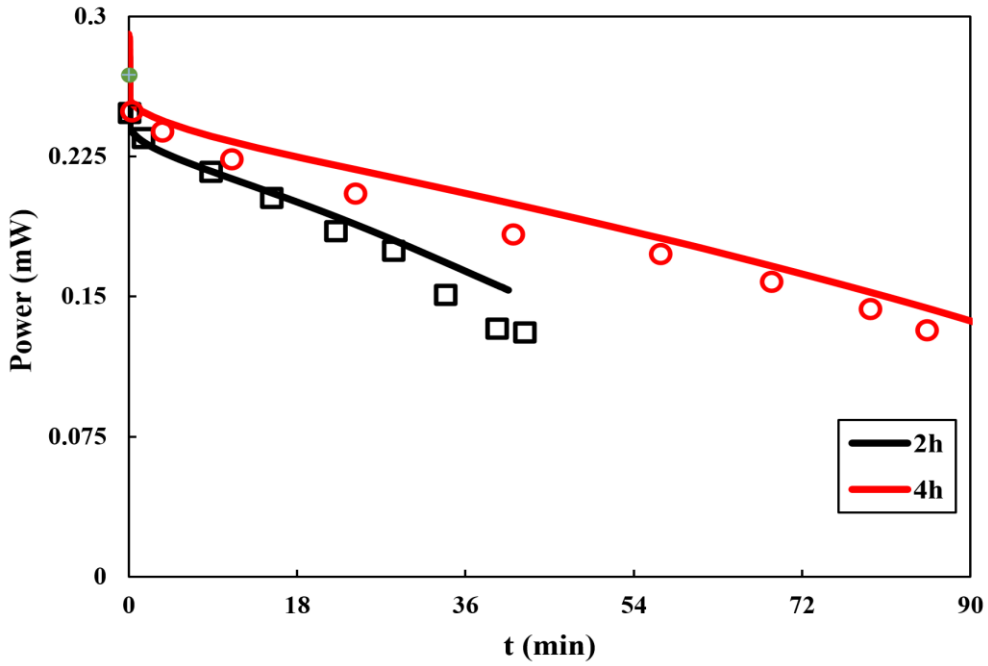

Figure 5.6. Verification with PowerPAD's unsteady results (2000 Ω load). Symbols are experimental data.

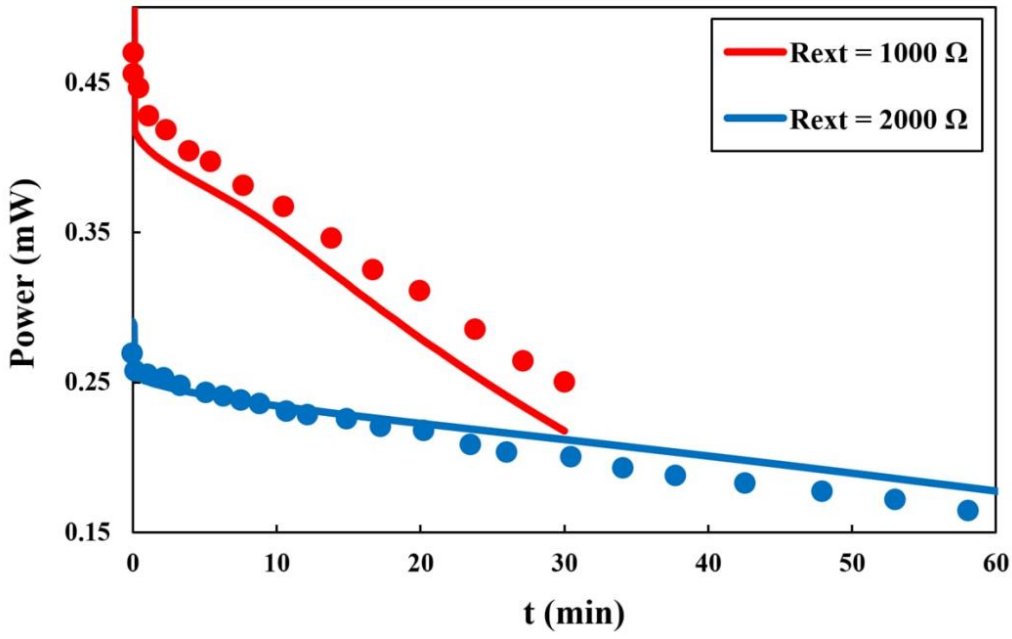

Figure 5.7. Verification with PowerPAD's unsteady results (4h-pad system). Symbols are experimental data.

The numerical results reported in Fig. 5.6 are qualitatively in line with the experimental observation that, for any given load, the power output and also the operation time of the

PowerPAD are enhanced when thicker pads are used as its absorbent material [16]. This is not surprising realizing the fact that a thicker pad stores a larger amount of electroactive species, and so it should deliver a larger capacity. Our numerical results also confirm the experimental finding that PowerPAD should generate a higher power when operated at a lower load albeit for a shorter service time; see Fig. 5.7. This behavior is also not surprising realizing the fact that a smaller load means that a higher current can be drawn from the cell because the operating point of the cell shifts to a lower cell voltage. As a result, active species are consumed at a higher rate making its runtime shorter. What is obvious is that there is a strong coupling between power output and the runtime of the cell, as is the case for ordinary dry cells. Based on the results presented in Fig. 5.7 one might reach to the wrong conclusion that a smaller load always corresponds to a larger power. Figure 5.7 shows that this is not necessarily true. In this figure we have plotted the power output as a function of external load (the so-called PPC curve) using the technique described in Chapter 2 and the polarization data presented in Fig. 5.2. As can be seen in this figure, the power of the cell peaks at a certain (small) load. In other words, power output is not a monotonic function of the external load.

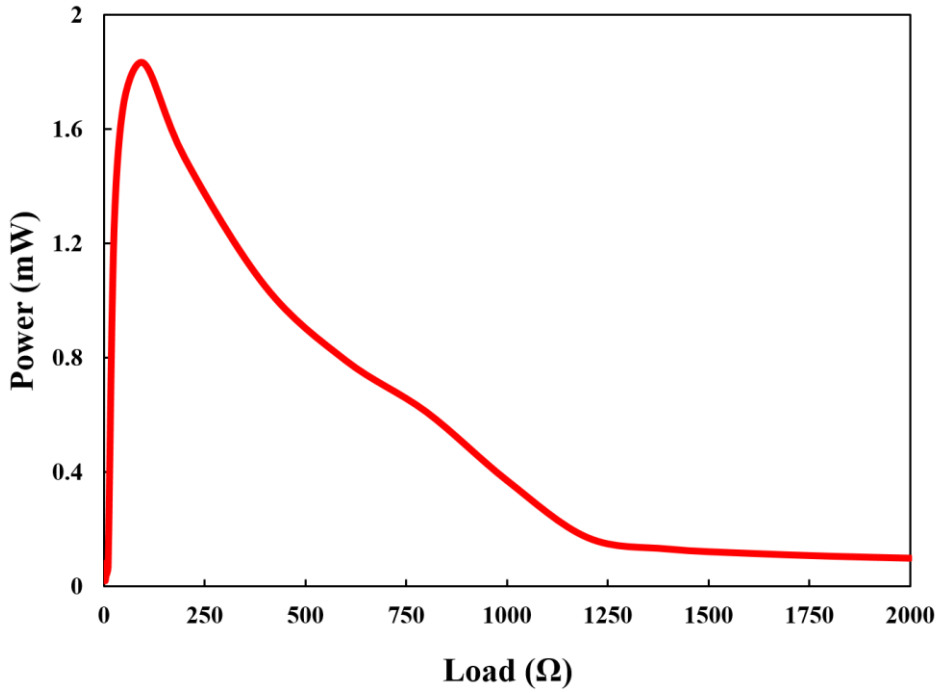

Figure 5.8. Variation of output power with external load (4h-pad system).

Based on this figure, the point of maximum power (which is roughly equal to 1.85 mW) is obtained with an external resistance of 88 Ω, and it corresponds to (V, I) = (0.4 V, 4.5 mA). For curiosity, we have tried to calculate the three main sources of polarizations at the point of maximum power in Fig. 5.8: i) ohmic loss, ii) activation loss, and iii) mass-transport loss. In principle, COMSOL can deliver activation overpotential. However, because our code is a transient code, it underestimates this overpotential (simply because species are consumed in the course of our pseudo-steady computations when we were trying to obtain the polarization curve). As such, we have decided to calculate the activation potential directly using the Butler-Volmer equation. We can also use simple analytical formulations for estimating the mass-transport loss. As the first step, we should note that the cell's total loss is nearly equal to 0.4 V at the peak point. We can proceed with calculating the voltage drop due to the mass-transport limitation and that due to the activation limitation using known formulae [22]. Having obtained these two overpotentials, the ohmic loss can be estimated knowing the total voltage drop, as described below.

Mass Transport Loss:

For the mass-transport overpotential we can use the following formula [22]:

$$\Delta V_M \approx \frac{RT}{nF}\left(1+\frac{1}{\alpha}\right)\ln\left(\frac{i_L}{i_L - i}\right) \tag{5.5}$$

where i_L is the limiting current. For the baseline 4h-pad system, the limiting current is equal to 9 mA. For an average charge-transfer of α = 0.275 (see Table 3.3), this formula gives roughly **0.05 V** as the mass-transport loss.

Activation Loss:

In [22], the following equation has been worked out for estimating the activation overpotential:

$$\Delta V_A \approx \frac{RT}{\alpha nF} \ln\left(\frac{i}{i_0}\right), \tag{5.6}$$

where i_0 is the reaction exchange current density. Unfortunately, exchange current density has not been reported in the literature for our quinone species on bare carbon-fiber electrodes, but we can easily calculate it using the Butler-Volmer formulations [22]:

$$i_{0,1}(\text{cathode}) = F k_1 \left(c_{IV}\right)_0^{\alpha_{1,c}} \left(c_V\right)_0^{\alpha_{1,a}} = 0.74\ (\text{mA.cm}^{-2}) \tag{5.7}$$

$$i_{0,2}(\text{anode}) = F k_2 \left(c_{II}\right)_0^{\alpha_{2,c}} \left(c_{III}\right)_0^{\alpha_{2,a}} = 4.32\ (\text{mA.cm}^{-2}) \tag{5.8}$$

where we have used the data in Tables 3.1 and 3.2 for the computations. Note that at the peak power output, for the 4h-pad system, the cell's current density is 4.5 mA which amounts to a current density of 18 mA.cm^{-2}. Using these values, the activation overpotential is estimated to be around **0.09 V**.

Ohmic Loss:

With the mass-transport loss being equal to 0.05 V and the activation loss being equal to 0.09 V we conclude that the ohmic loss is nearly equal to **0.26 V**. So, roughly 70% of the total voltage drop is due to the ohmic loss, 20% is due to the activation loss, and 10% is due to the mass-transport loss. These results also imply that the point of maximum power lies somewhere in the ohmic-loss region of the polarization curve shown in Fig. 5.2. With the ohmic loss being responsible for almost three-quarter of the total loss, one can claim that the ohmic loss is playing the role of the "limiting factor" for this particular cell.

5.4.1 Efficiency of PowerPAD

Another look at Figs. 5.6 and 5.7 reveals that although the comparisons between our numerical results and the experimental data reported in [16] are good they are not perfect. We can show that the comparisons become better if we include crossover in our analysis. But before modelling crossover for the PowerPAD, in this sub-section, we

present two different measures for the PowerPAD's efficiency and use them to assess the efficiency of the baseline cell as a function of time. In the next sub-section we model crossover for the PowerPAD. A flow cell's electrochemical performance is generally evaluated using four different efficiency metrics: 1) voltage efficiency (η_V), columbic efficiency (η_C), power efficiency (η_P), and energy efficiency (η_E). They are defined based on the discharge/charge behavior of the cell as shown below [22]:

$$\eta_V = \frac{\text{Discharge Voltage}}{\text{Charge Voltage}} \times 100\% \tag{5.6}$$

$$\eta_C = \frac{\text{Discharge Capacity}}{\text{Charge Capacity}} \times 100\% \tag{5.7}$$

$$\eta_P = \frac{\text{Discharge Power}}{\text{Charge Power}} \times 100\% \tag{5.8}$$

$$\eta_E = \frac{\text{Discharge Energy}}{\text{Charge Energy}} \times 100\% \tag{5.9}$$

These efficiencies are controlled by the current density, ionic conductivity of the electrolytes, electrode material, cell architecture, SOC, and its kinetics [66]. Since PowerPAD is not a cell intended to work in the charging mode, we need another measure(s) for its efficiency. The two metrics proposed in [57] for another paper-based capillary-driven microfluidic flow cell appear to be more appropriate for the PowerPAD. They are defined as shown below [57]:

$$\eta_F = \frac{\int_0^t I(\tau)\,d\tau}{q_{th}}, \tag{5.10}$$

$$\eta_E = \frac{\int_0^t I(\tau)E(t)\,d\tau}{E_0 q_{th}}, \tag{5.11}$$

where η_F is the faradaic efficiency, and η_E is the energy efficiency. In these relationships, I(t) and E(t) are the cell's time-dependent current and potential at the operating point with E_0 being its theoretical Nernst potential. It is worth mentioning that the faradaic efficiency is a measure of the electroactive species stored in the cell. In other words, it represents the theoretical charge capacity stored in the cell which is actually being converted into current. One the other hand, the energy efficiency can be interpreted as the ratio of the power generated by the device to the energy that the cell could ideally deliver when working at its theoretical voltage [67]. Using these relationships, we can compute PowerPAD's efficiency with time. Figure 5.9 shows these two efficiencies computed for the PowerPAD. For convenience, we have used two different formats for presenting the results. While in plot (a) in this figure these efficiencies have been shown as functions of time, in plot (b), like [57], we have shown these two efficiencies in terms of each other. Note that for the latter plot, we just have to extract these two efficiencies at a given time from plot (a) which gives us a single point on plot (b). For example, at time t = 80 min, the two efficiencies are roughly equal to 38% and 32% based on the data in plot (a). These two points are combined into a single point on plot (b) shown by the blue symbol in this plot. The efficiencies predicted for the PowerPAD are of the same order as the experimental values reported for another paper-based capillary-driven flow cell [57].

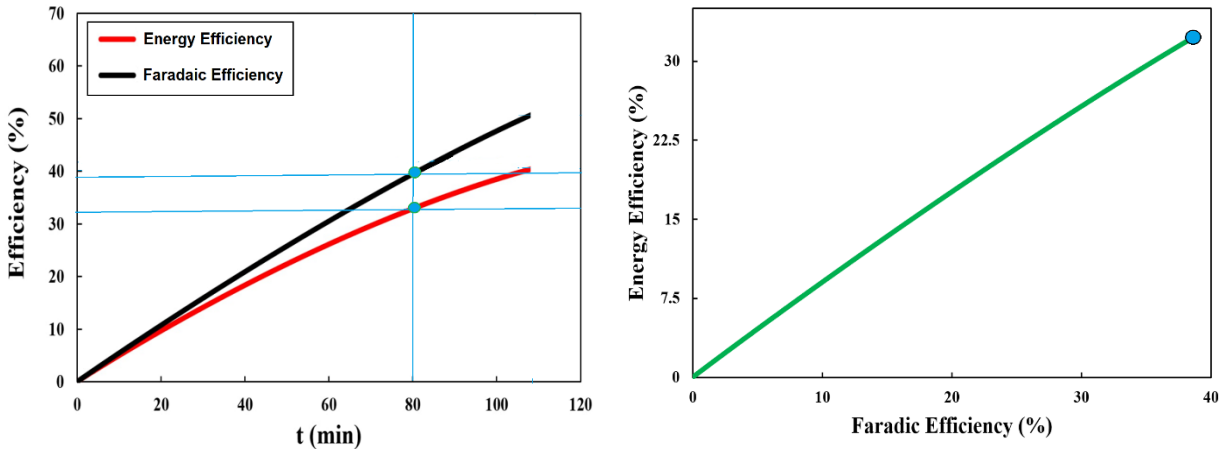

(a) (b)

Figure 5.9. Efficiency variation with time: (a) faradaic efficiency; (b) energy efficiency (4h-2000 system).

5.5. Crossover Modelling

Flow cells that are not equipped with membrane are, in general, vulnerable to species crossover, and PowerPAD is no exception [68]. Figure 5.10 shows fuel concentration at three different points in time during the cell's unsteady mode of operation. As can be seen in this figure, as soon as the cell starts energizing a load, some fuel in the negative half-cell (situated on the right-hand-side of the cell) have crossed over to the positive half-cell, which is situated on the left-hand-side of the cell. Given enough time, some of this fuel reaches the cathode and undergoes parasitic electrochemical reaction in this electrode thereby generating unwanted electrons. Figure 5.11 shows the concentration of the fuel inside the cathode. As is evident in this figure, the fuel has indeed diffused inside the cathode. The region most vulnerable to crossover is seen to be the lower right-corner of the cathode; see Fig. 5.11.

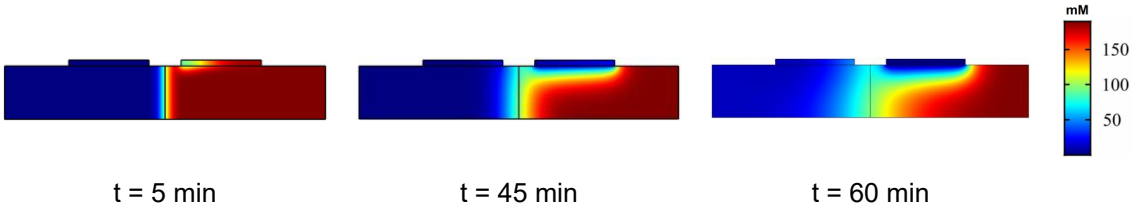

Figure 5.10. Contour plots for the fuel concentration at two different times (R_{ex} = 2000 Ω).

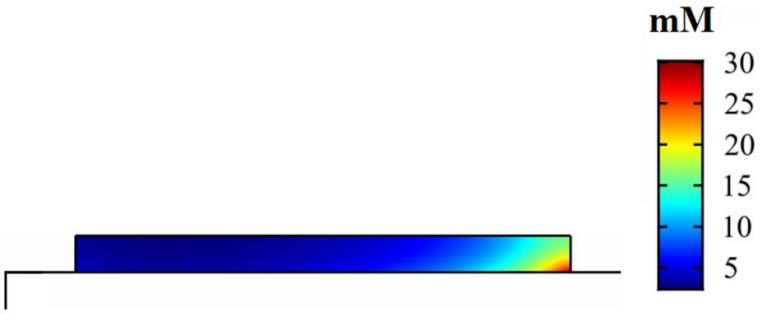

Figure 5.11. Amount of fuel crossed over to the cathode after t = 100 min (4h-2000 system).

From the above figures, one can conclude that PowerPAD is quite vulnerable to crossover (albeit at very long times), and so it requires a full crossover analysis. It is to be noted that fuel that has crossed over to the opposite half-cell, by default, means a loss of capacity even if it does not get involved in any kind of parasitic side reactions. But, the crossed-over species may indeed undergo parasitic side reactions, and there are two different types of such reactions which might occur in microfluidic flow cells:

1) Homogeneous side-reactions, which occur in the bulk fluid.
2) Heterogeneous side-reactions, which occur inside the electrode.

Both types of side-reactions mean a loss of capacity [68]. In fact, under extreme conditions they can even give rise to self-discharge, which exhibits itself by a sudden drop in performance. While homogeneous reactions are *chemical* in nature and occur in the bulk liquid (starting from the interface), heterogeneous reactions are *electrochemical* in nature and occur only on the surface of the wrong electrodes. Unlike chemical side-reactions which are spontaneous, electrochemical side-reactions usually occur at a

lower rate. An analysis of homogeneous crossover requires a good knowledge about the chemical side reactions. Such side-reactions are well established for all-vanadium cells [69]. For all-quinone cells, however, such chemical side-reactions have not yet been documented in the open literature. As such, the present analysis will be devoted to the heterogeneous crossover only.

As mentioned above, heterogeneous crossover refers to the active species electrochemically reacting on the surface of the opposite electrode. This happens when, for example, the fuel (H_2BQS) crosses over from the negative side and reaches the cathode on the positive side. And when it reaches the cathode (see Fig. 5.11) it generates *unwanted* electrons in the same way that the same fuel would generate *useful* electrons on the surface of anode. The oxidant (pBQ) in the positive half-cell then consumes these *unwanted* electrons instead of the regular ones coming from the anode (say, through the external wiring). This phenomenon can severely reduce the power output of a microfluidic flow cell [69-71]. As mentioned above, under extreme conditions, it can even give rise to self-discharge which exhibits itself as a complete loss of power output from the cell.

To investigate the effect of parasitic electrochemical reactions for the PowerPAD, we have to deal with two electrochemical reactions on each electrode with one of them being the *main* reaction and the other one the *parasitic* reaction. For instance, on the surface of the cathode we have the main electrochemical reaction, which is the reduction of pBQ, and the parasitic electrochemical reaction, which is the oxidation of H_2BQS. A similar argument can be applied to the anode where the *main* reaction is the oxidation of H_2BQS with the *parasitic* reaction being the reduction of pBQ. On both electrodes the parasitic reactions lower the net current generated by that electrode. In practice, this leads to a drop in the net current generated by the cell, for any given cell voltage. Noting the fact that heterogeneous crossover is concerned with active species only (i.e., H_2BQS and pBQ), we assume that parasitic side-reactions occur at the overpotential of the electrode onto which they have crossed over [69]. So, for the parasitic electrochemical reactions (denoted by subscript “P”) we have:

$$\text{Cathode}: j_{1,P} = F k_2 \left(C_{IV}\right)^{\alpha} \left(C_V\right)^{\alpha} \left[\frac{C_{II}^s}{C_{II}} \exp\left(+\frac{\alpha n F}{RT}\eta_2\right) - \frac{C_{III}^s}{C_{III}} \exp\left(-\frac{\alpha n F}{RT}\eta_2\right)\right] \tag{5.14}$$

$$\text{Anode}: j_{2,P} = F k_1 \left(C_{II}\right)^{\alpha} \left(C_{III}\right)^{\alpha} \left[\frac{C_V^s}{C_V} \exp\left(-\frac{\alpha n F}{RT}\eta_1\right) - \frac{C_{IV}^s}{C_{IV}} \exp\left(+\frac{\alpha n F}{RT}\eta_1\right)\right] \tag{5.15}$$

It needs to be mentioned that in coming up with these equations, we have assumed that when an active ion crosses to the opposite half-cell, its kinetic parameters remain intact [68]. Knowing the parasitic current density, we can find the net current density (j) for any given cell voltage, as shown below [67]:

$$j_{net} = \left(j_{2,M} - j_{2,P}\right) - \left(j_{1,M} - j_{1,P}\right) = \underbrace{\left(j_{2,M} - j_{1,M}\right)}_{\text{main current}} - \underbrace{\left(j_{2,P} - j_{1,P}\right)}_{\text{parasite current}} \tag{5.16}$$

where subscript M refers to the main reactions; see Eqs. 3.2a,b. For the active species involved in the parasitic reactions, we have:

$$\frac{dc_2}{dt} = D_2 \nabla^2 (c_2) - \frac{j_{2,M}}{F} - \frac{j_{2,P}}{F} \tag{5.17}$$

$$\frac{dc_5}{dt} = D_5 \nabla^2 (c_5) - \frac{j_{1,M}}{F} - \frac{j_{1,P}}{F} \tag{5.18}$$

For the remaining species, we have:

$$\frac{dc_3}{dt} = D_3 \nabla^2 (c_3) + \frac{j_{2,M}}{F} \tag{5.19}$$

$$\frac{dc_4}{dt} = D_4 \nabla^2 (c_4) + \frac{j_{1,M}}{F} \tag{5.20}$$

Using these formulations, we can proceed with investigating the effect of parasitic side-reactions on the PowerPAD. Figure 5.12 shows the effect of crossover on the power output of this cell. For comparison purposes, this figure also includes numerical results for the cell when crossover is neglected. As can be seen in this figure, with crossover included in the analysis, the critical time becomes much shorter. To be more specific, the critical time is reduced from t = 110 min to roughly t = 85 min. These results clearly demonstrate that fuel crossover to the cathode and generation of unwanted electrons in

this electrode (as caused by the parasitic side-reactions) has a detrimental effect on the cell's electrochemical performance. But, what is more important is the notion that with crossover included in our analysis the numerical results become much closer to the experimental data reported in [16]; see Fig. 5.12. The conclusion is that, crossover plays a key role on the long-time performance of the PowerPAD. In fact, it can be considered as the **"limiting factor"** for this particular cell; at least, under its current working conditions (i.e., where the external load is of the order of 10^3 ohms).

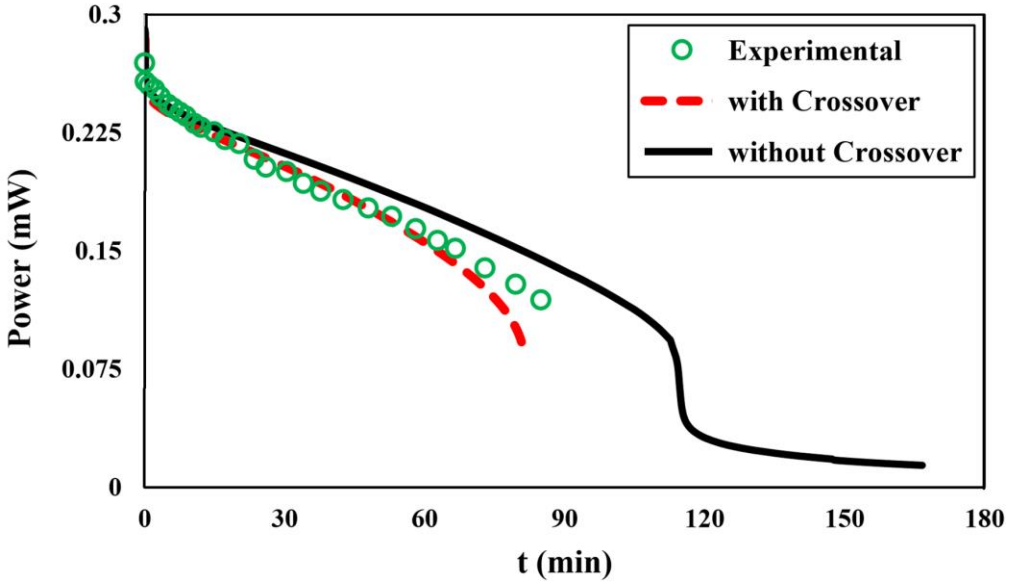

Figure 5.12: Effect of parasitic reactions on the power output of PowerPAD (4h-2000-system).

5.6. Concept of Back Diffusion

As earlier mentioned, in [16], PowerPAD was connected to an external load after it is fully-saturated with the reactants. The cell then works in its unsteady mode during which it generates a time-decaying power for roughly an hour depending on the thickness of its pad and the size of the load. The question then arises as to how the cell can continue generating power for such a long time? It is indeed puzzling why the cell should even work under fully-saturated condition while there is no supply of fresh electrolytes. First of all, this phenomenon is a clear manifestation of the fact that the diffusion-limited mass-transfer coefficient (m) is indeed non-zero even when there is no bulk flow. So, when designing such cells use should always be made of Sherwood-

number correlations that incorporates the diffusion-limited term in the Sherwood number; see Eq. 2.23b.

Another fact is that as soon as the cell is connected to an external load, the reactants residing inside the electrodes start being consumed. If there were no reactants inside the absorbent pad, the electrodes would be depleted of their active species within a couple of seconds which would exhibit itself by the power dropping to zero very fast. So, if the cell continues generating power it is because there is a supply of reactants to the electrodes from the pad. This phenomenon, which is called “back-diffusion” in this work, appears to be the main reason why the cell works for such a long time; see, also, Appendix D. That is to say that, with the concentration of, say, fuel becoming low inside the anode, a gradient then develops between its value in the pad and its value in the anode. According to Fick’s equation, this causes the fuel to diffuse back from the pad to the anode. However, as time progresses, the concentration gradient becomes weaker and weaker so that the power output of the cell should decrease with time, and this is exactly what we see in Fig. 5.13. Figure 5.14 shows that this is also true for the current and voltage.

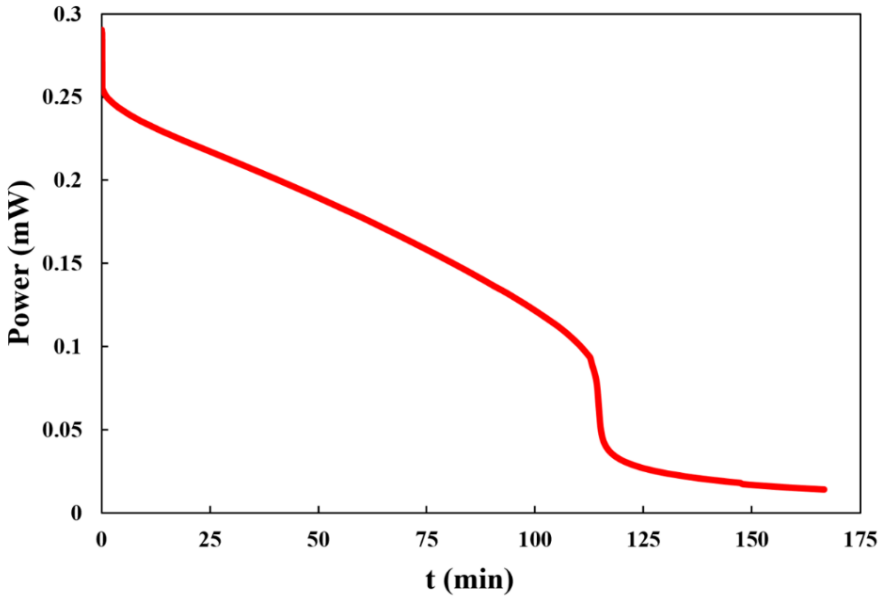

Figure 5.13. Decay of power output with time for the 4h-pad system with no parasitic crossover included in the analysis (R_{ex} = 2000 Ω).

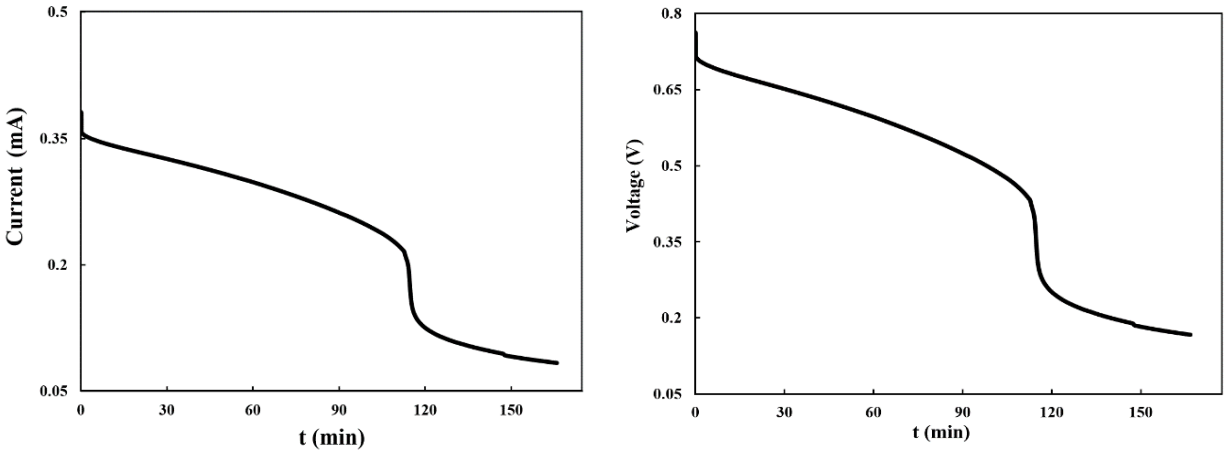

(a) (b)

Figure 5.14. Time-variation of: a) current, and b) voltage for the 4h-pad system (R_{ex} = 2000 Ω).

Another look at Figs. 5.13 and 5.14 shows that there is a sudden drop in voltage and current (and therefore power output) at a critical time. This is not surprising realizing the fact that for a sufficient amount of fuel to diffuse back to the anode and reach its bare carbon fibers to react electrochemically, the product (say, BQS) should diffuse at almost the same rate from the electrode back to the pad, i.e., where its concentration is low. In practice, however, this balance can be distorted as time progresses. As can be seen in Fig. 5.15, after t = 60 min, the amount of product (BQS) diffused from the anode to the pad is insignificant as compared with that of fuel crossed over to the positive side. In practice, this can unbalance the cell and eventually lead to the anode starving for the fuel at some point in time (called the “critical time”) as predicted in Figs. 5.13 and 5.14.

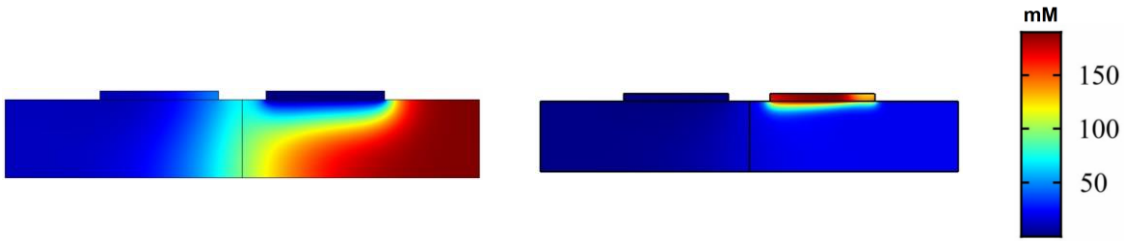

H2BQS (fuel) BQS (product)

Figure 5.15. Contour plots for H2BQS and BQS species after t = 60 min with no parasitic crossover included in the analysis (4h-2000 system).

To ensure that the concept of “back-diffusion”, as outlined above, is indeed valid we should obtain results at another pad thickness. If this concept is correct, it is speculated that by decreasing the thickness of the pad, the critical time should be completely removed or, at least, postponed to a larger time. This is because (at the same point in time) a thinner pad provides a larger concentration gradient and therefore a stronger back-diffusion from the pad to the electrodes. Figure 5.16 shows that this is indeed the case. That is to say that, there is no critical time for this pad system. It is therefore concluded that “back-diffusion” is indeed the working principle for the PowerPAD; see, also, Appendix D in which a one-dimensional analysis has been worked out to introduce the concept of back-diffusion time constant.

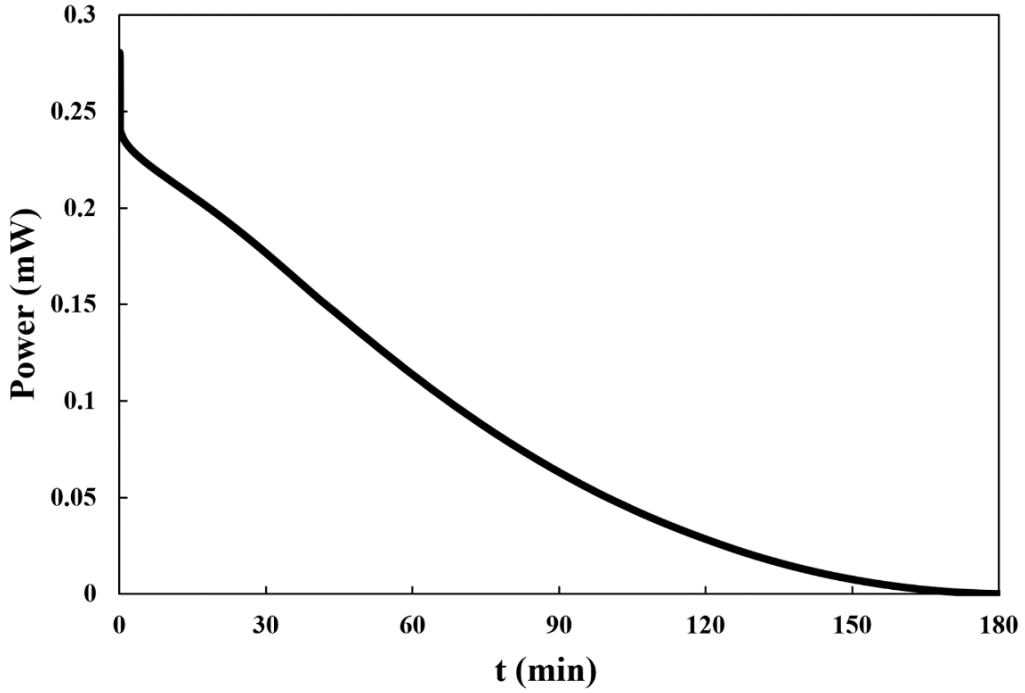

Figure 5.16. Decay of power output with time for the 2h-pad system with no parasitic crossover included in the analysis (R_{ex} = 2000 Ω).

Another explanation for the sudden drop in performance in Fig. 5.14, can be attributed to the ohmic loss becoming exceedingly large. The fact is that, as time progresses, protons are constantly consumed in an already-dilute electrolytes so that the SOC of the cell is reduced with time. Based on Eq. 3.16, a drop in SOC, and therefore proton concentration, translates itself into a drop in ionic conductivity and therefore an abrupt

increase in ohmic resistance of the electrolyte. This means that the slope of the instantaneous polarization curve sharply increases as time progresses (see Fig. 3.7). As a result, the operating point of the cell approaches the origin in an accelerative manner. In practice, this “ohmic-loss” limitation can work in parallel to the “mass-transport” limitation and give rise to the critical time predicted in Fig. 5.13.

5.7. Summary

In this Chapter we have tried to validate our mathematical model (described in Chapter 3) and numerical model (described in Chapter 4) against the unsteady experimental data reported in [16] for the PowerPAD. In the course of validating our code, we have reached to the conclusion that PowerPAD works on the principle of “back-diffusion”. That is to say that, the fuel which has been collected in the pad after originally passing through the electrode should diffuse back to the electrode for the cell to be able to function for more than an hour. Our results also show that the cell should suffer from a sudden drop in performance at a critical time either because of “mass-transfer” limitation or “ohmic-loss” limitation, or both. It was also found that the cell is vulnerable to crossover, and this is particularly so at prolonged times. The critical time was shown to drop by as much as 50% when crossover is included in the analysis. Since the effect of “mass-transfer” limitation and “ohmic-loss” limitation exhibit themselves at times much longer than the critical time corresponding to the crossover, it is concluded that among all parameters which can potentially limit the functionality of the PowerPAD (e.g., kinetic loss, ohmic loss, mass transport loss, migration, and crossover) it is the “crossover loss” which is the real “limiting factor” for this particular cell. Our results also suggest that the thickness of the pad can be used as a decisive tool for controlling the degree of back-diffusion. In the next Chapter we will show that there are other parameters that can control back-diffusion and/or the severity of crossover for the PowerPAD.

Chapter 6:

PowerPAD Design Optimization

6.1. Introduction

The level of power output generated by the PowerPAD and also its runtime are good enough for applications such as diagnostic kits. But, it is possible to extend its range of applicability and this can be achieved through proper design modifications and optimizations. In Chapter 5, we have seen that the mathematical methodology and numerical scheme developed in this thesis can successfully simulate both steady and unsteady performance of the existing PowerPAD design [16]. In this chapter, the same methodology will be used to see if the electrochemical performance of this flow cell can be further enhanced.

6.2. Extending the Runtime of PowerPAD

There are several methods by which the runtime of the PowerPAD can be enhanced. Any alteration of the parameters listed below can affect the performance of the device:

1. Redox couples
2. Electrolyte
3. Flow architecture
4. Electrode material and/or its geometry
5. Absorbent pad microstructure and/or its geometry

Obviously, these ideas can be combined with each other to come up with the best design. But, some of these ideas may be too ambitious. The *first* option appears to belong to this category. Although research on new quinone redox couples is ongoing in several research centers and institutions around the world, as it stands, we are short of options in this area. The *second* option is concerned with the notion that although the mixed-media (acidic/basic) concept utilized in PowerPAD has enabled this cell to attain a larger equilibrium potential (0.95 V), it has made the cell quite sensitive to pH-differential, and this can worsen the Galvani potential drop. As to the *third* option, it should be stated that this idea has already been tried at an early stage of this project (using vanadium species) and it was found to affect PowerPAD's polarization curves. It

is anticipated that flow architecture would also influence the unsteady behavior of the cell. With this in mind, we intend to try this idea in this part of the work.

The *fourth* option is also a viable option. The fact is that Toray electrode is not necessarily the best electrode available in the market for use in PowerPAD. There are other options that offer a larger specific area (for example, Sigracet 25 SGL carbon electrode). If for any reason we decide to stick to the Toray electrode, we can change its geometrical parameters; for example, we can vary the gap between the electrodes or its width. The *fifth* option is also an easy and affordable option. The fact is that, a variety of absorbent pads are available in the market with different microstructures. So, we can easily switch to other types of absorbent pads. But, we can also stick to the current absorbent pad (Ahlstrom 222) by simply making the pad thicker. Evidently, we have many options to control the power output and runtime of the PowerPAD, and we can combine these design modifications in order to achieve the highest performance. With this in mind, here we focus on the last three options (3,4, and 5).

Before proceeding, we stress that although crossover has been identified as a “limiting factor” for the PowerPAD, for a parameter study which aims at finding the relative role of influential parameters, we can temporarily exclude parasitic side-reactions from the initial analysis and defer it for the *optimized* design at the end of this chapter. This little maneuvering would reduce computational cost and effort. With this in mind, in subsequent sections we investigate the effect of different parameters on the cell performance. As earlier mentioned, the main objective is to see how the power and runtime of the PowerPAD can be extended by a proper selection of the pertinent parameters.

6.3. Flow Architecture

It is speculated that the cell’s performance in unsteady mode is affected by the flow architecture. To check this idea, the absorbent pad was extended to fill the gap between the electrodes. Figure 6.1 shows schematically this design modification. As can be seen in this figure, this idea enables the electrolytes to enter the pad also through the gap. As

such, this design will be referred to as the *mixed-flow* design because while flowing directly through the porous electrodes, the electrolytes simultaneously flow laterally.

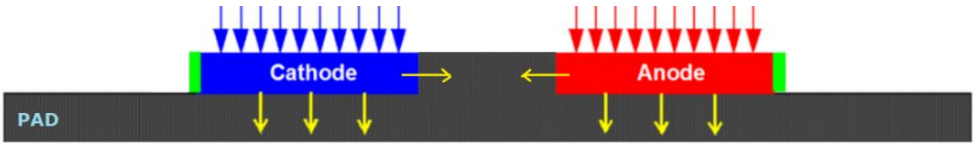

Figure 6.1. Schematic showing mixed-flow design where electrolytes can enter the pad horizontally from the inner side planes.

Figure 6.2 shows the variation of saturation field with time for this design. This figure shows that as soon as the electrolytes enter the pad, they start flowing laterally quite fast. In fact, based on the results obtained in these simulations, the two liquids first meet each other along the mid-plane at **t = 0.19 sec** (as compared with 0.33 sec for the vertical-flow design). But, like the vertical-flow design, the pad becomes fully-wet after roughly 5 seconds. And, after roughly 10 seconds the cell becomes fully-saturated. At this point in the saturation inside the pad is roughly equal to S = 0.93.

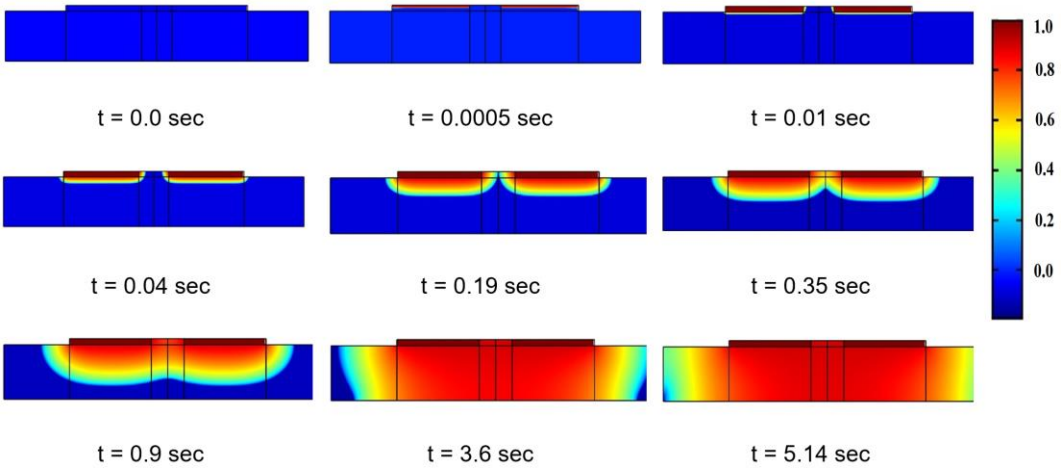

Figure 6.2. Time evolution of the saturation field for the mixed-flow design (4h-pad system).

Figure 6.3 shows the polarization curve for the mixed-flow design and its comparison with the vertical-flow design. Based on this figure it appears that the mixed-flow design is a better design. This effect can be attributed to the fact that this design benefits from having a reduced ohmic loss. That is to say that, the height of interface is larger for this

design (by exactly the thickness of the electrode), and so the area available for proton exchange is larger in this design. Figure 6.4 shows that the mixed-flow design slightly outperforms the vertical flow design during the cell's unsteady mode of operation. The gain in power output and runtime are roughly 5% with this design.

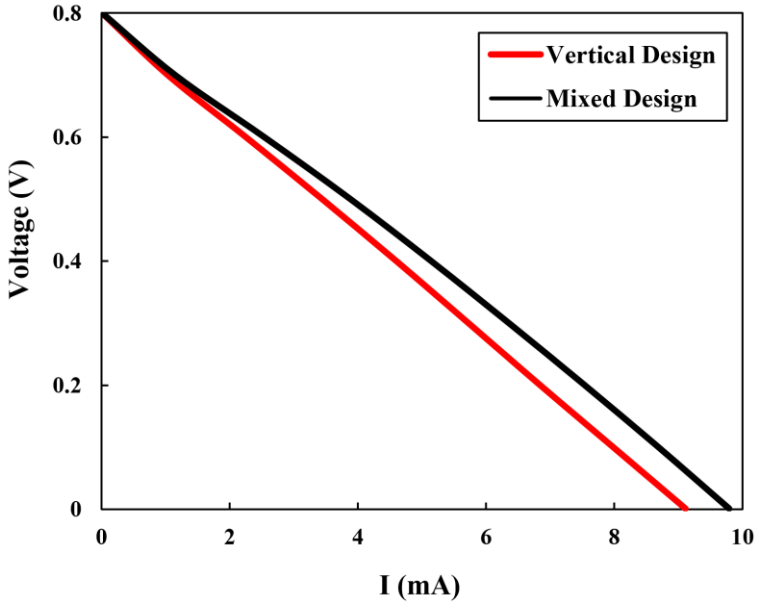

Figure 6.3. Polarization curve of the mixed-flow design and its comparison with vertical-flow design (4h-pad).

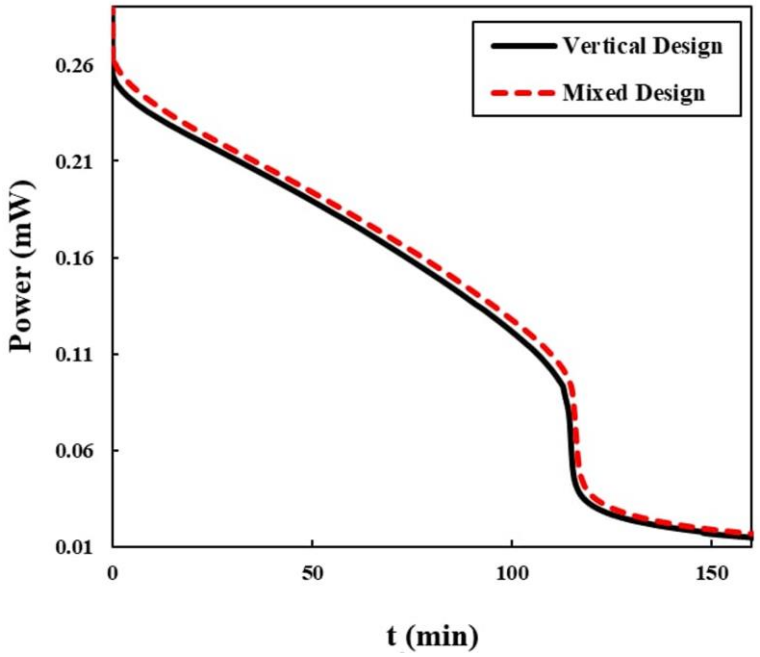

Figure 6.4. Time-dependent response of mixed-flow design and its comparison with vertical-flow design (4h-2000) without considering crossover.

6.4. Electrode Parameters

Electrode is the most crucial part of any flow cell and its parameters have a direct effect on the system performance. For a given electrode (say, Toray TGP-120) it is conceivable that by changing its geometrical parameters (for example, gap distance or width), polarization curve and therefore the power output of the cell can be controlled. It is also possible to completely replace the current electrode with a new one having a different microstructure. In this sub-section we try both ideas.

6.4.1. Effect of Gap Distance

If we decide to stick to the current Toray electrode, the easiest option to change the cell's performance is through changing the gap distance between the electrodes. The gap currently used in PowerPAD is 2 mm. We can make the gap larger or smaller. By so doing, the length of the electrode, and therefore its active area, is slightly increased, and this can enhance the system performance. Figure 6.5 shows that the gap distance (δ) indeed affects the polarization curves. In fact, in terms of polarization curve, the best performance corresponds to the smallest gap of δ = 1 mm. But, as can be seen in Fig. 6.6, for this smaller gap size, the sudden drop in power occurs at a shorter critical time. This effect can be attributed to the fact that by reducing the gap distance, it has become easier for a species to cross over the opposite electrode and undergo parasitic electrochemical reactions. In terms of efficiency, the three gaps are found to exhibit nearly the same performance (not shown here).

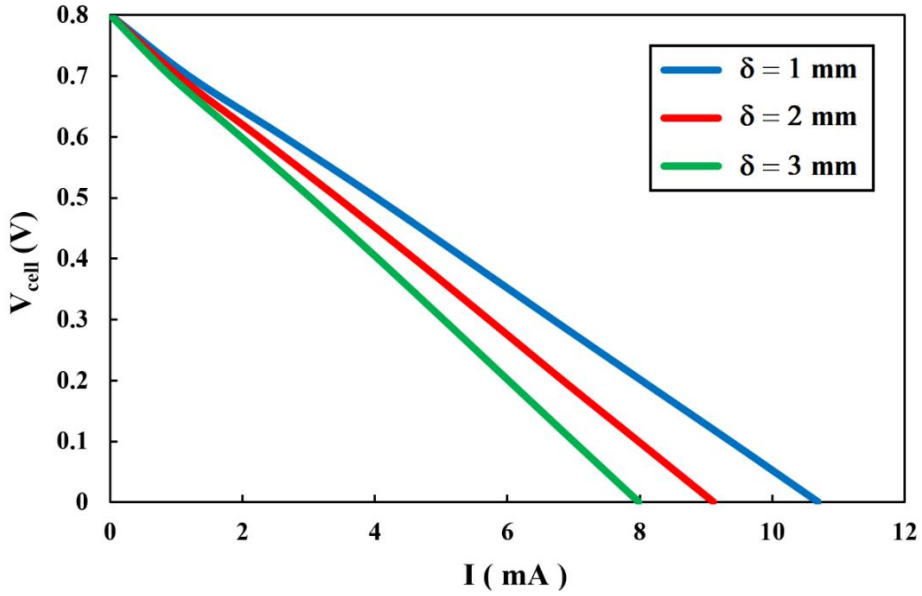

Figure 6.5. Effect of gap distance on the polarization curves of PowerPAD (4h-pad system).

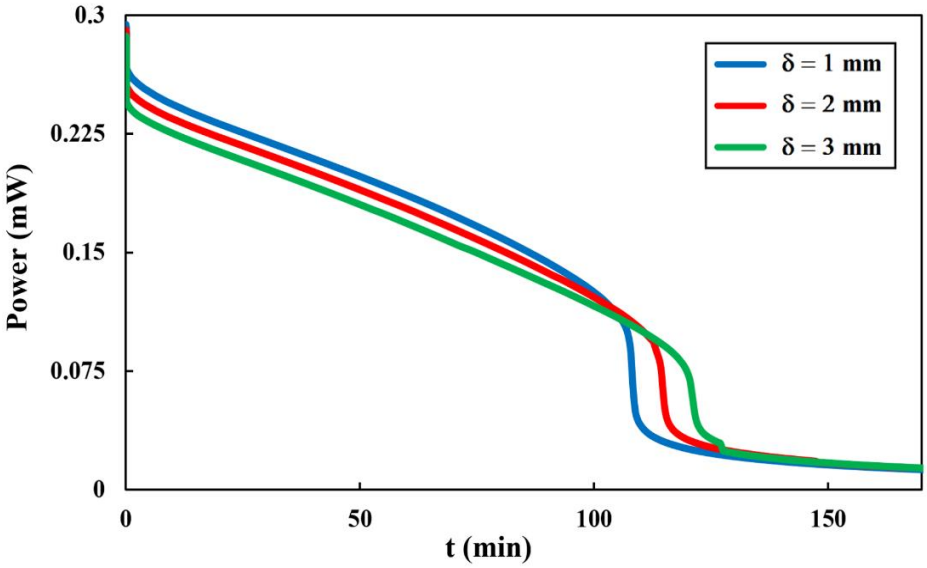

Figure 6.6. Effect of gap distance on the unsteady behavior of PowerPAD (4h-2000 system).

6.4.2. Effect of Specific Area

Specific area is an important parameter in a flow cell as it controls the source term in the Nernst-Planck equation (see Eq. 2.18). It is a well-established fact that, an increase in specific area can directly improve system performance. In a recent work, Goulet et al.

[72] have shown that the specific surface area of Toray papers can be enhanced by an order of magnitude through depositing carbon nanotubes on the carbon fibers. Another idea is to use electrodes made of porous carbon fibers which provide a large surface [73]. There are also technologies that can produce fibers of arbitrary diameter for use in electrodes [74,75]. The fact is that the specific area of Toray electrode is not very high (say, 8.33 x 10^4 m^2/m^3). As earlier mentioned, a better option would be to use Sigracet (SGL-25) carbon-fiber electrode which has a specific surface area wround 200,000 m^2/m^3. Figure 6.7 compares the performance of these two electrodes in regard to the polarization curves. As can be seen in this figure, the polarization curve for the Sigracet electrode is better than that of the Toray electrode. More importantly, the critical time of the PowerPAD is predicted to increase if use is made of the Sigracet electrode; see Fig. 6.8. This figure clearly shows using Sigracet electrode, the critical time is increased by roughly 10%. We have also computed the energy efficiency of these two electrodes but they have found to be virtually the same (not shown here). In other words, in terms of efficiency, there is not much to separate these two electrodes.

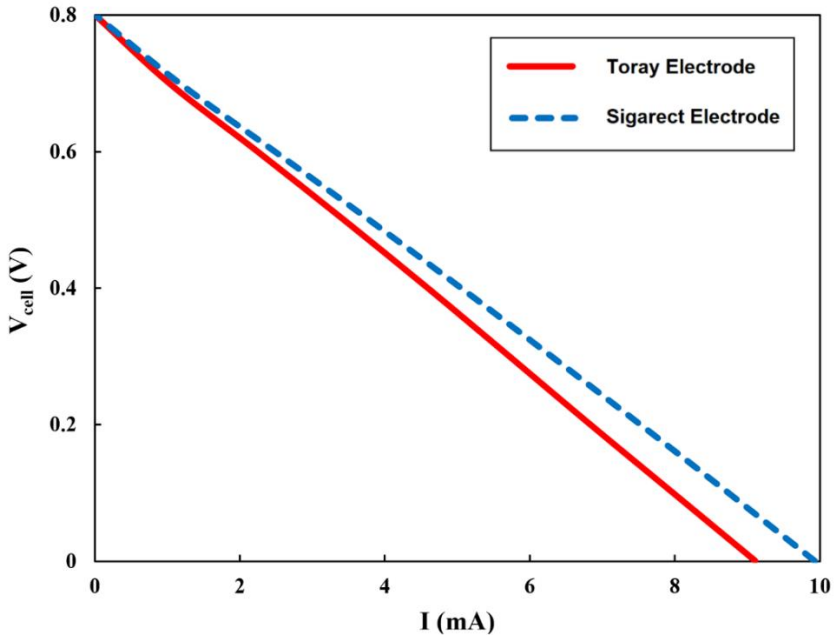

Figure 6.7. Effect of specific area on the polarization curve of the PowerPAD (4h-pad system).

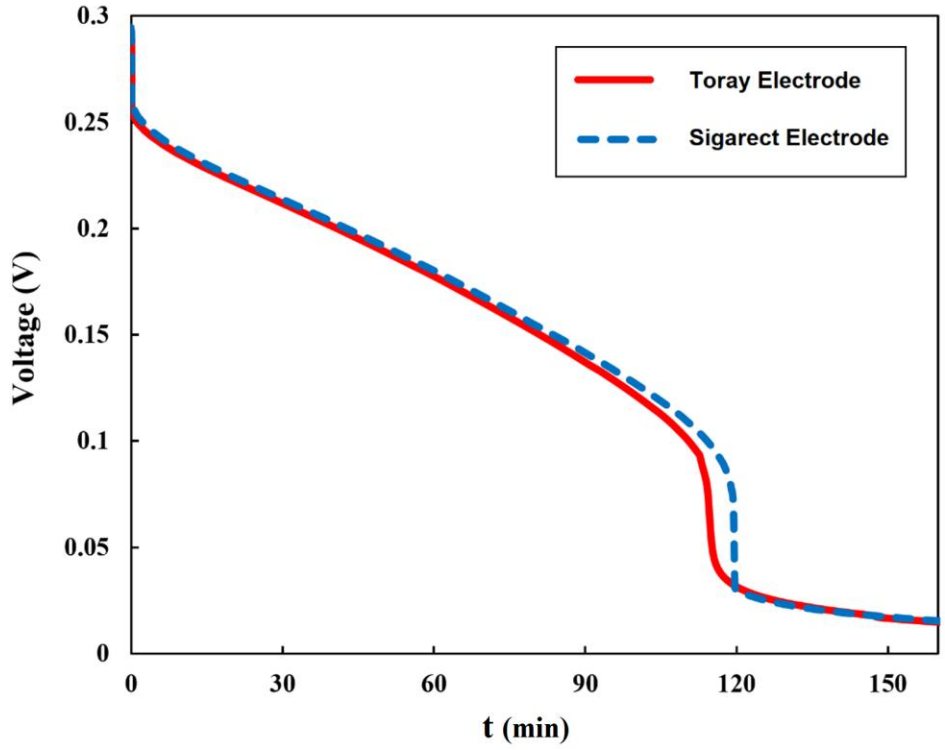

Figure 6.8. Effect of specific area on the runtime of the PowerPAD (4h-2000 system).

6.4.3. Effect of Width

The width of the electrode in the original PowerPAD's was 5 mm while the width of its absorbent pad was 20 mm (both in the y-direction). Obviously, we have rooms to increase the width of the electrodes in the y-direction in our 2D model. In this sub-section, it is assumed that the width of the electrode is 10 mm with its pad being also 10 mm. Note that the width of the electrode and the pad should match each other for the 2D assumption to remain valid. Figure 6.9 shows that the polarization curve is significantly improved by increasing the width of the electrodes. In fact, for any given cell voltage the current is doubled when the width is doubled. What is more important is the prediction that the critical time is roughly doubled by this simple idea; see Fig. 6.10. This is not surprising realizing the fact that the current collected by the electrode is proportional to W; see Eq. 3.21. The price is that the new cell exhibits a smaller energy efficiency; see Fig. 6.11.

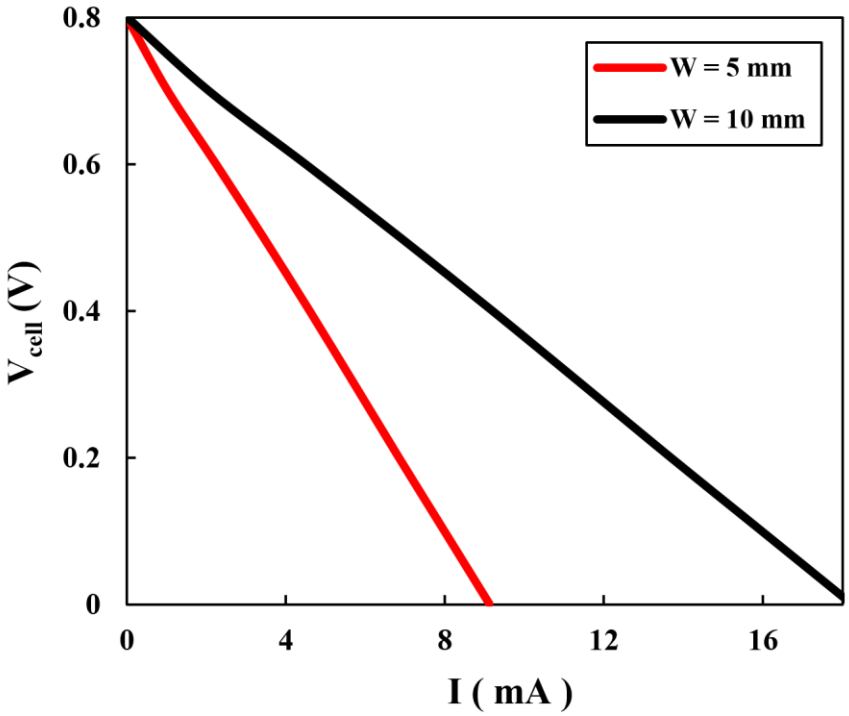

Figure 6.9. Effect of electrode width on the polarization curve of PowerPAD (4h-pad system).

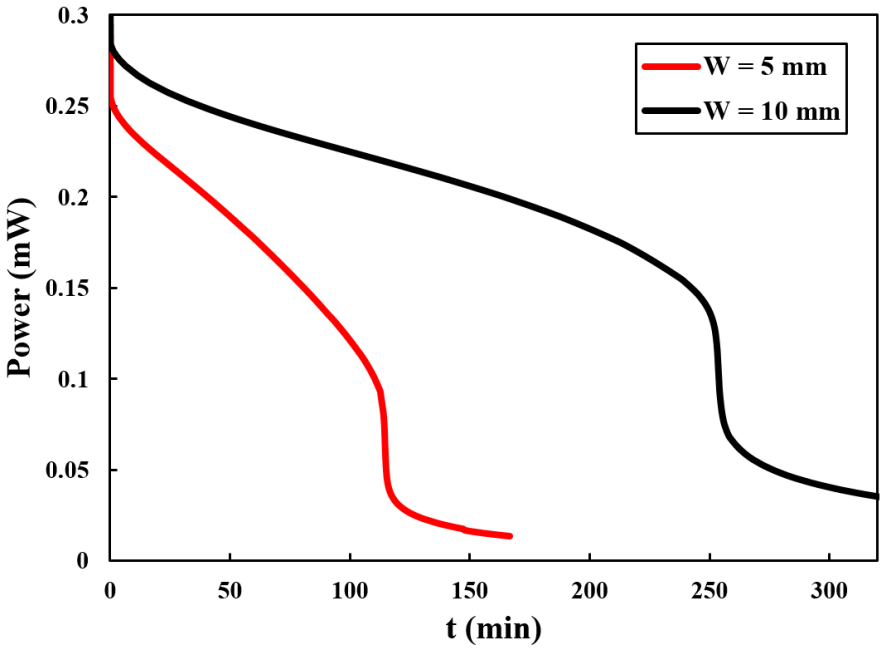

Figure 6.10. Effect of electrode width on the efficiency of PowerPAD (4h-2000 system).

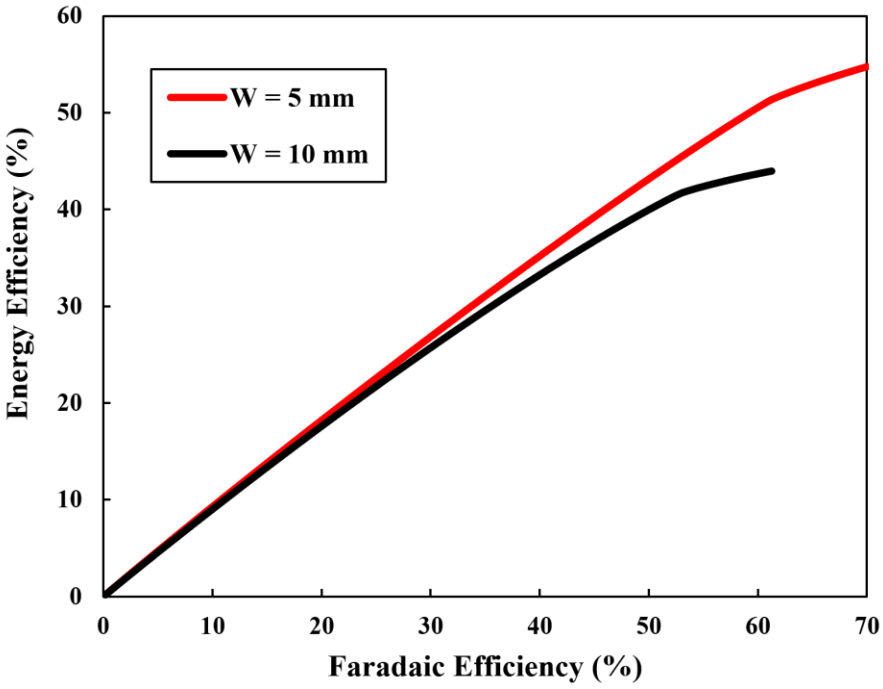

Figure 6.11. Effect of electrode width on the efficiency of PowerPAD (4h-2000 system).

6.5. Absorbent-Pad Parameters

We can stick to the current absorbent pad (namely, Ahlstrom 222 membrane) and just alter its dimensions (length, width, thickness) in order to control the cell's performance. The easiest idea is to increase the pad thickness — an idea that has already been tried experimentally in [16] and shown to be very influential. We can also employ a new filter pad from another manufacturer with a different microstructure (e.g., porosity). Here, we try both ideas.

6.5.1. Effect of PAD Thickness

Pad thickness is the easiest parameter to alter because all we have to do is to add another membrane to the last in the series. To that end, two more pad systems were considered for the simulations: 6h-pad and 8h-pad. Figure 6.12 shows the polarization curves for these two new pad systems. For comparison purposes, polarization curves for the other two pads have also been included in this figure. This figure shows that by increasing the pad thickness, the polarization curve is improved. This is as expected

because the internal ohmic resistance is reduced when a larger thickness is used. That is to say that, a larger thickness means a larger cross-sectional area and this makes it easier for the ions to be exchanged at the interface. But, based on Fig. 6.12, the effect of pad thickness on the polarization curve appears to become less significant the larger the thickness. This is apparently because back-diffusion becomes progressively more difficult for the ions when the thickness of the pad is increased. A weakened back-diffusion of the thicker pads can also affect the unsteady mode of operation. To check this, having found the new polarization curves, we can intersect them with any given external load, for example, 2000-Ohm load and proceed with the unsteady analysis.

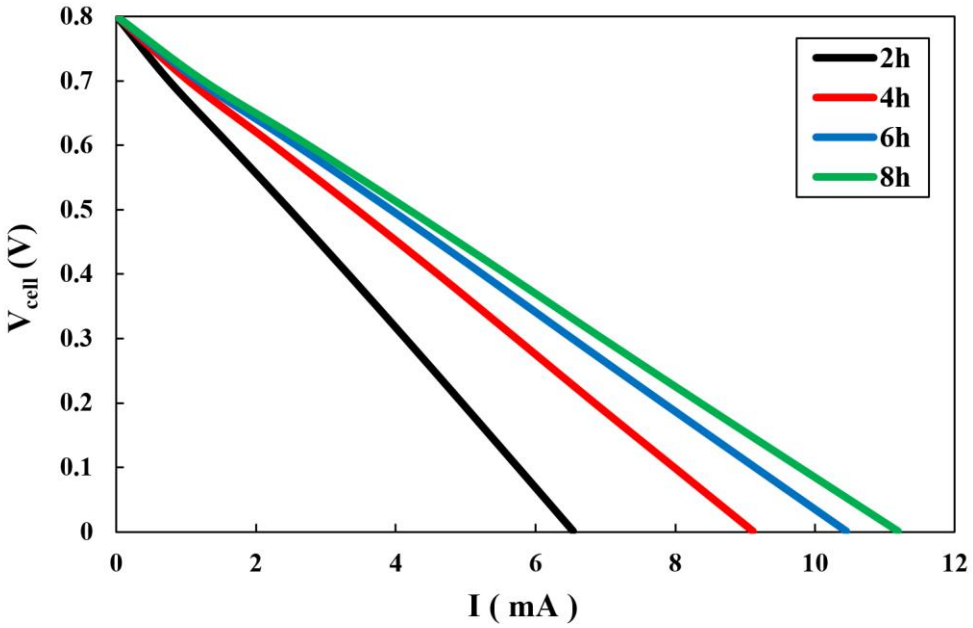

Figure 6.12. Effect of pad thickness on steady polarization curves of the PowerPAD.

Figure 6.13 shows the effect of pad thickness on the cell's runtime. According to this figure, the operating time of the PowerPAD can indeed be enhanced by increasing the pad thickness. The effect, however, appears to saturate if the pad's thickness is exceedingly large. To be more specific, there is more gain by going from 2h to 4h as compared with going from 6h to 8h. As can be seen in Fig. 6.14, there is a price for using this method and that is a drop in the cell's efficiency although it appears to be marginal.

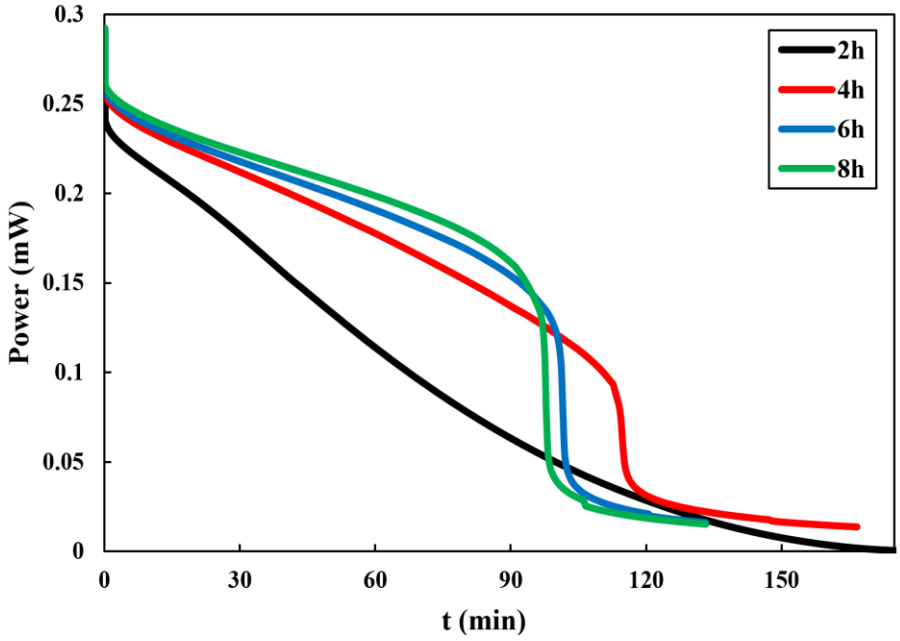

Figure 6.13. Effect of pad thickness on the runtime of PowerPAD at prolonged times. (R_{ex} = 2000 Ohm).

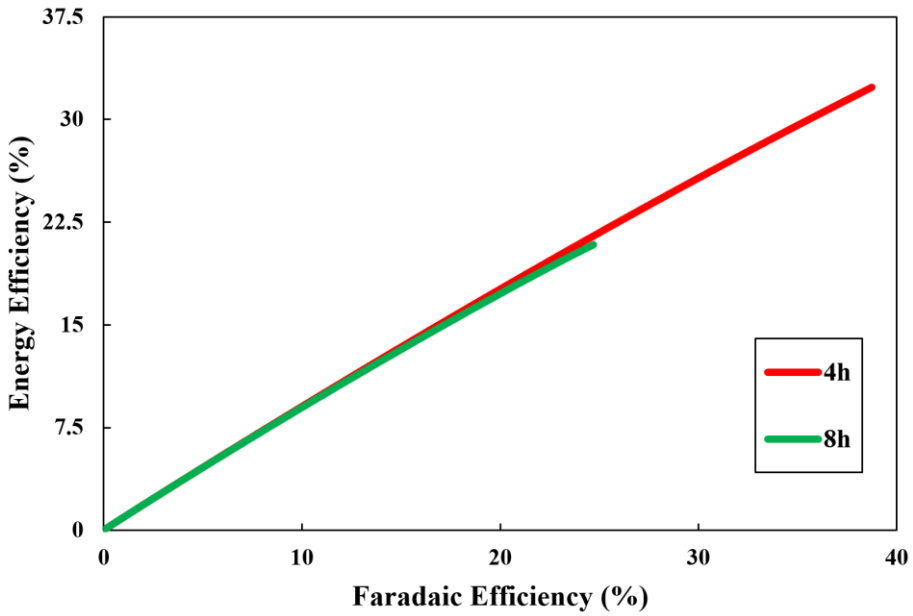

Figure 6.14. Effect of pad thickness on the efficiency of PowerPAD (R_{ex} = 2000 Ohm).

6.5.2. Effect of Pad Porosity

Porosity is perhaps the most influential parameter of any porous material. In our mathematical model, it appears itself before the unsteady term in the Nernst-Planck equation. Thus, it is expected to affect the unsteady mode of operation for the PowerPAD. Figure 6.15 shows the effect of porosity on the polarization curves. Note that in this figure $\varepsilon = 0.7$ corresponds to the pad material currently used in the PowerPAD (namely, Ahlstrom 222 grade). This figure shows that a larger porosity of 0.9 significantly improves the polarization curves. That is to say that, at a given cell voltage more current (and therefore more power) can be generated at this porosity. In fact, as can be seen in Fig. 6.16, by increasing the porosity of the pad, the critical time is just marginally reduced. So, in a sense, the effect of porosity is qualitatively similar to the effect of pad thickness. To explain the effect of a higher porosity, it should be noted that by so doing the amount of electrolyte that can be stored in the pad is increased. As a result, the amount of the reactants available for the electrochemical reactions also increases this way, and this gives rise to a better performance. The maximum efficiency of the cell is also slightly increased if use is made of more porous pads; see Fig. 6.17. Still, it can be argued that it is a better option than the original pad currently used in the PowerPAD design because it provides a higher power and a flatter power curve.

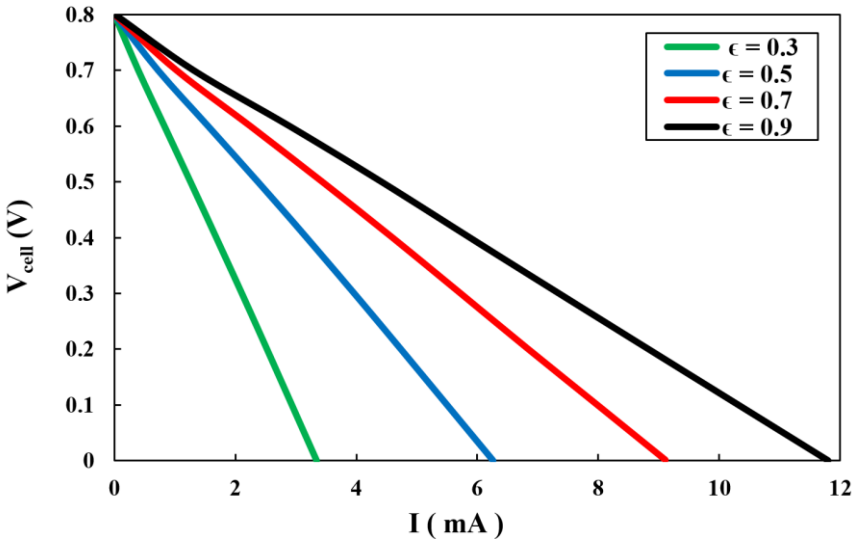

Figure 6.15. Effect of pad porosity on steady polarization curves of the PowerPAD (4h-pad system).

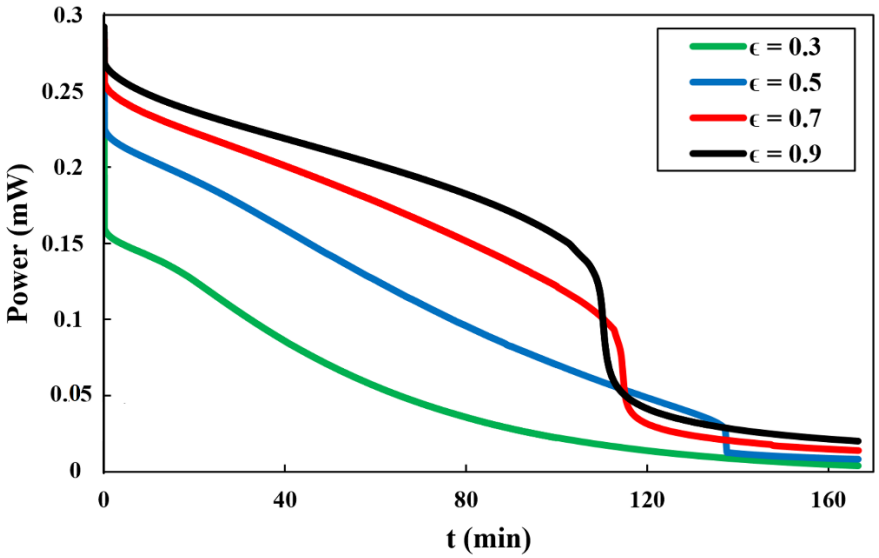

Figure 6.16. Effect of pad porosity on unsteady polarization curves of the PowerPAD (4h-2000 system).

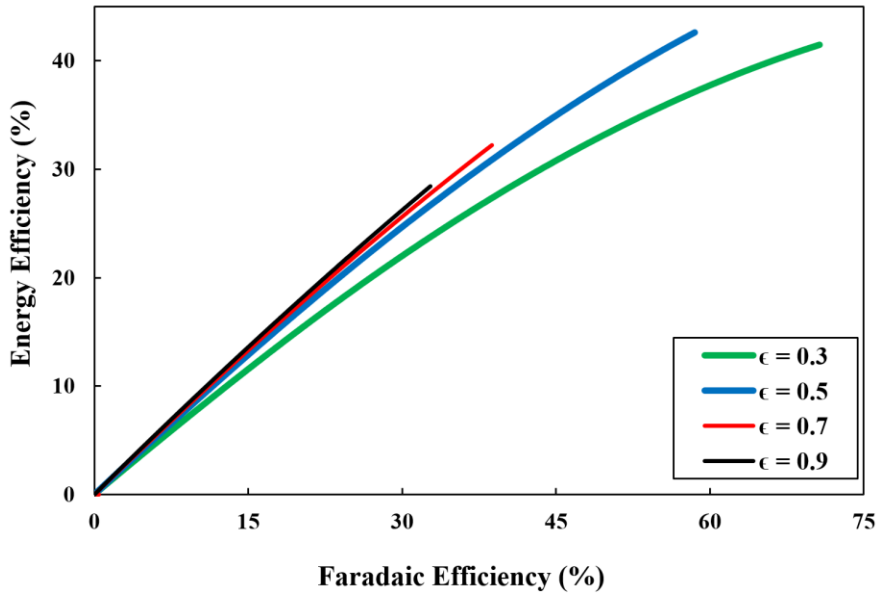

Figure 6.17. Effect of pad porosity on the efficiency of the PowerPAD (4h-2000 system).

6.6. The Optimized Design

From the results presented in the above sections it can be concluded that the runtime and power output of the PowerPAD can be enhanced using different strategies:

- By increasing the electrode's specific area
- By increasing the gap distance between the electrodes
- By increasing the width of the electrodes
- By increasing the thickness of the pad
- By increasing the porosity of its pad
- By adopting the mixed-flow architecture

These ideas can be combined with each other to render an *optimized design*. Since porosity of filter papers in the market (regardless of the brand) are all around 0.7, so it is better not to count on this option. Also, it is advisable not to make the optimized design too thick, so we stick to the 4h-pad system. Thus, as our optimized design we have: a = 2 x 10^5 1/m, δ = 3 mm, W = 10 mm, L = 5 mm, H = 3.32 mm, and ε = 0.7. For now, we ignore the effect of parasitic side-reactions. Figure 6.18 shows a sketch of the optimized design in Cartesian coordinate system.

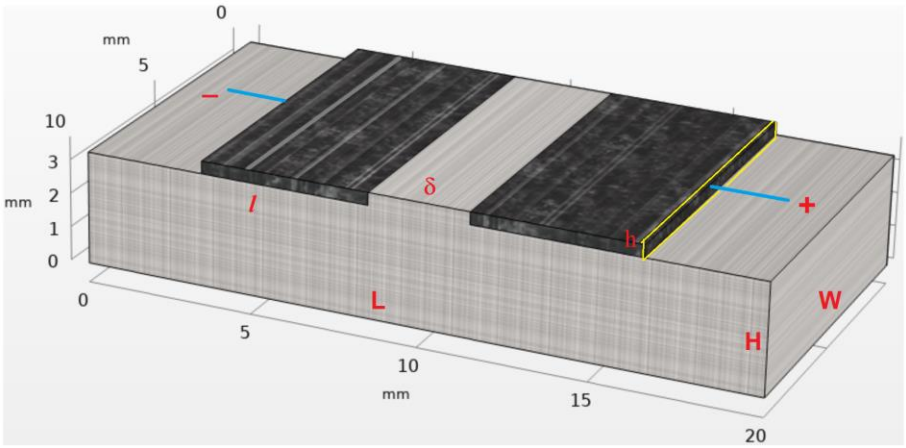

Figure 6.18. Scaled drawing showing the optimized design and its dimensions in Cartesian coordinate system.

Figure 6.19 shows the polarization curve for the optimized design (labelled "NEW"). This figure also includes the polarization curve for the current design (labelled "OLD"). Note that both designs are 2D models with their main difference being in the width of their

electrode/pad, which is 5 mm for the old design and 10 mm for the new design. Figure 6.19 shows that in terms of the polarization curves the new design outperforms the old design. That is to say that, at any given voltage it generates more current than the old design. This is not surprising realizing the fact that the current collected from a device is proportional to its width (see Eq. 3.13) and the new design is wider by two times. In addition, it benefits from other design features such as a Sigracet electrode enhanced surface area. And this is why it has an enhanced performance which exhibits itself by a shallower slope in its polarization curve; see Fig. 6.19. As a result, for any given load the operating point for the new design corresponds to a larger voltage and current and this is beneficial in our unsteady analysis. With the voltage and current of the operating point being larger for the new design, the power generated by this design is going to be larger at t = 0 in our unsteady analysis (i.e., when the cell is connected to an external load).

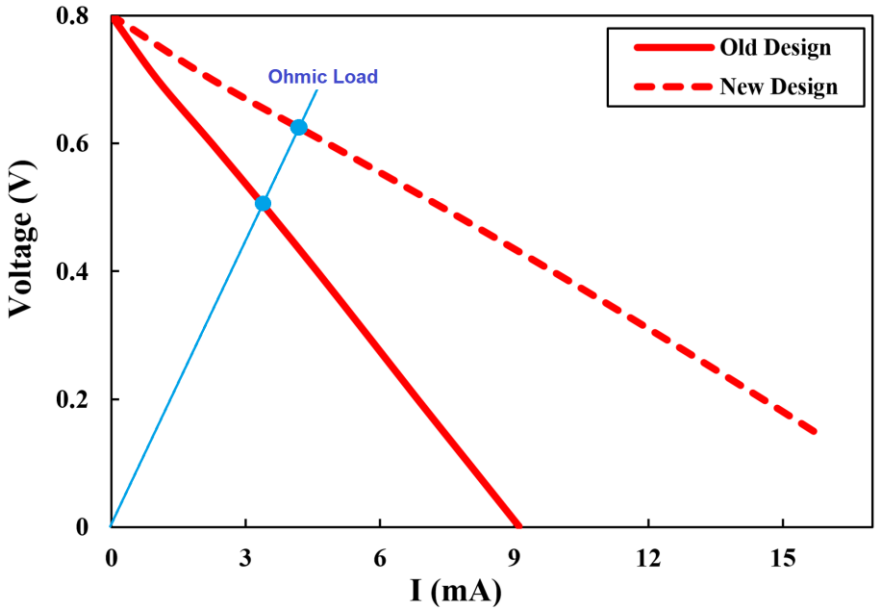

Figure 6.19. Comparison between polarization curves of the old and new designs (4h-pad system).

Figure 6.20 shows that this is indeed the case. That is to say that, at t = 0, the new design generates a larger power and a flatter time-decaying power curve which enables it to run for a longer time. To be more specific, while the critical time of the OLD design is 110 min, for the new design it is estimated to be around 230 min; see Fig. 6.20. On

the other hand, while at t = 110 min, the power output of the old design drops to roughly 0.04 mW, at this point in time the new design generates roughly 0.22 mW. (We could not capture a *true* critical time for the new design but based on the results presented in Fig. 6.20, if such a *time* indeed exists for this cell, it is definitely going to be longer than 230 min.)

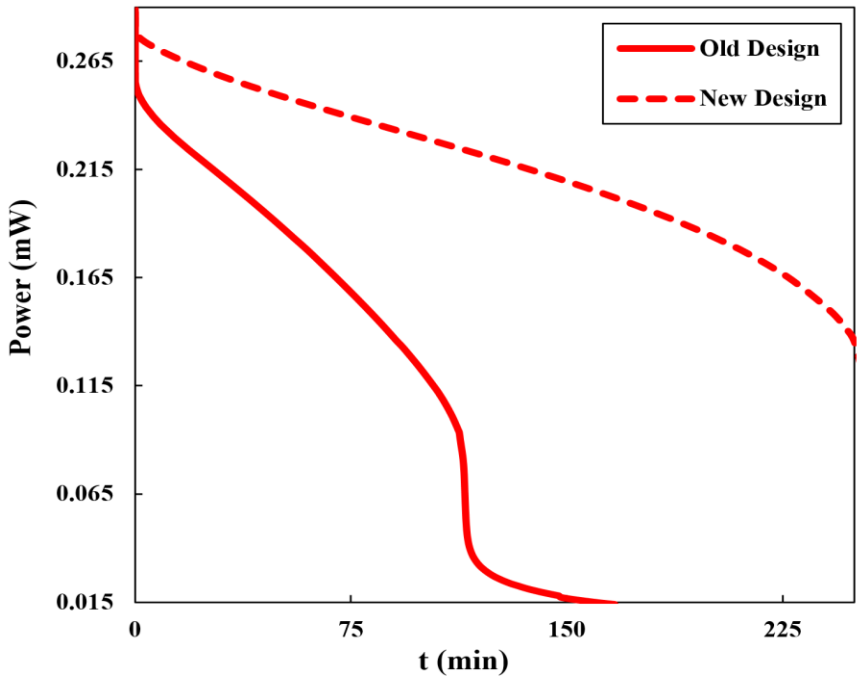

Figure 6.20. Comparison between the unsteady behavior of old and new designs *without* crossover (4h-2000 system).

In Chapter 5, we have already shown that the baseline design (which is referred to as old design in the present Chapter)`delivers its maximum power at a small external load of 88 Ω while in [16] three different loads of 500 Ω, 1000 Ω, and 2000 Ω were tried in the experiments. The conclusion is that, in the experimental setup used in [16] the power generated by the PowerPAD was far from the maximum value that it was potentially capable of generating. In other words, the cell could have generated a much larger power if use could be made of smaller external loads. For the old design, the optimized load is 88 Ω—we can show that it drops to 42 Ω for the new design. The prediction is that the maximum power output of the PowerPAD requires a load of the order of 10 Ω or 100 Ω but definitely not 1000 Ω. But using smaller loads may not

always be justifiable. The problem with this idea is that by using smaller loads of this order, the cell's runtime becomes much shorter. This might not be desirable in all applications although it looks fine for certain rapid diagnostic kits, where test results must be delivered in a couple of minutes (e.g., glucose test kits).

Based on the results shown in this section, the new (say, optimized) design outperforms the current design used in PowerPAD in terms of power and runtime. We can show that this is also true in terms of the efficiency. Figure 6.21 compares the efficiency of the two designs. First of all, this figure shows that for each design, the cell's efficiency is increased as time progresses. This is not surprising because the numerator in Eqs. 5.9 and 5.10 can only grow with time. What is more interesting is the behavior of the two designs in terms of their efficiencies.

As can be seen in Fig. 6.21, at short times the old design outperforms the new design but at long times it is the new design which is more efficient. The prediction that at short times the old design has a higher efficiency can be attributed to the fact that in the denominator of the efficiency definitions (see Eqs. 5.9 and 5.10) we have the theoretical capacity (q_{th}) which is proportional to the volume of the electrolyte. And the volume of electrolyte for the new design is roughly twice that of the old design (simply because the width of its electrode and pad has been doubled). But, given enough time, for the new design the numerator grows to such an extent that its efficiency exceeds that of the old design. This is simply because the runtime of the new design is roughly three times larger than that of the old design. Since the runtime is the upper limit of the two integrals in Eqs. 5.9 and 5.10, it is no wonder that the efficiency of the new design should eventually overtake the old design. This notion can clearly be seen in Fig. 6.21 for the energy efficiency which reaches 55% for the new (and could rise even further if we could have continued obtaining converged numerical results for a longer time) whereas for the old design it reaches an asymptotic value of roughly 44%. So, looking at it from this perspective, the new design is evidently going to be much more efficient than the old design. That is to say that it extracts much more energy from the electrochemical reactions. To show this in better perspective, in Fig. 6.22 we have shown the two efficiencies in terms of each other, i.e., after eliminating the time. In this format, the

more efficient device is always on top of the less efficient device, and this is perhaps why in [57] this style has been used for presenting their efficiency results.

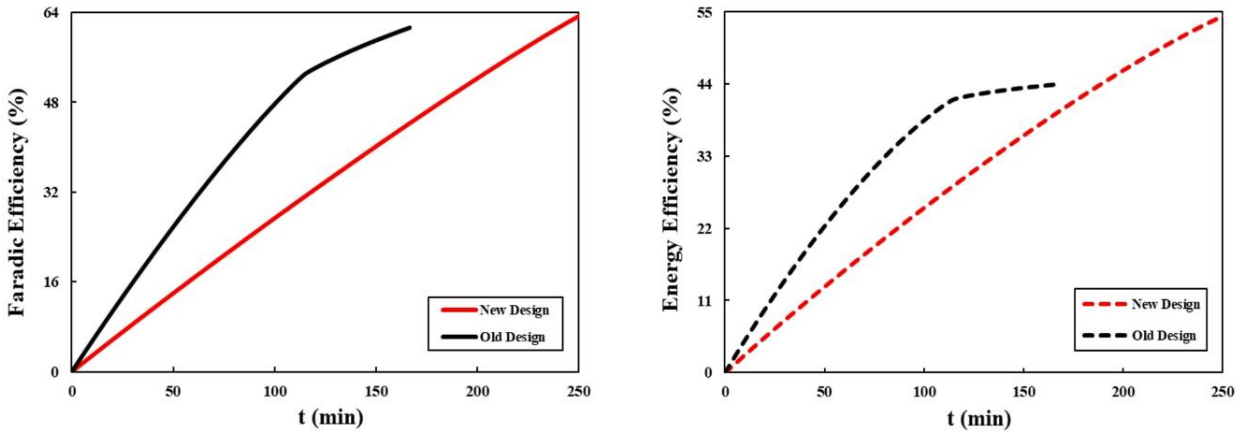

Figure 6.21. Comparison between time-dependent efficiencies of old and new designs (4h-2000 system).

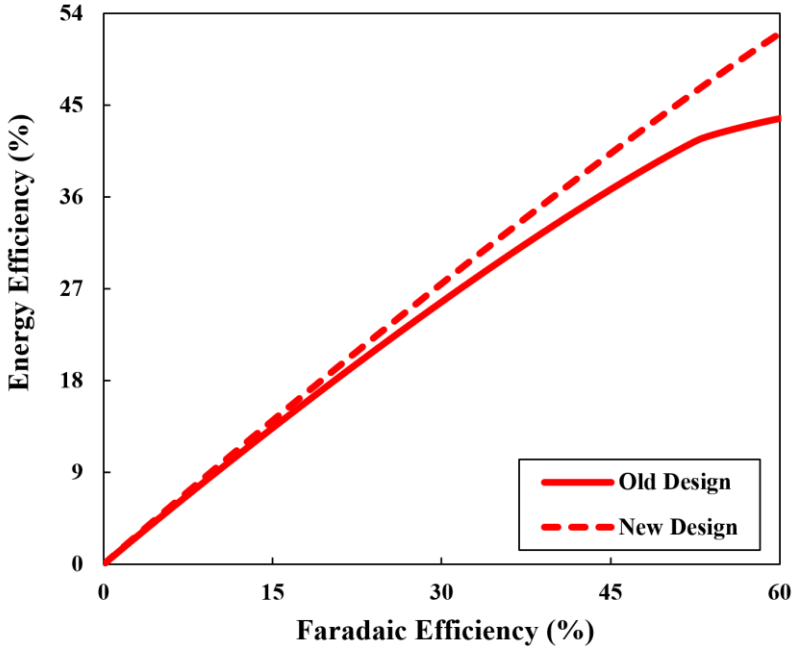

Figure 6.22. Comparison between efficiencies of the old and new designs (4h-2000 system).

In obtaining the above results, we have excluded the effect of parasitic side-reactions. Figure 6.23 shows the effect of crossover on the OLD and NEW designs. The OLD

design is seen to be much more vulnerable to parasitic side-reactions as compared with the new design. Based on the results presented in this figure, while for the old design the runtime is reduced from 110 min to roughly 85 min, for the optimized design it is predicted to be around 200 min. The gain in performance is obviously very significant. To be more specific, while the critical time of the old design is 85 min under crossover conditions, for the new design it is around 200 min. Also, while close to the critical time the power output of the old design is around 0.09 mW (see, also, Fig. 6.23), at this particular point in time the new design delivers power around 0.23 mW.

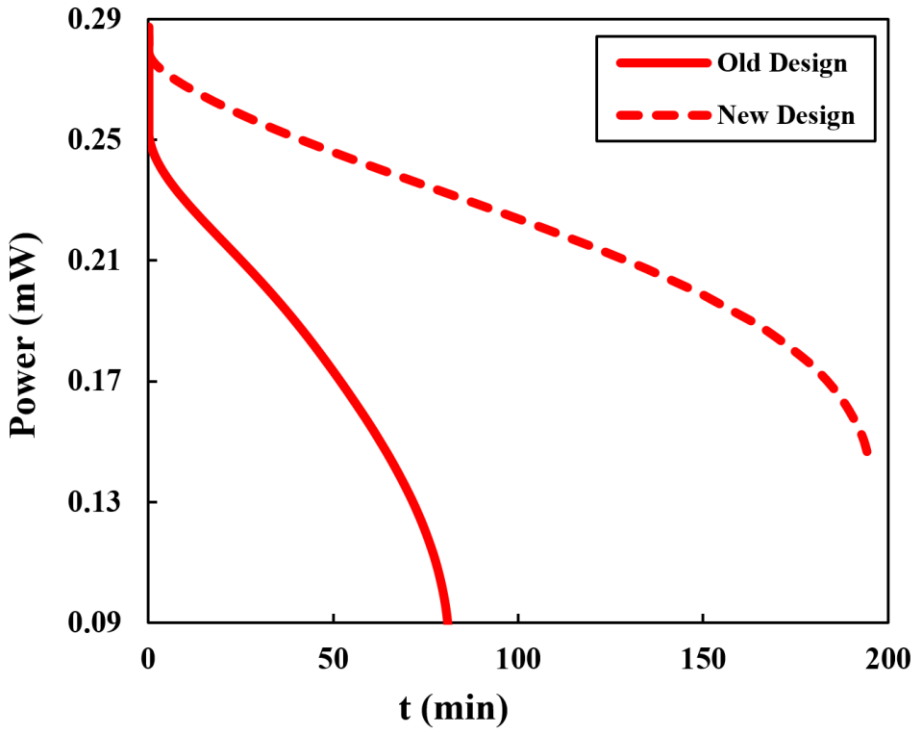

Figure 6.23. Effect of crossover on the unsteady behavior of old and new designs (4h-2000 system).

6.7. Summary

In this Chapter we have shown that the performance of the PowerPAD can be enhanced through modifying its flow architecture and the microstructure of its electrode and/or its absorbent pad. In the next Chapter the significance of our results and their impact on electrochemistry community is summarized. Also, suggestions are made as to how the work can be extended in ensuing studies.

Chapter 7:

Concluding Remarks

7.1. Summary

In this Master's thesis, a general mathematical/numerical framework has been developed which enables predicting the behavior of paper-based microfluidic flow cells in a systematic manner. A two-dimensional version of the model, after several simplifying assumptions, has been worked out and then validated against experimental data for a novel flow cell called PowerPAD, in both steady and unsteady modes of operation. The model could properly identify back-diffusion as the main principle underlying the functionality of this flow cell at prolonged times. The validated model also enabled us to investigate the effect of different parameters on the runtime and power output of this prospective flow cell. It was shown that the performance of the cell can be improved using a variety of design refinements chief among them are: 1) refining the geometry and/or microstructure of the electrode, 2) refining the thickness and/or the porosity of the absorbent pad, and 3) using mixed-flow design in place of the current vertical-flow design. An optimized design was proposed which roughly triples the runtime and power output of the PowerPAD. The optimized cell also exhibits a higher efficiency. All in all, the numerical results obtained in this thesis work suggest that although mass-transfer and ohmic-loss limitations are a real possibility for this cell, since the negative effects of crossover exhibits itself at a time scale much shorter than those introduced by mass-transfer and ohmic-loss limitations, thus "crossover" can be identified as the *limiting factor* for the PowerPAD. A simple analysis has shown that migration plays no role on the electrochemical performance of this particular cell.

7.2. Novelty of Thesis

This thesis work has several novelties as listed below:

1. An integrated mathematical model describing/predicting the electrochemical performance of paper-based capillary-driven flow cells has not been reported before in the open literature.
2. Richards model has not previously been used before for designing any type of microfluidic flow cell.
3. Crossover has not previously been studied for any all-quinone flow cell.
4. We are not aware of any 3D flow cell to have been modelled successfully using a 2D model in *unsteady* mode of operation.
5. Back-diffusion has not previously been identified as the working principle of capillary-driven flow cells.

7.3. Suggestions for Future Works

Future works should be aimed at experimentally testing the validity of numerical predictions made in this work. It is also suggested that, in future works, the effect of pH-differential be studied on the cell's performance, both experimentally and theoretically. Another area for future research is developing new electrolytes which can allow a higher concentration for the quinone species. (With the electrolytes currently used in the PowerPAD, the maximum concentration is just 0.2 M.) In the same vein, developing new and more effcient quinone redox couples could significantly enhance the electrochemical performance of the next-generation PowerPAD (say, PowerPAD 2). The model developed in this thesis is 2D, and it was a tricky business to validate it using 3D data in the unsteady mode of operation. With a proper hardware, we can attempt a 3D simulation and see by how much it differs from the 2D simulation used in the present work. In subsequent works the mathematical model developed in this work should be refined by incorporating the effect of temperature on the transport properties, for example, through invoking the Arrhenius equation [77]. The current model can also be extended by incorporating heat transfer effects through incorporating the energy equation in the analysis. Still, we would like to stress that, even in its current form, the mathematical developed in this work is robust enough to be used for design purposes.

That is to say that, we can design the cell such that it can mean a target power output and or a target runtime. The model can also be used in future works for designing next-generation flexible PowerPAD thanks to the notion that in recent years bendable carbon-fiber electrodes have become available [78]. This Flexi-PowerPAD can then be used for energizing wearable sensors, which is an active field of research.

7.4. Contributions to Date

The results of this thesis work have been presented in two international conferences. Also, a journal manuscript based on the numerical results obtained in this thesis work is currently under preparation. I have also contributed in writing a review-paper on microfluidic flow cells that is currently under review after receiving positive feedback from the first round of reviewing. These contributions have been listed below:

1. **P. Sadeghi**, O. Ibrahim, and E. Kjeang, “Numerical modelling of membrane-less flow batteries”, The Electrochemical Society: *PRiME-2020*, October 409, 2020.
2. **P. Sadeghi**, and E. Kjeang, “Numerical modelling of capillary-driven paper-based flow-through microfluidic redox flow-batteries”, *InterPore-2021*, May 31-June 4, 2021.
3. **P. Sadeghi**, M. Pourjafar, O. Ibrahim, and E. Kjeang, “Mathematical modelling of all-quinone, paper-based, microfluidic flow batteries”, *under preparation*.
4. O. Ibrahim, M. Navarro-Segarra, **P. Sadeghi**, N. Sabate, J. Esquivel, E. Kjeang, “Microfluidics for electrochemical energy conversion”, *Chem. Rev.*, *under review*, 2021.

References

[1] I. Buchmann, *Batteries in a Portable World: A Handbook on Rechargeable Batteries for Non-Engineers*, Cadex Electronics Inc., 3rd edition, 2011.

[2] J.F. Peters, M. Baumann, B. Zimmermann, J. Braun, and M. Weil, The environmental impact of Li-Ion batteries and the role of key parameters – A review, Renewable and Sustainable Energy Reviews, 67 (2017) 491–506.

[3] A.Z. Weber, M.M. Mench, J.P. Meyers, P.N. Ross, J.T. Gostick, Q. Liu, Redox flow batteries: A review, J. Appl. Electrochem. 41 (2011) 1137–1164.

[4] S. Shrivastava, T.Q. Tung, and N.E. Lee, recent progress, challenges, and prospects of fully integrated mobile and wearable point-of-care testing systems for self-testing, Chemical Society Reviews, 49 (2020) 1812-1866.

[5] S. Smith, J.G. Korvink, D. Mager, and K. Land, The potential of paper-based diagnostics to meet the ASSURED criteria, RSC Adv., 8 (2018) 34012.

[6] N. Nguyen, and S. Wereley, *Fundamentals and Applications of Microfluidics*, Artech House, (2006) 111.

[7] E. Kjeang, *Microfluidic Fuel Cells and Batteries*, Springer, 2014.

[8] R. Ferrigno, A.D. Stroock, T.D. Clark, M. Mayer, G.M. Whitesides, Membraneless vanadium redox fuel cell using laminar flow. J. Am. Chem. Soc., 124 (2002) 12930–12931.

[9] E.R. Choban, L.J. Markoski, A. Wieckowski, P.J.A. Kenis, Microfluidic fuel cell based on laminar flow, J.l of Power Sources, 128 (2004) 54–60.

[10] Y. Wang, S. Luo, H.Y.H. Kwok, W. Pan, Y. Zhang, X. Zhao, D.Y.C. Leung, Microfluidic fuel cells with different types of fuels: A prospective review, *Renewable and Sustainable Energy Reviews* 141 (**2021**) 110806.

[11] A.W. Martinez, S.T. Phillips, G.M. Whitesides, E. Carrilho, Diagnostics for the developing world: microfluidic paper-based analytical devices, Analytical Chemistry, 82 (2010) 3-10.

[12] A.K. Yetisen, M.S. Akram, C.R. Lowe, Paper-based microfluidic point-of-care diagnostic devices, Lab on a Chip, 13 (2013) 2210-51.

[13] V.T. Nguyen, S. Song, S. Park, and C. Joo, Recent advances in high-sensitivity detection methods for paper-based lateral-flow assay, Biosensors and Bioelectronics, 152 (2020) 112015.

[14] Y. Liu, L. Zhan, Z. Qin, J. Sackrison, and J.C. Bischof, Ultrasensitive and highly specific lateral flow assays for point-of-care diagnosis, ACS Nano, 15 (2021) 3593−3611.

[15] J.P. Esquivel, J.R. Buser, C.W. Lim, C. Domínguez, S. Rojas, P. Yager, and N. Sabat, Single-use paper-based hydrogen fuel cells for point-of-care diagnostic applications, J. Power Sources, 342 (2017) 442-451.

[16] J.P. Esquivel, P. Alday, O.A. Ibrahim, B. Fernández, E. Kjeang, and N. Sabaté, A metal-free and biotically degradable battery for portable single-use applications, Advanced Energy Materials, 7 (2017) 1700275.

[17] X. Pang, J.T. Davis, A.D. Harvey, D.V. Esposito, Framework for evaluating the performance limits of membraneless electrolyzers. *Energy and Environmental Science*, *13* (2020) 3663-3678.

[18] C. Brett, and A.M. Brett, *Electrochemistry: Principles, Methods, and Applications*, Oxford University Press, 1993.

[19] J. Newmann, and K.E. Thomas-Alyea, *Electrochemical Systems*, Wiley-Interscience, 3rd edition, 2004.

[20] G.L. Soloveichik, Flow Batteries: Current Status and Trends, Chem. Rev., 115 (2015) 11533–11558.

[21] F. Pen, and Q. Wang, Redox species of redox flow batteries: a review, Molecules, 20 (2015) 20499-20517.

[22] R O'Hayre, S.W. Cha, W. Colella, and F.B. Prinz, Fuel Cell Fundamentals, 3rd Edition, Wiley, 2016.

[23] J.B. Benziger, M.B. Satterfield, W.H.J. Hogarth, J.P. Nehlsen, I.G. Kevrekidis, The power performance curve for engineering analysis of fuel cells, Journal of Power Sources, 155 (2006) 272–285.

[24] A.A. Shah, M.J. Watt-Smith, F.C. Walsh, A dynamic performance model for redox-flow batteries involving soluble species, Electrochimica Acta, 53 (2008) 8087–8100.

[25] C.A. Kennedy, W.C. Lennox, A pore-scale investigation of mass transport from dissolving DNAPL droplets, Journal of Contam. Hydrol., 24 (1997) 221–246.

[26] P. Stoodley, S. Yang, H. Lappin-Scott, Relationship between mass transfer coefficient and liquid flow velocity in heterogenous biofilms using microelectrodes and confocal microscopy, Zbigniew Lewandowski. Biotechnology and bioengineering, 56 (1997) 681-688.

[27] Q. Xu and T.S. Zhao, Determination of the mass-transport properties of vanadium ions through the porous electrodes of vanadium redox flow batteries, Phys.Chem. Chem. Phys., 15 (2013) 10841-8.

[28] A. Xu, T.S. Zhao, L. Shi, and J.B. Xu, Lattice Boltzmann simulation of mass transfer coefficients for chemically reactive flows in porous media, J. of Heat Transfer, 140 (2018) 052601-8.

[29] J.L. Barton, and F.R. Brushett, A one-dimensional stack model for redox flow battery analysis and operation, Batteries, 5 (2019) 1-25.

[30] E.R. Choban, L.J. Markoski, A. Wieckowski, P.J.A. Kenis, Microfluidic fuel cell based on laminar flow, Journal of Power Sources, 128 (2004) 54–60 55.

[31] E.R. Choban, J.S. Spendelow, L. Gancs, A. Wieckowski, P.J.A. Kenis, Membraneless laminar flow-based micro fuel cells operating in alkaline, acidic, and acidic/alkaline media, Electrochimica Acta, 50 (2005) 5390–5398.

[32] R. Ferrigno, A.D. Stroock, T.D. Clark, M. Mayer, G.M. Whitesides, Membraneless vanadium redox fuel cell using laminar flow, J. Am. Chem. Soc., 124 (2002) 12930-12931.

[33] E. Kjeang, N. Djilali, and D. Sinton, Microfluidic fuel cells: A review, Journal of Power Sources, 186 (2009) 353-369.

[34] Z. Liu, X. He, J. Han, X. Zhang, F. Li, A. Li, Z. Qu, F. Xu, Liquid wicking behavior in paper-like materials: mathematical models and their emerging biomedical applications, Microfluidics and Nanofluidics, 22 (2018) 132.

[35] https://en.wikipedia.org/wiki/File:Capillary_flow_brick.jpg.

[36] R. Lucas, Rate of capillary ascension of liquids, Kollid Z., 23 (1918) 15.

[37] E.V. Washburn, The dynamics of capillary flow, Phys. Rev., 17 (1921) 273.

[38] K. Li, D. Zhang, H. Bian, C. Meng, Y. Yang, Criteria for applying the Lucas-Washburn law, Scientific Reports, 5 (2015) 14085.

[39] L.A. Richards, Capillary conduction of liquids through porous mediums, Physics, 1 (1931) 318–333.

[40] K. Jedvert, A. Idström, T. Köhnke, and M. Alkhagen, Cellulosic nonwovens produced via efficient solution blowing technique, J. Applied Polymer Science, 137(45) (2019) 48339.

[41] https://hdl.handle.net/10217/209006.

[42] R.H. Brooks, and A.T. Corey, Hydraulic Properties of Porous Media, Hydrology Papers 3, Colorado State University, Fort Collins, 1964.

[43] H. Huinink, Fluids in porous media: Transport and phase changes, Morgan & Claypool Publishers, (2016) 1–116.

[44] D. Krishnamurthy, E.O. Johansson, J.W. Lee, and E. Kjeang, Computational modeling of microfluidic fuel cells with flow-through porous electrodes, J. of Power Sources, 196 (2011) 10019– 10031.

[45] O.A. Ibrahim, P. Alday, N. Sabate, J.P. Esquivel, and E. Kjeang, Evaluation of redox chemistries for single-use biodegradable capillary flow batteries, J. of The Electrochemical Society, 164 (12) A2448-A2456 (2017).

[46] B. Yang, L. Hoober-Burkhardt, F. Wang, G.K.S Prakash, and S.R. Narayanan, An Inexpensive Aqueous Flow Battery for Large-Scale Electrical Energy Storage Based onWater-Soluble Organic Redox Couples, *Journal of The Electrochemical Society*, 161(9) (2014) A1371-A1380.

[47] M. Pavelka, F. Wandschneider, and P. Mazur, Thermodynamic derivation of open circuit voltage in vanadium redox flow batteries, Journal of Power Sources 293 (2015) 400e408.

[48] J. Geiser, H. Natter, R. Hempelmann, B. Morgenstern, and K. Hegetschweiler, Photometrical determination of the state-of-charge in Vanadium redox flow batteries, Part II: In combination with open-circuit-voltage, Z. Phys. Chem., 233 (12) (2019) 1683-1694.

[49] K.W. Knehr, E.C. Kumbur, Open circuit voltage of vanadium redox flow batteries: Discrepancy between models and experiments, Electrochemistry Communications, 13 (2011) 342–345.

[50] E. Makrlik, Galvani potential difference at the Interface between two immiscible electrolyte solutions, Z. Phys. Chemie, 267 (1986) 637-640.

[51] F. Reymond, D. Fermin, H.J. Lee, and H.H. Girault, Electrochemistry at liquid:liquid interfaces: methodology and potential applications, Electrochimica Acta, 45 (2000) 2647–2662.

[52] P. Peljo, M. Bichon, and H.H. Girault, Ion transfer battery: storing energy by transferring ions across liquid–liquid interfaces, Chem. Commun., 52, 2016, 9761-9764.

[53] A. Morita, A. Koizumi, and T. Hirano, Recent progress in simulating microscopic ion transport mechanisms at liquid–liquid interfaces, J. Chem. Phys., 154, 080901 (2021).

[54] A. Khataee, K. Wedege, E. Drazevic, and A. Bentien, Differential pH as a method for increasing cell potential in organic aqueous flow batteries, J. of Materials Chemistry A, 2017, 5(41) 21875-21882.

[55] T. Haisch, H. Ji, C. Weidlich, Monitoring the state of charge of all-vanadium redox flow batteries to identify crossover of electrolyte, Electrochimica Acta, 336 (2020) 135573.

[56] E. Kjeang, R. Michel, D.A. Harrington, N. Djilali, and D. Sinton, A microfluidic fuel cell with flow-through porous electrodes, Journal of the American Chemical Society, 130 (2008) 4000–4006.

[57] M. Navarro-Segarra, P.P. Alday, D. Garcia, O.A. Ibrahim, E. Kjeang, N. Sabaté, J.P. Esquivel, An organic redox flow cell-inspired paper-based primary battery, Chem. Sus. Chem., 13 (2020) 2394-2401.

[58] D. Rath, N. Sathishkumar, and B.J. Toley, Experimental Measurement of Parameters Governing Flow Rates and Partial Saturation in Paper-Based Microfluidic Devices, Langmuir , 34 (2018) 8758–8766.

[59] A. Perez-Cruz, I. Stiharu, A. Dominguez-Gonzalez, Two-dimensional model of imbibition into paper-based networks using Richards' equation, Microfluid. Nanofluid., 21 (2017) 1–12.

[60] S. Suo, M. Liu, and Y. Gan, Modelling imbibition processes in heterogeneous porous media, Transport in Porous Media, 126 (2019) 615–631.

[61] F. Marinelli, and D.S. Durnford. Semi-analytical solution to Richards equation for layered porous media, *Journal of Irrigation and Drainage Engineering,* 124.6 (1998) 290-299.

[62] T.J. *Santner, B.J. Williams, and W.I. Notz, The Design and Analysis of Computer Experiments, Springer Verlag, 2003.*

[63] P. *Bratley, B.L. Fox, L.E. Schrage, A Guide to Simulation,* Springer Science & Business Media*,* 2011*.*

[64] P. Dechaumphai, and S. Sucharitpwatskul, *Finite Element Analysis with Comsol*, Alpha Science International Ltd. Verlag, 2019.

[65] M. Landeryou, A. Cottenden, I. Eames, A. Frampton, Bulk liquid-transport properties of multi-layered fibrous absorbents, J. of the Textile Institute, 94 (2003) 67-76.

[66] C.P. De León, Redox flow cells for energy conversion, J. Power Sources 160, 716 (2006).

[67] R. Jiang, C. Rong, and D. Chu, Determination of energy efficiency for a direct methanol fuel cell stack by a fuel circulation method, Journal of Power Sources 126 (2004) 119–124.

[68] L.J. Small, H.D. Pratt, and T.M. Anderson, Crossover in membranes for aqueous soluble organic redox flow batteries, *Journal of The Electrochemical Society*, 166 (2019) A2536-A2542.

[69] I.B. Sprague, D. Byun, and P. Dutta, Effects of reactant crossover and electrode dimensions on the performance of a microfluidic based laminar flow fuel cell, *Electrochimica Acta*, 55 (2010) 8579–8589.

[70] J. Xuan, M.K.H. Leung, D.Y.C. Leung, and H. Wang, Laminar flow-based fuel cell working under critical conditions: The effect of parasitic current, *Applied Energy*, 90 (2012) 87–93.

[71] S.E. Ibáñez, A.E. Quintero, P.A. García-Salaberri, M. Vera, Effects of the diffusive mixing and self-discharge reactions in microfluidic membraneless vanadium redox flow batteries, International Journal of Heat and Mass Transfer*,* 170 (2021) 121022.

[72] M.A. Goulet, A. Habisch, E. Kjeang, In situ enhancement of flow-through porous electrodes with carbon nanotubes via flowing deposition, *Electrochimica Acta*, 206 (2016) 36–44.

[73] J. Kim, Y.J. Heo, J.Y. Hong, and S.K. Kim, Preparation of porous carbon nanofibers with tailored porosity for electrochemical capacitor electrodes, *Materials*, 13 (2020) 729.

[74] X. Mao, T.A. Hatton, and G.C. Rutledge, A review of electrospun carbon fibers as electrode materials for energy storage, *Current Organic Chemistry*, 17(13), 2013.

[75] J. Erben, A. Heußner, S. Thiele, S. Kerzenmacher, Activation of electrospun carbon fibers: the effect of fiber diameter on CO2 and steam reaction kinetics, *Journal of Polymer Research,* 28 (2021) 108.

[76] C.M. Liu, Complete solutions to extended Stokes' problems, *Mathematical Problems in Engineering*, Hindawi Publishing Corporation, Volume 2008, Article ID 754262, 18 pages.

[77] K.J. Laidler, The development of the Arrhenius equation, *J. Chem. Educ*., 61(6) (1984) 494.

[78] X. Sun, H. Lu, T.E. Rufford, R.R. Gaddam, T.T. Duignan, X. Fan, and X.S. Zhao, A flexible graphene–carbon fiber composite electrode with high surface area-normalized capacitance, *Sustainable Energy Fuels*, 3 (2019) 1827.

Appendix A: Brooks-Corey Correlation

In the Richards equation, the diffusion coefficient is defined as:

$$D(S) = \left(\frac{k(S)}{\mu\varepsilon} \right) \left(\frac{\partial p_c(S)}{\partial S} \right). \tag{A1}$$

Based on the experimental data obtained by Brooks and Corey [44] for different granular materials, the capillary pressure, $p_c(S)$ in this equation can be related to S as shown below:

$$p_c(S) = p_{c,min}\, S^{-1/\lambda}, \tag{A2}$$

In this equation λ is a fitting parameter which depends on the microstructure of the material. Also, $p_{c,min}$ is a representative (constant) pressure used for normalizing the $p_c(S)$. Although in some papers atmospheric pressure has been used for this purpose, usually the minimum capillary pressure (i.e., capillary pressure corresponding to the maximum pore size (called the *retention size* in filter paper terminology) is used for this purpose. Assuming that the pores are spherical in shape, $p_{c,min}$ can be written as:

$$p_{c,min} = \frac{4\Gamma \cos\theta}{d_{max}}, \tag{A3}$$

where Γ is the surface tension, and θ is the contact angle, and d_{max} is the maximum pore size [44]. In addition to the capillary pressure being a function of S, Brooks and Corey showed that permeability too is related to the saturation field through the following power-law equation [44]:

$$k(S) = k_{max}\left(S^{3+2/\lambda} \right), \tag{A4}$$

where k_{max} is the maximum permeability. For fibrous materials it can be obtained using Huinink's equation [45]:

$$k_{max} = \frac{\varepsilon d_f^{\,2}}{8} \tag{A5}$$

By inserting $p_c(S)$ and $k(S)$ in Eq. A1, we obtain the following equation for the saturation-dependent diffusion coefficient D(S):

$$D(S) = D_0 S^n \tag{A6}$$

where n = 2 + 1/λ and D_0 is the maximum diffusivity corresponding to S = 1 (i.e., the fully-saturated case). Thus, we obtain:

$$D_0 = \frac{\varepsilon^2}{180(1-\varepsilon)^2}\left(\frac{4 d_{max}\sigma\cos\theta}{\mu\lambda}\right). \tag{A7}$$

Clearly, D_0 plays a key role in paper-based systems. As can be seen in Eq. A7, it involves parameters related to the fluid, to the solid, and to the fluid/solid interaction. A larger D_0 makes it easier for the fluid to spread through the pores of the material. Based on Eq. A7, it is evident that for a given fluid, liquid imbibition is facilitated by increasing porosity and maximum or average pore size. The role played by λ is seen to be qualitatively the same as the viscosity, and this suggests that it must be made as small as possible. This is not surprising realizing the fact that λ is a measure of porous material's tortuosity. It can also be interpreted as a measure of the pore-size and its random distribution; see, Fig. A1.

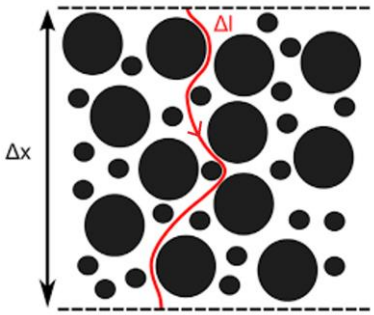

Figure A1: Schematic showing tortuous path which fluid should take in a poly-dispersed granular material.

Based on Eq. A2, a higher capillary pressure and therefore a stronger imbibition can be obtained at any given S using materials having a smaller λ. A smaller λ also gives rise to a sharper interface between wetting and non-wetting fluids making interface tracking/resolving easier. When translated in terms of n, a smaller λ means a larger n. For most filter papers, the power-law index (n) lies between 2 to 6. Materials having large "n" are more suitable for use in paper-based systems.

Appendix B: Derivation of Cathode Boundary Condition

As mentioned in Chapter 3, our numerical scheme requires that the potential of cathode is given as a boundary condition. While in steady mode it is as simple of assigning a certain real number to the cathode voltage, in unsteady mode, we have to derive the boundary condition. As the starting point, let's assume that $i(x,z)$ is the local current density [A/m^2] which can be obtained from Butler-Volmer equation. Let's also assume that $\vec{i}_s(x,z)$ is the current density vector in the electrode. Conservation of charge requires that for the cathode we should have:

$$\nabla.\ \vec{i}_s = \nabla.\ \left(-\sigma_s^{eff}\vec{\nabla}\varphi_s\right) = -\sigma_s^{eff}\vec{\nabla}\varphi_s = -aj_l \ \Rightarrow\ -\sigma_s^{eff}\nabla^2\varphi_s = -aj_l \tag{B.1}$$

where "a" [m^{-1}] is the specific active surface area [m^2] per unit volume [m^3]. To find the total current, we have to integrate this equation over the whole volume of the cathode:

$$\iiint_{\forall} -\sigma_s^{eff}\vec{\nabla}\varphi_s d\forall = \iiint_{\forall} -aj_l d\forall = I \tag{B.2}$$

Since y-direction is the neutral direction, this integral can be written as:

$$-\sigma_s^{eff} w \iint_A \nabla^2\varphi_s\ dA = -\sigma_s^{eff} w \iint_A \left(\frac{\partial^2\varphi_s}{\partial x^2} + \frac{\partial^2\varphi_s}{\partial z^2}\right) dxdz = I \tag{B.3}$$

Thus we have:

$$-\sigma_s^{eff} w\left[\iint_A\left(\frac{\partial^2\varphi_s}{\partial x^2}dx\right)dz+\iint_A\left(\frac{\partial^2\varphi_s}{\partial z^2}dz\right)dx\right]=I \tag{B.4}$$

After integrating this equation once we obtain:

$$W\int_0^{H_e}\sigma_s^{eff}\left(\left.\frac{\partial\varphi_s}{\partial x}\right|_{x=L_e}-\left.\frac{\partial\varphi_s}{\partial x}\right|_{x=0}\right)dz+W\int_0^{L_e}\sigma_s^{eff}\left(\left.\frac{\partial\varphi_s}{\partial z}\right|_{z=H_e}-\left.\frac{\partial\varphi_s}{\partial z}\right|_{z=0}\right)dx=I \tag{B.5}$$

At this stage, we should decide on the plane through which we can collect the current during the unsteady mode of operation, and we have two options for this: 1) we can orient the collectors so that current is collected in the x-direction, and 2) we can orient them such that it is collected in the z-direction. In the PowerPAD, the first option has been used. In Fig. B.1, the plane through which current is collected has been shown by a green line on the left-hand-side of the cathode. We apply the potential boundary condition on this plane.

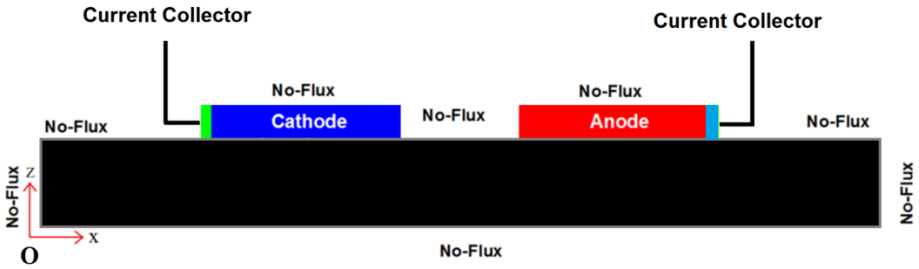

Figure B.1. Position of the current collectors in the PowerPAD.

With the other boundaries being of no-flux type, we have:

$$W\int_0^{H_e}\sigma_s^{eff}\left(\left.\frac{\partial\varphi_s}{\partial x}\right|_{x=16}-\left.\frac{\partial\varphi_s}{\partial x}\right|_{x=4}\right)dz+W\int_0^{L_e}\sigma_s^{eff}\left(\left.\frac{\partial\varphi_s}{\partial z}\right|_{z=H_e}-\left.\frac{\partial\varphi_s}{\partial z}\right|_{z=0}\right)dx=I \tag{B.6}$$

For this type of current collector, the potential of the cathode should, at all times, satisfy the following equation:

$$I = -\sigma_s^{eff} W \int_0^{H_e} \left.\frac{\partial \varphi_s}{\partial x}\right|_{x=4mm} dz \tag{B.7}$$

And this is the Eq. (3.15) in the main text.

Appendix C: Importance of Migration Flux for the PowerPAD

In Chapter 2, the migration term was included in the Nernst-Planck equation because, in true sense, it is never equal to zero. But, there are situations in which this term can be ignored when compared with other terms in this equation. For example, in [46] this term was ignored for an all-vanadium cell on the basis that the concentration of its acidic electrolyte was so high (say, 8M) that the energy of the electrostatic force (i.e., the force generated by ionic-potential gradient) was absorbed while mobilizing the small-sized protons. For the PowerPAD the concentration of the electrolytes is just 0.2M, and dropping this term may not be so justifiable. But, in the PowerPAD the migration term competes with diffusion term only. Thus, if we can show that it is much smaller than the diffusion term, we are still entitled to ignore the migration term in our unsteady analysis. With no convective flux involved, the Nernst-Planck equation becomes:

$$\varepsilon\left(\frac{\partial c_i}{\partial t}\right) - \underbrace{D_i \nabla^2 c_i}_{\text{diffusion}} - \underbrace{z_i \frac{F}{RT} D_i \left(c_i \nabla^2 \varphi_f + \vec{\nabla} c_i \cdot \vec{\nabla} \varphi_f\right)}_{\text{migration}} = -\mathbf{R}_i \tag{C.1}$$

The migration term is seen to make the Nernst-Planck equation highly nonlinear. In fact, the nonlinear term $\left(\vec{\nabla} c_i \cdot \vec{\nabla} \varphi_f\right)$ is also responsible for strong coupling between the concentration field and the ionic potential field. Evidently, the migration term dramatically increases the difficulty level of solving this equation. Figure C.1 shows typical results obtained using COMSOL. From this figure, it can be concluded that migration of species across the interface slightly lowers the critical time. The prediction that migration term does not play a key role on the performance of the PowerPAD is not surprising when it is noted that the operating point of this flow cell is quite close to its OCV. As a result, the cell always operates at a small current density that becomes smaller and smaller as time progresses, until it becomes virtually equal to zero.

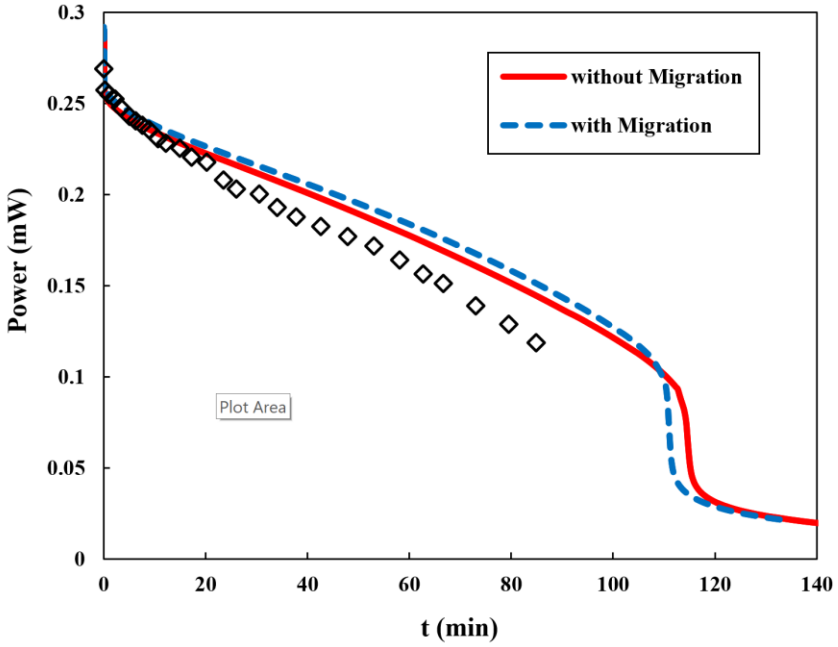

Figure C.1: Effect of migration on the 4h-2000 system in PowerPAD. Symbols are the experimental data [17].

We can also resort to a simple dimensional analysis proposed by Ibanez et al. [62] to show that migration term is indeed much smaller than the diffusion term in the PowerPAD. For an all-vanadium, Y-shaped microfluidic flow-cell equipped with flow-by electrodes they argue that a good measure for deciding whether migration term can be ignored or not is the following dimensionless number called “Electric-Potential Number”, Ψ:

$$\Psi = \frac{\Delta\phi}{RT/F} \tag{C.2}$$

where $\Delta\phi$ is the potential difference across the gap between the electrodes as a result of electrostatic (migration) force. They argued that if this dimensionless number is sufficiently small then migration effects can be ignored. To estimate $\Delta\phi$ for the PowerPAD, we need the ionic potential gradient $\nabla\phi_f$. This gradient is related to the concentration gradient, as shown below:

$$\nabla\phi_f \approx -\frac{F\sum_i z_i D_i \left(\nabla c_i\right)}{\sigma} \tag{C.3}$$

where σ_f is the ionic conductivity of the electrolyte. Note that only H2BQS and BQS contribute to this equation because the other two quinone species are not charged. The concentration gradient across the electrodes is then estimated as $\nabla c \approx c/\delta$ where it is assumed that the diffusion thickness $(\delta = \sqrt{Dt})$ has become equal to the gap distance between the two electrodes, which is 2 mm. Since the electrical conductivity of 0.2M sulfuric acid at room temperature is roughly equal to $0.73\ (S/cm)$, based on the above equations we estimate the gradient in ionic potential as: $\nabla\phi_f \approx 0.1\ (V/m)$. With this estimated value for the ionic-potential gradient, the electric potential difference across the electrodes due to migration effect is estimated as: $\Delta\phi \approx \delta\nabla\phi = 2\times10^{-4}\ (V)$. And this leads to $\Psi \approx 0.008$ which is much smaller than unity. This small value for the electric-potential number (better say "migration number") justifies ignoring the migration term for the PowerPAD.

Appendix D: The Concept of Back-Diffusion Time

As discussed in the main body of text, PowerPAD is a cell which works based on back diffusion. That is to say that, the cell is initially filled with the active species so that it becomes fully-saturated cell. It is then connected to an external load in the same way that an ordinary dry cell is used to power, say, a light bulb. And, as soon as the cell is connected to an external load, active species in the electrodes start being consumed. Obviously, this process lowers species concentration inside the electrodes. With their concentration being high inside the absorbent pad, a concentration gradient is established in the cell that causes species to diffuse from the pad back to the electrode — the so-called *back-diffusion*. Theoretically, this back-diffusion process should last as long as we have unused species left in the pad. The question is: How long does it take for the fuel residing in the pad to completely diffuse back to the complete? To answer this question, we can resort to a simple one-dimensional analysis even though our simulation for PowerPAD was based on a two-dimensional analysis. One thing good

about one-dimensional analysis is that it renders itself to a well-known analytical solution. The analytical solution can easily provide us with an upper bound for the runtime of the cell. Moreover, unlike the 2D analysis, which requires numerical methods, the 1D analysis can provide us with a better insight as to the parameters affecting the cell's runtime. In our 1D analysis, we ignore variation in the x-direction so that we have c(z,t). Assuming that the diffusivity (D) is constant, Fick's second law of diffusion can then be written as:

$$\frac{\partial c}{\partial t} = D\left(\frac{\partial^2 c}{\partial z^2}\right). \tag{D.1}$$

This linear partial-differential equation is first-order in time, and so it needs an initial condition. It is assumed that initially the concentration field is uniform at c_i; that is:

$$c(z > 0, t = 0) = c_i \tag{D.2}$$

Equation D.1 is second-order in z thus we need two boundary conditions. At the bottom plate (z = 0) we impose the no-flux condition. At z = H (i.e., at the inlet plane of the electrodes) we assume that suddenly the concentration is dropped from c_i to c = 0 (which this tacitly means that electrochemical reaction occurs spontaneously). Thus, we have:

$$\begin{aligned} &c(z = H, t > 0) = 0 \\ &\partial c / \partial z \;\; (z = 0, t > 0) = 0 \end{aligned} \tag{D.3}$$

Fortunately, Eq. (D.1) subject to these initial/boundary conditions renders itself to an analytical equation. In dimensionless form, the analytical solution reads as [76]:

$$C(Z, T) = \sum_{n=0}^{\infty} \frac{2}{K} \sin(K)\, e^{-(K^2 T)} \cos(KZ), \tag{D.4}$$

where,

$$C = \frac{c}{c_i},\; Z = \frac{z}{H},\; T = \frac{Dt}{H^2},\; K = \frac{(1+2n)\pi}{2}. \tag{D.5}$$

Figure D.1 shows a plot of Eq. (D.4) as a function of the dimensionless time, T. This figure shows that, as time progresses, the pad is progressively depleted from the fuel.

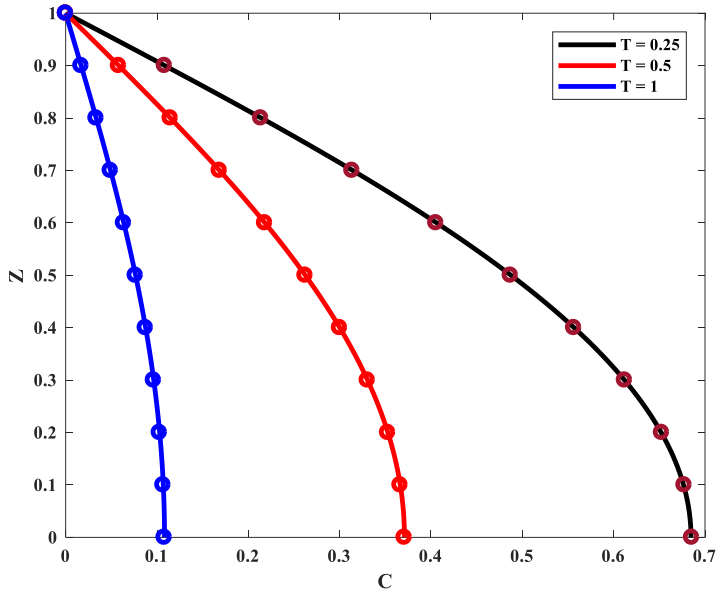

Figure D.1. Variation of fuel concentration as a function of time based on one-dimensional analysis.

This simple analysis outlined above can give us an estimation of the time needed for the pad to become completely depleted from the fuel. To estimate the "depletion time", we need H and D. For the 4h-pad system, we have H = 3.32 mm. On the other hand, diffusivity of the fuel is known to be around 4×10^{-6} $(\mathrm{cm}^2/\mathrm{s})$. Using the above analytical solution, we can calculate the dimensionless concentration (c/c_i) as a function of time at any given height, z. Figure D.2 shows its variation near the bottom plate (z = 0). This figure shows that after roughly T = 4 no fuel is virtually left at the bottom plate inferring that the pad is completely depleted of the fuel. This dimensionless time corresponds to roughly 30 hours suggesting that, in theory, the cell can continue producing power for roughly a day. And, this is the upper bound for the runtime of the PowerPAD.

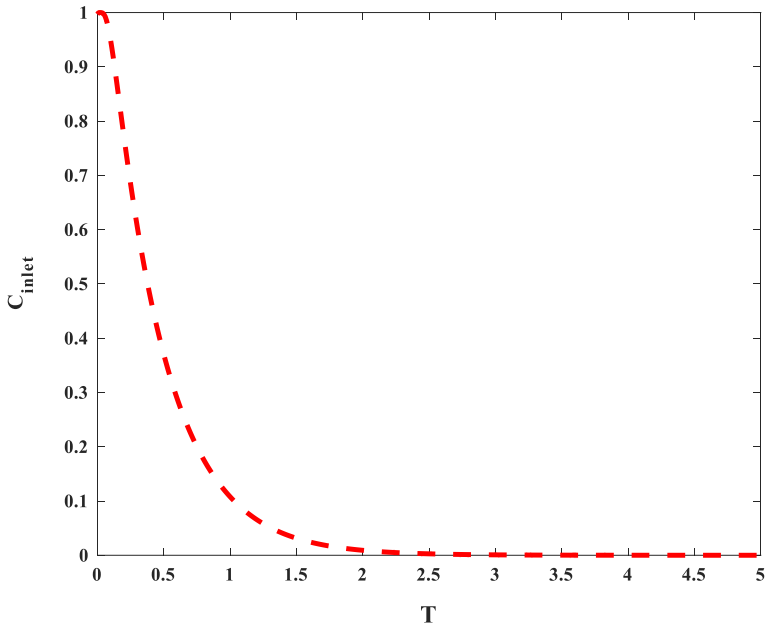

Figure D.2. Variation of dimensionless fuel concentration at the bottom plate as a function of dimensionless time based on one-dimensional analysis.

It is interesting to note that although one-dimensional analysis is a rough representation of the PowerPAD (which is a 3D cell, in true sense) it can give us an upper bound for its runtime. In practice, however, due to crossover less fuel can diffuse back to the anode and this makes its runtime shorter. It should also be noted that, unlike chemical reactions, electrochemical reactions are not spontaneous and this also lowers the runtime. Still, the 1D solution is worthwhile as it clearly shows the importance of the diffusion thickness, $\delta = \sqrt{Dt}$ on the runtime. That is to say that, as soon as it becomes of the same order as the height of the cell, H, the degree of species diffusion is evidently weakened. Based on Fig. D.2, this situation is reached around T = 1 (which is roughly equivalent to 4 hours). This finding suggests that flow cells such as PowerPAD should preferably be used for T<1 while back-diffusion is strong. Fortunately, diagnostic kits usually meet this criterion suggesting that flow cells such as PowerPAD are best suited for such applications.